

DEEP WATER DISPERSION EXPERIMENT
RAFOS COMPONENT
FINAL REPORT

*BY H. FUREY, A. RAMSEY, T. MEUNIER,
P PÉREZ-BRUNIUS, P GARCIA CARILLO, J. RODRÍGUEZ OUTERELO,
AND A. BOWER*

July 2020



TABLE OF CONTENTS

CHAPTER 1. INTRODUCTION	1
1.1 Background	1
1.2 Objectives	1
1.3 Field Program Description	2
1.4 Major Events	6
1.5 Analysis Focus	9
1.6 Report Organization	9
CHAPTER 2. METHODOLOGY	10
2.1 RAFOS Float Dataset	10
2.2 Ancillary Satellite Altimeter Dataset	14
CHAPTER 3. BASIC STATISTICS	17
3.1 Float Mission Lengths	17
3.2 Number of Floats Per Month	19
3.3 Float Speed	21
3.4 Float Displacement	24
3.5 “Loopiness” Ratio	24
3.6 Interesting Examples	26
3.7 Eddy Census	34
3.8 Lagrangian Integral Time Scales	41
3.9 Loop Current Rings	44
3.10 Pseudo Eulerian Statistics and Dominant Circulation Patterns	54
CHAPTER 4. FLOAT ANALYSIS	66
4.1 ABSOLUTE DYNAMIC TOPOGRAPHY AND TRAJECTORY DATA	66
4.2 DISPERSION STATISTICS	82
CHAPTER 5. Discussion and Recommendations for Future Studies	89
5.1 RECOMMENDATIONS	91
CHAPTER 6. Acknowledgements	93
CHAPTER 7. References	94

LIST OF FIGURES

CHAPTER 1. INTRODUCTION

Figure 1-1 Experiment Timeline.....	3
Figure 1-2 Surface drifter and RAFOS float nominal deployment locations.....	4
Figure 1-3 Proposed experiment design for deployment locations	5
Figure 1-4 Loop Current Eddies (LCRs).....	6
Figure 1-5 Storm tracks of major hurricanes, hurricanes, and tropical storms.....	8

CHAPTER 2. METHODOLOGY

FIGURE 2-1 DEPLOYMENT LOCATIONS FOR SOUND SOURCES AND RAFOS FLOATS.....	11
Figure 2-2 Float performance chart.....	12
Figure 2-3 Displacement vectors for RAFOS floats	13
Figure 2-4 Trajectories for RAFOS floats	14
Figure 2-5 Time series for SSH steric signal	15
Figure 2-6 Gulf of Mexico region where the SSH spatial average was performed	16

CHAPTER 3. BASIC STATISTICS

Figure 3-1 Number of floats per trajectory length	18
Figure 3-2 Number of floats in water per month	20
Figure 3-3 Spaghetti diagram for 300-dbar floats	22
Figure 3-4 Spaghetti diagram for 1500-dbar floats	23
Figure 3-5 Float displacements.....	24
Figure 3-6 Float Loopiness Ratio.....	25
Figure 3-7 Trajectory for float 1509.....	27
Figure 3-8 Trajectory for float 1513.....	28
Figure 3-9 Trajectory for float 1504.....	29
Figure 3-10 Trajectory for float 1481.....	30
Figure 3-11 Trajectory for float 1516.....	31
Figure 3-12 Trajectory for float 1526.....	32
Figure 3-13 Trajectory for float 1533.....	33
Figure 3-14 Trajectory for floats 1456 & 1472.....	34
Figure 3-15 Trajectory eddy segments plotted by pressure level	37
Figure 3-16 Example of an eddy	38
Figure 3-17 Deep anticyclonic formation off the Campeche Escarpment.....	40
Figure 3-18 Autocorrelation of velocity for 300-dbar Floats	42
Figure 3-19 Autocorrelation of velocity for 1500-dbar Floats	42
Figure 3-20 Lagrangian integral time scale for 300-dbar Floats	43
Figure 3-21 Lagrangian integral time scale for 1500-dbar Floats	43

Figure 3-22 Taylor diffusivity for 300- and 1500-dbar Floats	44
Figure 3-23 Life cycles and interactions of six LCRs	45
Figure 3-24 Time evolution of LCR A and its 'children' eddies.....	47
Figure 3-25 Time evolution of LCR A's properties	48
Figure 3-26 Time evolution of LCR B and its 'children' eddies.....	49
Figure 3-27 Time evolution of LCR B's properties.....	49
Figure 3-28 Time evolution of LCR C and its 'children' eddies.....	50
Figure 3-29 Time evolution of LCR C's properties.....	50
Figure 3-30 Time evolution of LCR D and its 'children' eddies	51
Figure 3-31 Time evolution of LCR D's properties	51
Figure 3-32 Time evolution of LCR E and its 'children' eddies	52
Figure 3-33 Time evolution of LCR E's properties.....	52
Figure 3-34 Time evolution of LCR F and its 'children' eddies	53
Figure 3-35 Time evolution of LCR F's properties	53
Figure 3-36 Data grid for study area.....	55
Figure 3-37 Number of observations.....	56
Figure 3-38 Degrees of freedom.....	57
Figure 3-39 Mean velocity vectors.....	58
Figure 3-40 Variance ellipses	59
Figure 3-41 Polar distributions of θ and distribution of velocity ratio	61
Figure 3-42 Mean kinetic energy	63
Figure 3-43 Eddy kinetic energy.....	64
Figure 3-44 Percent mean to total kinetic energy	65

CHAPTER 4. FLOAT ANALYSIS

Figure 4-1 Absolute dynamic topography and trajectory data: Jul to Aug 2016.....	67
Figure 4-2 Absolute dynamic topography and trajectory data: Sep to Oct 2016.....	68
Figure 4-3 Absolute dynamic topography and trajectory data: Nov to Dec 2016.....	69
Figure 4-4 Absolute dynamic topography and trajectory data: Jan to Feb 2017	70
Figure 4-5 Absolute dynamic topography and trajectory data: Mar to Apr 2017	71
Figure 4-6 Absolute dynamic topography and trajectory data: May to Jun 2017	72
Figure 4-7 Absolute dynamic topography and trajectory data: Jul to Aug 2017	73
Figure 4-8 Absolute dynamic topography and trajectory data: Sep to Oct 2017	74
Figure 4-9 Absolute dynamic topography and trajectory data: Nov to Dec 2017.....	75
Figure 4-10 Absolute dynamic topography and trajectory data: Jan to Feb 2018	76
Figure 4-11 Absolute dynamic topography and trajectory data: Mar to Apr 2018.....	77
Figure 4-12 Absolute dynamic topography and trajectory data: May to Jun 2018.....	78
Figure 4-13 Absolute dynamic topography and trajectory data: Jul to Aug 2018.....	79
Figure 4-14 Absolute dynamic topography and trajectory data: Sep to Oct 2018.....	80

Figure 4-15 Absolute dynamic topography and trajectory data: Nov to Dec2018.....	81
Figure 4-16 Absolute dynamic topography and trajectory data: Jan to Feb 2019	82
Figure 4-17 Launch locations for RAFOS and APEX floats from previous GoM program	84
Figure 4-18 Relative dispersion against time and relative diffusivity against pair separation	85
Figure 4-19 Dispersion and diffusivity model results for surface	86
Figure 4-20 Dispersion and diffusivity model results for 300 m.....	87
Figure 4-21 Dispersion and diffusivity model results for 1500 m.....	88

LIST OF TABLES

CHAPTER 1. INTRODUCTION

Table 1-1 Loop Current Eddy detachment and death dates.....	7
Table 1-2 Atmospheric storm events.....	8

CHAPTER 3. BASIC STATISTICS

Table 3-1 Percent of float missions lengths.....	17
Table 3-2 Number of floats in water per month.....	19
Table 3-3 Speed ranges for 300-dbar floats.....	21
Table 3-4 Speed ranges for 1500-dbar floats.....	21
Table 3-5 Loopiness ratios and percent Loopiness.....	26
Table 3-6 Total number of eddies by depth	36
Table 3-7 Eddy mean statistics	39
Table 3-8 List of variable definitions and abbreviations used in section 3.4.....	54
Table 3-9 Basic statistics for MKE and EKE	62

CHAPTER 1. INTRODUCTION

1.1 BACKGROUND

The Deep Water Dispersion Experiment (DWDE) is the observational component of the “Deep and shallow particle dispersion and biological connectivity over the continental slope in the western Gulf of Mexico” project, which is Subproject 1 of the megaproject “Ocean observation platforms, base line, numerical modeling and scenarios of natural response of the Gulf of Mexico, under potential large scale oil spills”, directed by the Consorcio de Investigación del Golfo de México (CIGoM) and funded by the Fondo Sectorial SENER-CONACYT-Hidrocarburos. The overarching goal of the megaproject is to better understand the consequences of a large scale oil spill in the Gulf of Mexico, with a significant part aimed at developing high-resolution ocean circulation models to reproduce the spread of a contaminated patch of water. These models must include, either explicitly or with accurate parameterization, the most important transport mechanisms in the Gulf of Mexico.

The main purpose of the physical oceanography component of Subproject 1 was to characterize deep-ocean particle dispersion in the Perdido region of the western Gulf of Mexico, both at the surface and at depth. This study was designed with the overarching intention of understanding the processes involved in the spreading of a passive tracer, and assessing the accuracy of the numerical models in reproducing the observed dispersion and movement of particles. To this end, we proposed a study to deploy and analyze a large number of surface drifters, subsurface acoustically-tracked floats (RAFOS), and an autonomous vehicle (ocean glider) equipped with novel technological enhancements in both the instrumentation and data processing stages. The use of both subsurface floats and surface drifters to collect Lagrangian data is critical to understanding the effects of small-scale oceanic features in the spread and dispersion of a tracer, since even state-of-the-art numerical models cannot resolve all scales of motion of real ocean flows. The result is a significant step forward in the understanding of particle dispersion in the Perdido region, with relevance to similar hydrodynamic systems around the world.

1.2 OBJECTIVES

The DWDE component, which is the subject of this report, specifically addressed the subsurface circulation and dispersion of the western Gulf of Mexico’s Perdido region. The Gulf of Mexico is characterized as a two-layer circulation system (e.g., Hamilton et al., 2019). The upper layer ranges from 0 to ~1000m and includes the Loop Current and Loop Current Rings (also referred to as Loop Current Eddies). The lower layer is found between ~1000m and the seafloor. The depth of the interface between the two layers is generally determined by the depth of the Loop Current, which is characterized by the 6°C isotherm (Hamilton et al., 2019). The Loop Current enters through the Yucatan Channel and extends into the Gulf to varying degrees. At its farthest extent into the Gulf, the Loop Current pinches off a large eddy with a diameter of several hundred kilometers, forming a Loop Current Ring (LCR). Once the LCR is pinched

off the Loop Current, the Loop Current retracts towards the southeastern Gulf (Oey et al., 2005) and departs through the Florida Straits.

In order to capture synoptic circulation and dispersion characteristics of the full water column, deployments of subsurface RAFOS floats were coordinated with surface drifter deployments (part of another project under Subproject 1), simultaneously sampling the surface, upper layer and lower layer. The DWDE subsurface Lagrangian drifters (RAFOS floats) were deployed at 300 and 1500 dbar, recording temperature, pressure, and position three times per day, to resolve mesoscale motions. The drifters and floats were deployed in groups of 2-4 instruments in order to characterize dispersion at the surface, in the upper layer, and in the lower layer.

Specific Objectives:

1. Characterize the basic properties of particle dispersion in the Perdido region both at the surface and at depth, including the magnitude and orientation of the dispersion as a function of cross-slope location. This will test our initial hypothesis that the degree of anisotropy will be enhanced in the vicinity of the continental shelf break.
2. Understand the role of various environmental factors controlling particle dispersion, including (i) the effect of mesoscale eddies and fronts on cross-shelf and along-shore dispersion, (ii) the role of stratification, particularly with respect to the annual cycles in water column properties, and (iii) the impact of wind forcing modulating dispersion characteristics. We expect that the rate of dispersion will depend upon the relative position of the simulated patch and the location of the mesoscale eddies present, and that the rate of dispersion will decay with depth.
3. Provide a dataset to assess the accuracy of model predictions and improve the parameterizations of submesoscale features in ocean models for deep water regions of the Gulf of Mexico.

1.3 FIELD PROGRAM DESCRIPTION

The RAFOS float program planned to support “Subproject 1. Deep and shallow particle dispersion and biological connectivity over the continental slope in the western Gulf of Mexico,” consisted of deploying 84 RAFOS floats in the Perdido region of the Gulf of Mexico (Figure 1-1). The RAFOS floats were to be deployed in groups of 21 every spring and fall for two years, coinciding with surface drifter deployments belonging to a companion project conducted by CICESE and UABC (Centro de Investigación Científica y de Educación Superior de Ensenada and Universidad Autónoma de Baja California). Figure 1-2 shows the locations along the slope of these ‘stacked,’ nearly simultaneous (within an hour’s time) deployments. This allowed investigators to observe the influence of surface wind on the spreading of a tracer at the surface, as opposed to the dispersal of the tracer at depths below the Ekman layer, which are isolated from the direct influence of wind.

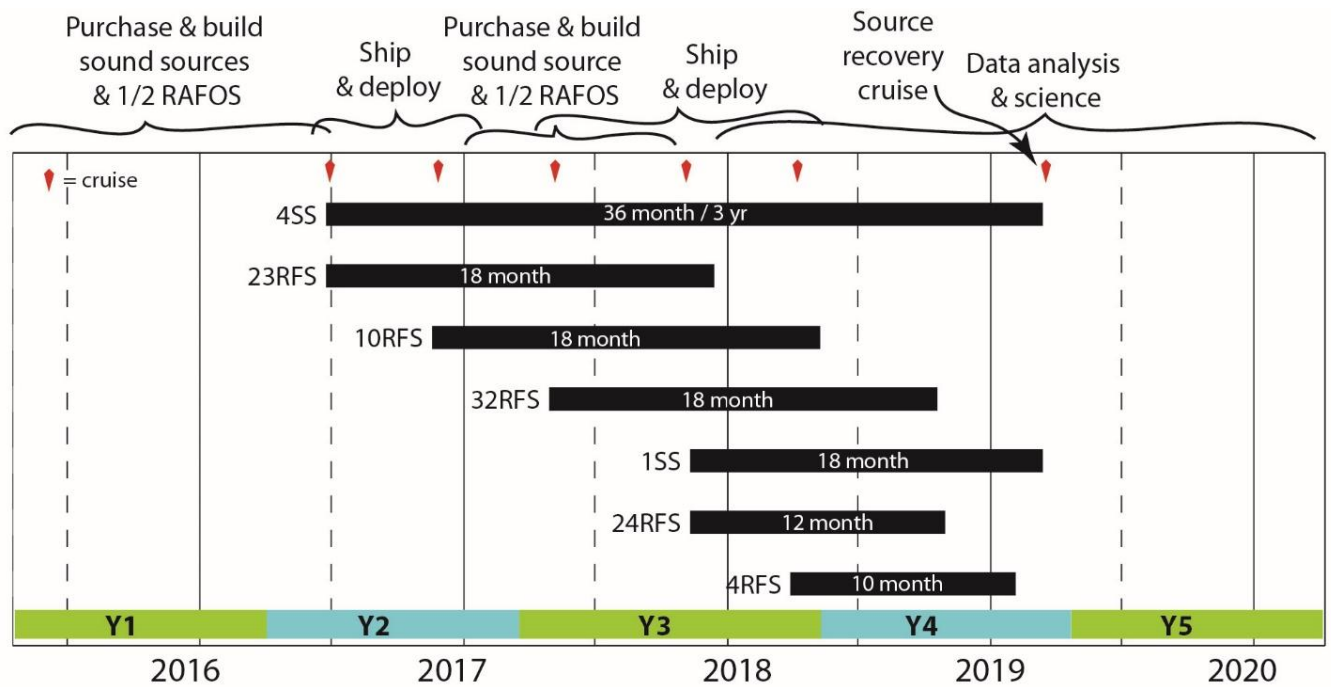


Figure 1-1. Experiment timeline, where 'SS' denotes sound source mooring deployment, 'RFS' denotes RAFOS float deployment. The original deployment schedule consisted of one sound source deployment cruise and four float deployment cruises. An additional sound source and float deployment cruise was added after the project began.

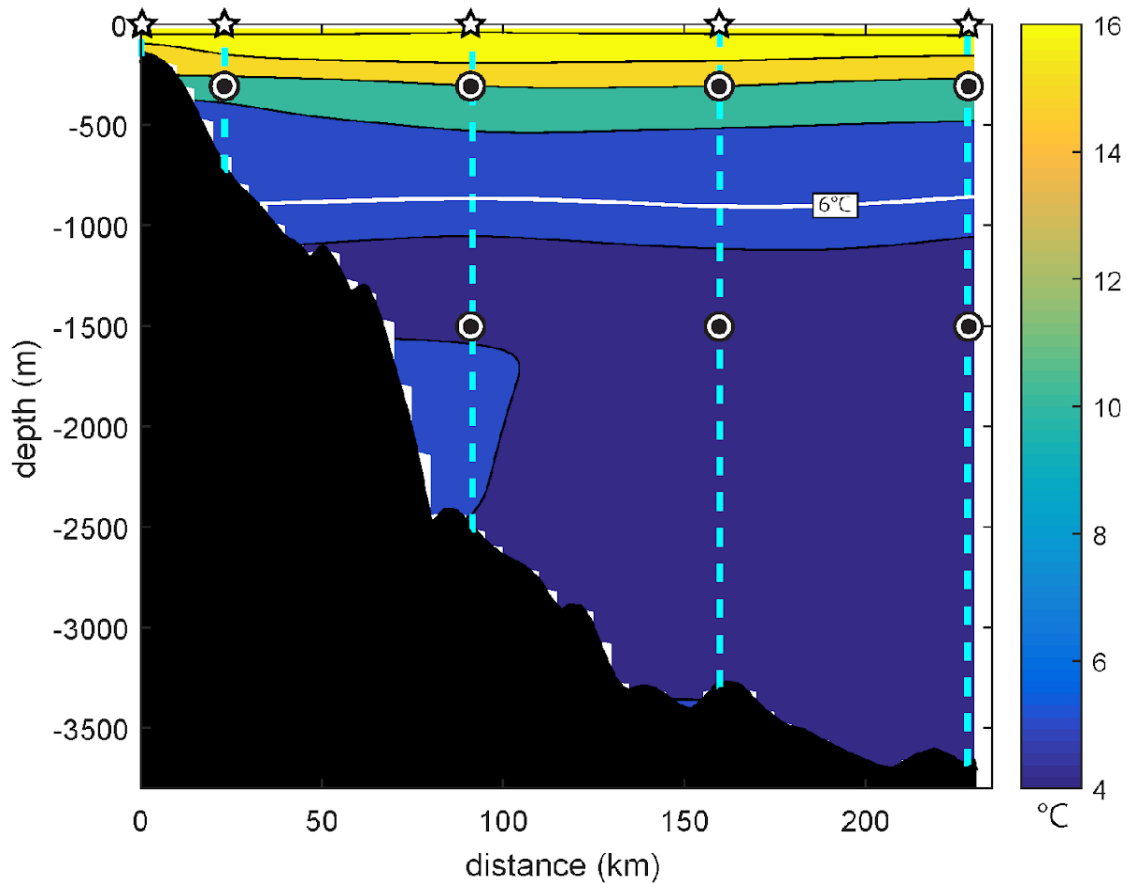


Figure 1-2. Surface drifter (star) and RAFOS float (double-circle) nominal deployment locations plotted over the cross-shelf section of DWDE-1 conservative temperature (TEOS-10). Both surface drifters, which were deployed as part of a companion project, and RAFOS floats were deployed in groups of 2-4 instruments and in vertical 'stacks' where two or three levels of the water column were seeded at the same position, depending on water depth. The 6°C isotherm is contoured in white, and represents the division between upper and lower layer flow fields in the Gulf of Mexico, as defined by Hamilton et al. (2018). Temperature is contoured every 2°C. Dashed vertical lines mark the CTD station locations. Bathymetry across the shelf has been interpolated from ETOPO2.

The RAFOS floats require a moored subsurface sound source array to track their movement. The trajectory of a float is obtained by triangulating its position based on the time of arrivals of acoustic signals emitted at fixed times by the sound sources. In order to get good tracking of the floats in the Perdido region, we deployed four sound source moorings to enslify the western Gulf of Mexico (Figure 1-3).

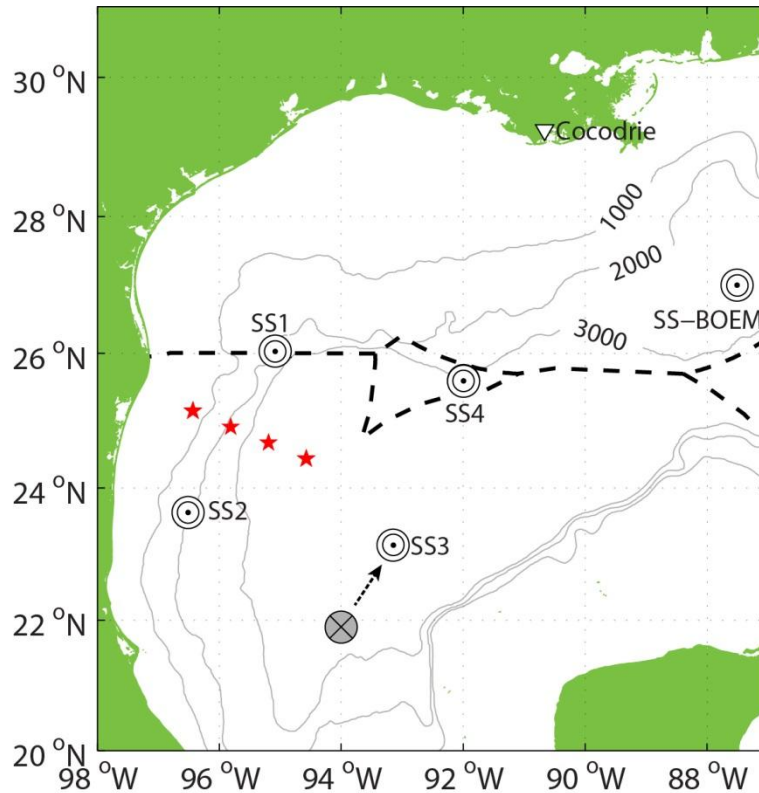


Figure 1-3. Proposed experiment design for the DWDE RAFOS and sound source mooring deployments. The red stars mark the surface drifter and RAFOS float nominal deployment locations. The triangle marker at Cocodrie, Louisiana, marks the homeport of the R/V Pelican, the ship used for the majority of the field program. Circle markers show sound source locations. The grayed marker shows the planned position of sound source 3, and the dashed arrow shows the actual position due to weather constraints during the deployment cruise. The position of a remnant sound source from a previous RAFOS float project, 'SS-BOEM,' is also marked. The thick dashed line marks the Exclusive Economic zone (EEZ) boundaries and red stars show the proposed deployment locations for the RAFOS floats.

1.4 MAJOR EVENTS

During the DWDE project, six LCRs were observed drifting through the Gulf of Mexico. The trajectories of their centers are shown in Figure 1-4; detachment dates and approximate death dates can be found in Table 1-1. All six LCRs were partially sampled by RAFOS floats at different times in their life cycles. Details of the LCRs' life cycle, mutual interactions, and RAFOS surveying periods are provided in Chapter 3.4.

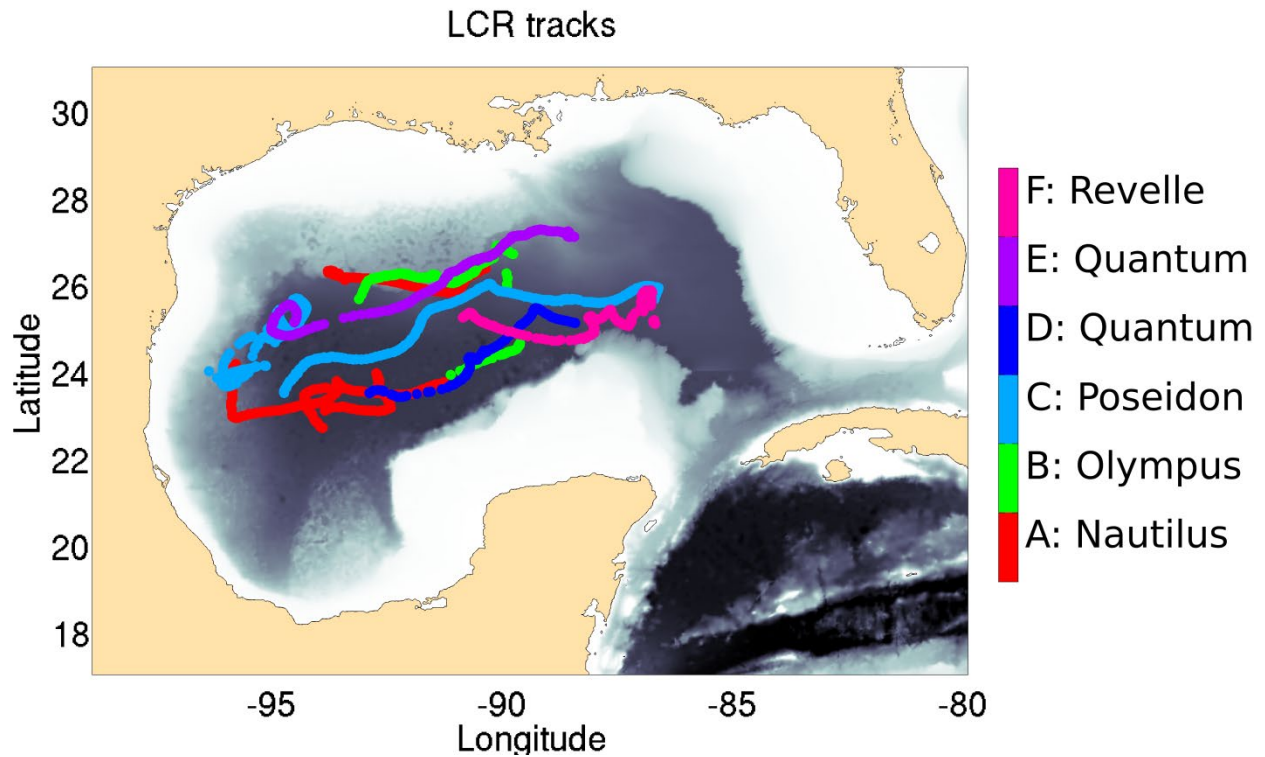


Figure 1-4. Tracks of Loop Current Eddies (LCRs) that were pinched off the Loop Current and drifted westward through the Gulf during the DWDE RAFOS observational period. LCR tracks are color coded and named.

Loop Current Ring	Detachment date	Death date
A: Nautilus	May 14 2015	October 31 2016
B: Olympus	October 15 2015	October 11 2016
C: Poseidon	April 15 2016	October 12 2017
D: Quantum II	November 04 2017	October 09 2018
E: Quantum I	February 08 2018	October 16 2018
F: Revelle	June 19 2018	December 31 2018

Table 1-1. *Table of Loop Current Eddy detachment and death dates of the LCRs that were pinched off the Loop Current and drifted westward through the Gulf during the DWDE RAFOS observational period.*

During the course of the DWDE experiment, 10 Tropical cyclones affected the Gulf of Mexico, including six tropical storms and four hurricanes. The trajectories of these storms are shown in Figure 1-5; storm formation and decay dates are provided in Table 1-2. Although the transfer of momentum between a hurricane and the ocean through surface stress does not reach the drift depth of the RAFOS floats, surface stresses can affect float trajectories through the downward propagation of inertial-gravity waves within anticyclonic structures such as LCRs (Pallas Sànz et al. 2016). Hurricane events are thus important for the understanding of near inertial kinetic energy in the float data.

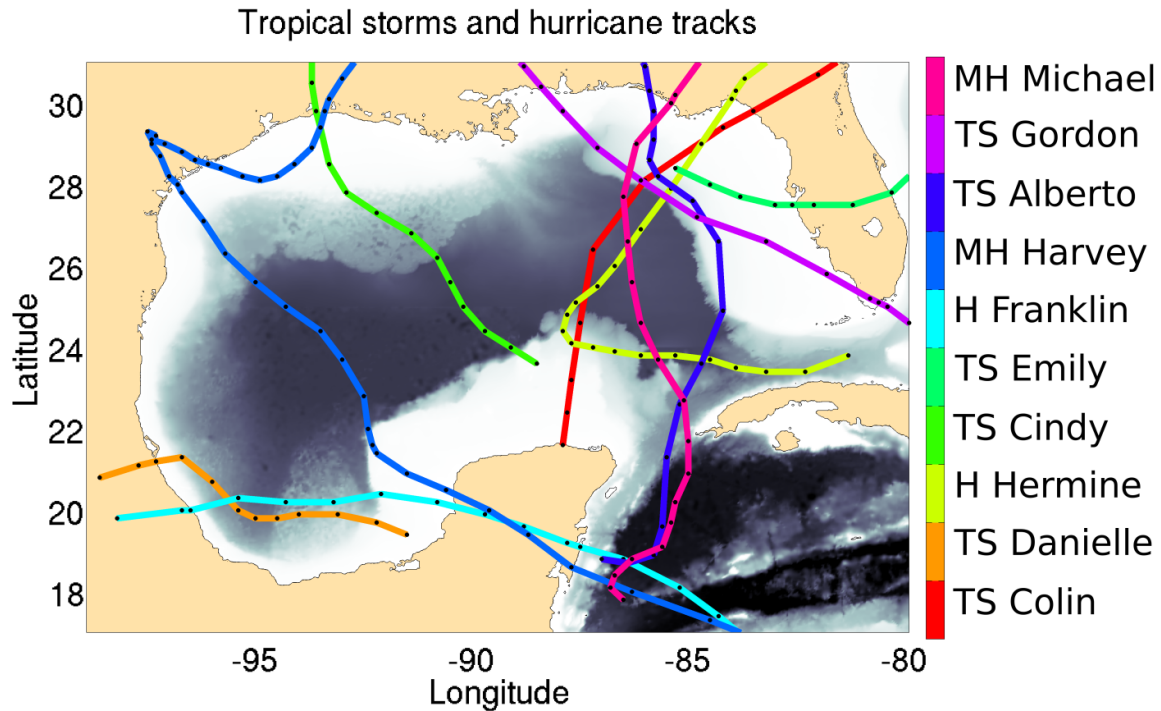


Figure 1-5. Storm tracks of major hurricanes (MH), hurricanes (H), and tropical storms (TS) that passed over the Gulf of Mexico during the DWDE RAFOS observational period. Storm tracks are color coded and naming convention indicates type of storm and storm name.

Tropical Cyclone	Intensity	Date range
Colin	Tropical Storm	June 5-7 2016
Danielle	Tropical Storm	June 19-21 2016
Hermine	Hurricane	August 28-September 03 2016
Cindy	Tropical Storm	June 20-23 2017
Emily	Tropical Storm	July 30-August 01 2017
Franklin	Hurricane	August 7-10 2017
Harvey	Major Huriicane	August 17-September 01 2017
Alberto	Tropical Storm	May 25-31 2018
Gordon	Tropical Storm	September 03-06 2018
Michael	Major Hurricane	October 07-11 2018

Table 1-2. Table of atmospheric storm event dates that were over the Gulf during the DWDE RAFOS observational period.

1.5 ANALYSIS FOCUS

The focus of analysis for this report was to: (1) assess the major Loop Current events that affected the western Gulf of Mexico during the time the RAFOS floats were tracked underwater; (2) calculate basic statistics for the RAFOS float dataset such as float duration, population over time, and mean speeds; (3) choose float examples from each pressure level that illustrate the different characteristics of circulation; (4) quantify the eddy field using statistical methods and provide kinematic statistics for the eddies; (5) determine the Lagrangian Integral Time Scale for both pressure levels; (6) provide a detailed description of each Loop Current eddy passing through the study region during the study period; (7) provide higher order float statistics such as gridded mean velocity, degrees of freedom, mean kinetic energy, and eddy kinetic energy in order to describe the basic circulation characteristics at both depths during the study period; (8) provide a description of the circulation of the entire system: the Loop Current and associated eddies, along with the upper and lower layer float trajectories over the time period covered by the field program; (9) provide an estimate of dispersion from the observational data and compare to model-derived estimates.

1.6 REPORT ORGANIZATION

This report is presented in the following order:

Chapter 2. A brief description of the experiment, field program design, instrumentation, and instrument data processing.

Chapter 3. A description of basic statistics for the RAFOS float dataset, a statistical analysis of the shallow and deep eddy field, determination of the Lagrangian Integral Time Scale for both pressure levels, a detailed description of each Loop Current eddy passing through the study region during the study period, and higher order float statistics used to describe the basic circulation characteristics at both depths during the study period.

Chapter 4. A description of the interaction of the major Loop Current events that affected the western Gulf of Mexico during the time the RAFOS floats were tracked underwater, June 2016 through December 2018, using the sea surface height combined with float-observed flows at 300 and 1500 dbar, and computation of the dispersion from surface drifter and float observations compared to modeled fluid particle dispersion.

Chapter 5. A summary of the major results found in this report and recommendations for further research using these data to fill knowledge gaps in the Gulf of Mexico.

CHAPTER 2. METHODOLOGY

2.1 RAFOS FLOAT DATASET

The primary goal of this subprogram was to study and quantify the subsurface dispersion of the Perdido region of the western Gulf of Mexico using subsurface Lagrangian drifters, specifically RAFOS floats. All details of experiment design, float ballasting, parameter setup, instrument drift characterization, instrument performance, and plots of collected and processed data are available in the WHOI Technical Report WHOI-2020-01, 'The Deep Water Dispersion Experiment: RAFOS Float Data Report, June 2016 - January 2019' by Ramsey et al. (2019).

The basic design of the project was to deploy sets of about 20 floats every few months from 2016-2018 (Figures 1-1). A single station transect was oriented perpendicular to the slope in the western Gulf's Perdido region (Figure 1-3), and multiple floats were launched at each station: two to four floats at 300 dbar and two to four floats at 1500 dbar, where bathymetry allowed (Figure 1-2). Figure 2-1 depicts the positions of the sound source moorings and float deployment locations for each of the five deployments. Discounting unexpected early termination of many of the 300-dbar float missions due to interaction with large marine animals (presumably sharks; Ramsey et al. 2019), the overall data return was excellent (> 95% data return of all floats not interrupted by shark attacks). Overall, 73 float-years' worth of data were collected. The bar diagram in Figure 2-2 shows the mission lengths of each float deployment over time.

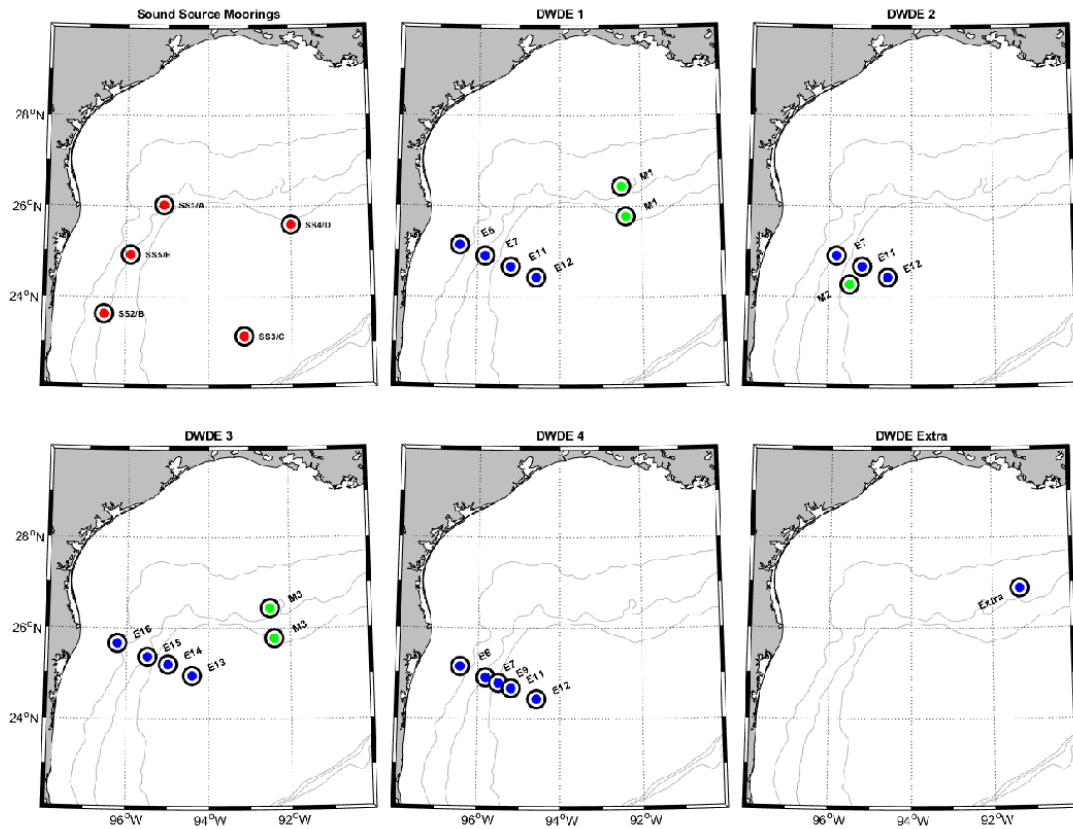


Figure 2-1. Deployment locations for sound sources (red dots), science floats (blue dots), and monitor floats (green dots). All sound source locations are shown in the first subplot. The following subplots each represent one of the five float deployment cruises. (From Ramsey et al. 2019)



Figure 2-2. Float performance chart. Each bar indicates the underwater mission length of the floats; serial numbers noted at left of each bar. The notation ‘DNS-’ indicates ‘Did Not Surface’ and ‘M-’ indicates ‘Monitor Float’, which is an intentionally short-missioned float used to report on signal strength of the sound sources. The histogram bars are color coded by float target pressure: Gray/Back indicates a 300/1500 dbar target pressure. (From Ramsey et al. 2019)

In general, floats at both seeding layers (300 and 1500 dbar) had the same displacement coverage (Figure 2-3), and both spread into the Bay of Campeche and eastward to about 89°W. Additionally, the floats at 300 dbar spread northward into the northwest Gulf as they were not bathymetrically constrained. The breakdown of displacement by cruise may be found in Ramsey et al. (2019) and in section 3.1.4 below, showing that the spread of the floats varied significantly depending on time of deployment, with floats reaching the Bay of Campeche or traveling eastward towards 89°W.

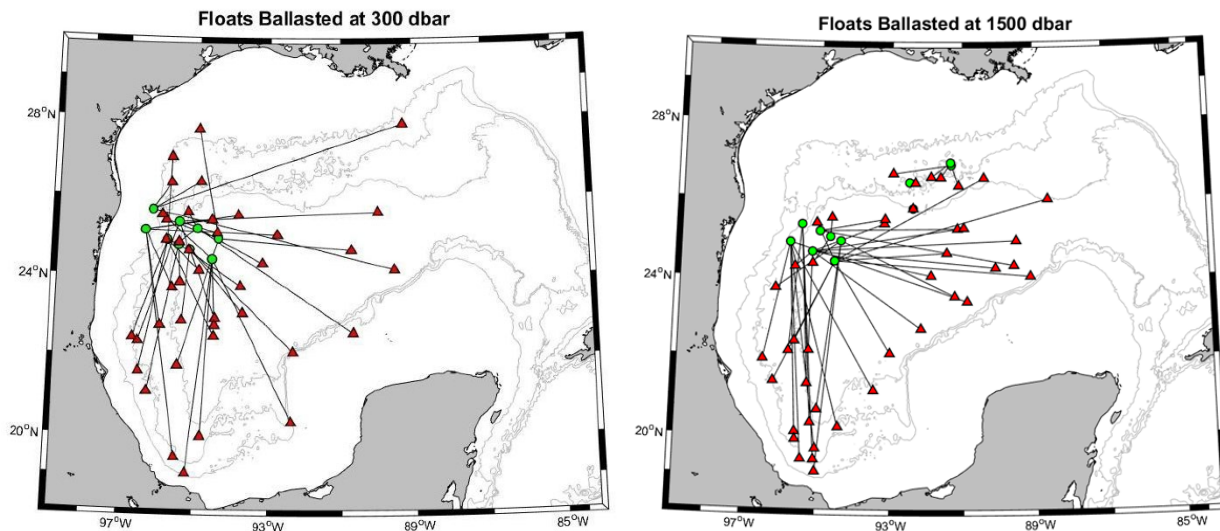


Figure 2-3. Displacements for all 300-dbar (left) and 1500-dbar (right) floats. Green circles indicate launch locations, red triangles indicate surface locations, and a black line connects the two. Note that not all mission lengths are the same. (From Ramsey et al. 2019)

An overview of all float trajectories for both depth layers (Figure 2-4) shows some differences in character between upper and lower layer float behavior. Qualitatively, upper-layer floats tend to trace out large loops during most of their lifetimes, presumably circulating in upper layer eddies shed or spun up by the Loop Current and/or LCR. Lower-layer floats appear to be more bathymetrically constrained along the western slope and around the perimeter of the Bay of Campeche, and exhibit looping motions when over the Sigsbee Abyssal Plain, in the flat-bottomed central Gulf.

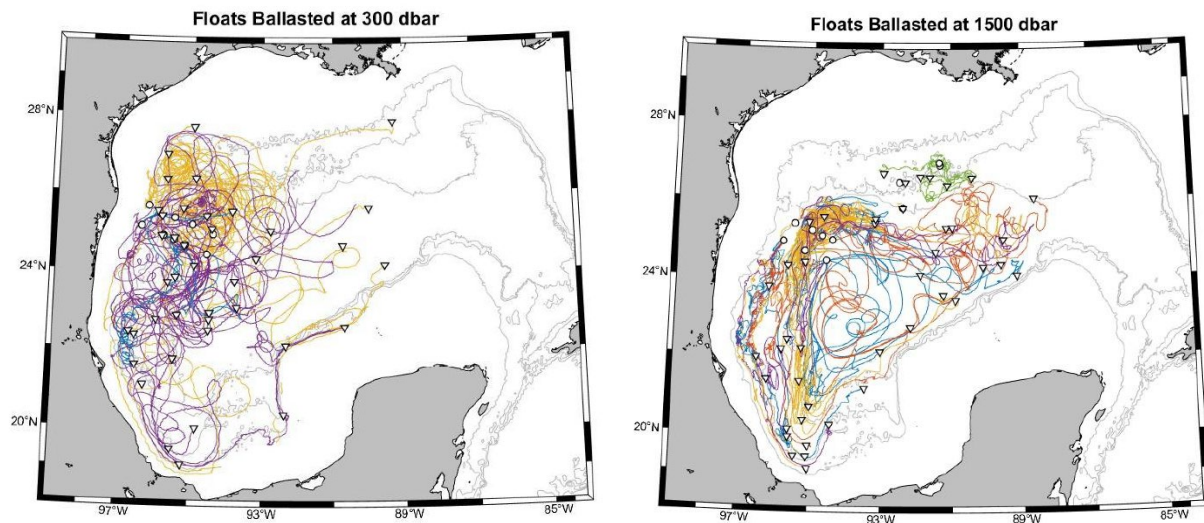


Figure 2-4. Trajectories for all 300-dbar (left) and 1500-dbar (right) floats. A circle indicates launch locations, triangle indicates surface location, and a line connects the two. Colors indicate deployment cruise: DWDE-1 (blue), DWDE-2 (orange), DWDE-3 (yellow), DWDE-4 (purple), and DWDE-Extra (green). Note that not all mission lengths are the same. (From Ramsey et al. 2019)

2.2 ANCILLARY SATELLITE ALTIMETRY DATASET

Satellite sea surface height data were used to investigate Loop Current and Loop Current Ring position and evolution over time during the float study period. The altimetry data used are absolute dynamic topography and geostrophic velocities from the AVISO Ssalto/DUACS product in its Delayed-Time (DT-MADT-H-UV) and Near-Real-Time (NRT-MADT-H-UV) versions. Spatial coverage includes the Gulf of Mexico and part of the Caribbean Sea, 97.875 W to 78.125 W and 16.125N to 31.625 N; the temporal coverage of DT data goes from 01-01-1993 to 05-05-2016 (daily data) and NRT data from 05-06-2016 to 06-26-2017. Data collected after 06-26-2017 is no longer available on AVISO. It is distributed by CMEMS (<http://marine.copernicus.eu/sea-level-thematic-center-sl-tac/>), instead.

Processing of the satellite SSH data included first removing the steric signal, in order to obtain an altimetry signal that only reflects the mesoscale dynamics. The steric signal, related to large-scale warming (or cooling) for the Gulf of Mexico, introduces a seasonal variation in sea level that has no dynamic effect (Figure 2-5).

The steric signal for each daily SSH field is calculated by spatial averaging in the region with depths greater than 200m, $\langle \text{SSH} \rangle_{>200\text{m}}$ (Figure 2-6). The depth mask used to calculate the spatial average was generated by interpolating the GoM bathymetry data to the AVISO grid and eliminating the points where the depth was less than 200m. This 200m mask was made with the dual purpose of eliminating the effect of shallow

areas, where the heating (or cooling) has a greater steric effect, and eliminating spurious data generated near the coastal zone due to ground contamination of the measured signal by the satellites.

Then, the altimetry field without the steric signal is obtained by subtracting the spatial average from the daily SSH field, as follows:

$$SSH_{i_ns} = SSH_i - \langle SSH_i \rangle_{>200m},$$

Where "i" refers to the day on which the spatial averaging was performed.

The data was downloaded from the ftp server <ftp.aviso.altimetry.fr>, using a username and password. In order to allow verification of processing, raw data is included in the Aviso database.

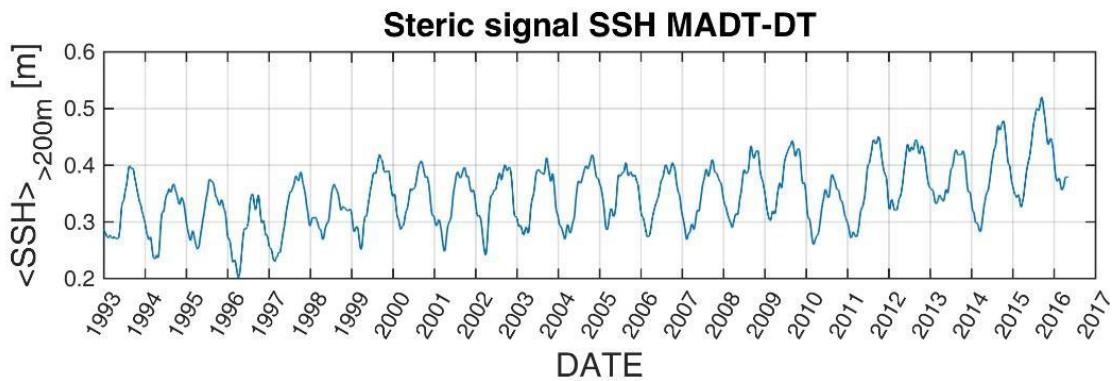


Figure 2-5: Time series for SSH Steric Signal (m) from AVISO DT-MADT-H-UV data.

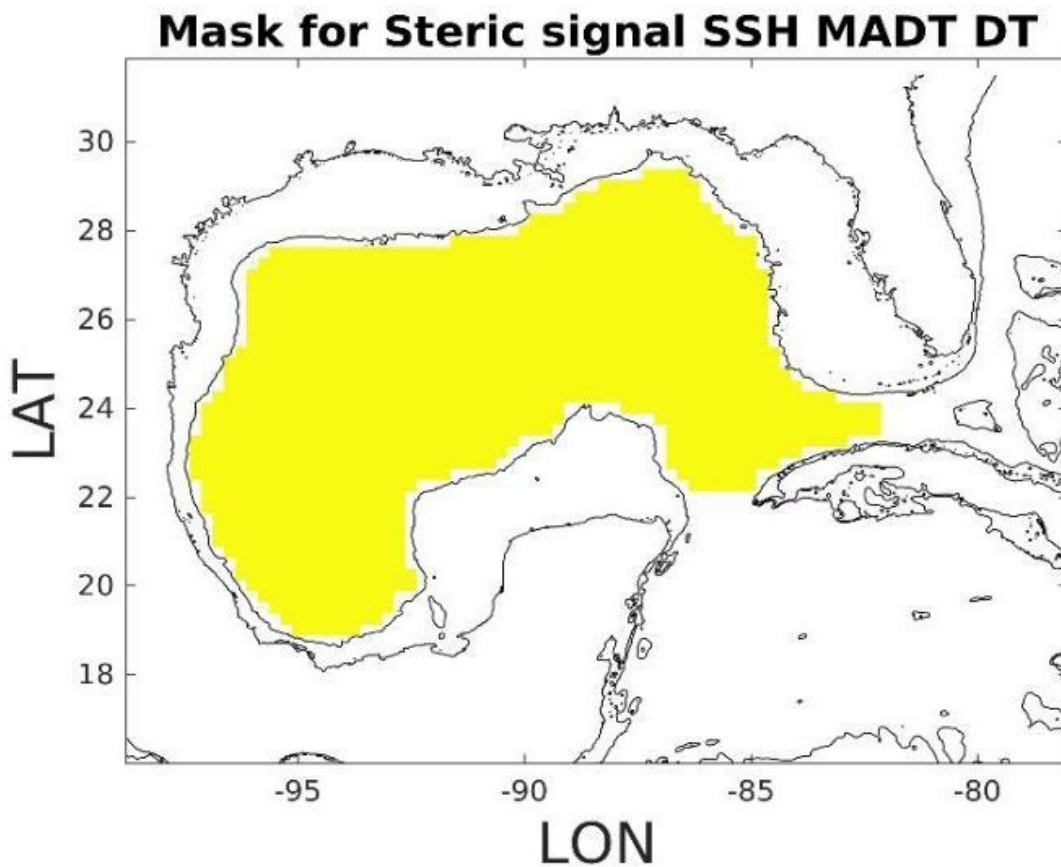


Figure 2-6 Gulf of Mexico region where the SSH spatial average was performed.

Processing the altimetry data for the eddy-detection algorithm, diagnostics, and SSH-RAFOS drift comparisons followed a slightly different approach. The seasonal steric height cycle was computed using the mode of the daily SSH distribution, which corresponds to the Gulf Common Water's SSH. The time series data were then low-pass filtered using a fourth order Butterworth filter with a cut-off period of 10 days. Once this periodic signal was removed, the mode of the distribution of the resulting SSH dataset was removed, so that the zero-SSH value corresponded to Gulf Common Water.

CHAPTER 3. BASIC STATISTICS

This study has generated the first dataset of upper layer (300 dbar) trajectories in the western Gulf of Mexico, and added to the existing earlier data in the lower layer (1500 dbar; Hamilton et al., 2016). Data from 83 floats were collected between June 2016 and January 2019 (Section 2; Figure 2-2; Ramsey et al. 2019). The results discussed here include data from 80 floats: 40 ballasted for 300 dbar and 40 ballasted for 1500 dbar. Short mission floats, some deployed at 1000-m, were used to return data on sound source signal strength. These 1000-m monitor floats (S/N 1070 and S/N 1119) are not included in the final dataset. Float S/N 1539 is also omitted as it only recorded temperature and pressure data.

3.1 FLOAT MISSION LENGTHS

Float mission lengths for the DWDE project were programmed for 127, 300, 365, or 540 days, with the majority being 540 days. In order to coincide with the field program end date, mission lengths for the fourth and fifth float deployments were shortened to 365 and 300 days, respectively. There were two 127-day monitor floats deployed at 1500 dbar. All 40 of the deep floats that surfaced completed a full mission, whereas, the unforeseen ‘shark bite’ issue (See Section 2 and Ramsey et al. 2019) meant that only eight of the 40 shallow water floats that surfaced completed full missions.

The resulting float mission lengths ranged from six to 540 days (Figure 3-1). Mission lengths greater than 360 days had the highest data return (54%); 16% of the mission lengths were between 180 to 360 days, lowest rate of return; and 30% of the mission lengths were less than 180 days (Table 3-1).

The 300-dbar floats had the shortest mission lengths (Figure 3-1, Table 3-2). Of the 40 floats ballasted for 300 dbar, 55% had mission lengths less than 180 days; 25% had mission lengths between 180 and 360 days; and only 20% had mission lengths greater than 360 days. The floats ballasted for 1500 dbar completed the longest missions: 88% greater than 360 days; 7% between 180 and 360 days; and only 5% less than 180 days (Figure 3-1, Table 3-2).

	> 180 day	180 – 360 days	< 360 days
All Floats	30%	16%	54%
300-dbar floats	55%	25%	20%
1500-dbar floats	5%	7%	88%

Table 3-1. Percentage of float mission lengths less than 180 days, between 180-360 days, and greater than 360 days.

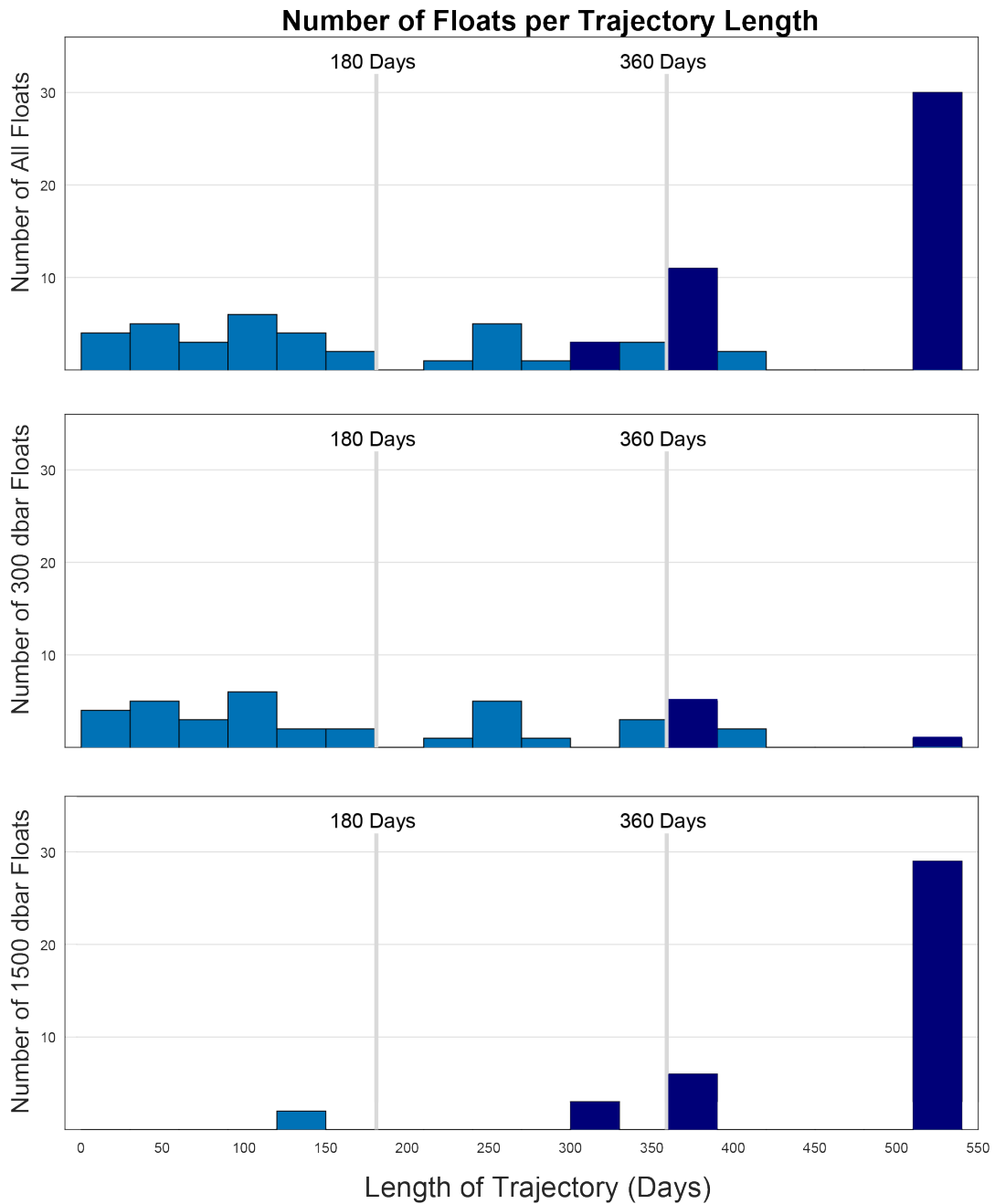


Figure 3-1. Histogram showing the number of floats per completed mission length. Top panel shows all floats, middle panel shows 300-dbar floats, bottom panel shows 1500-dbar floats. Dark blue indicates the float completed its full programmed mission; lighter blue indicates the mission was terminated early, either by ‘shark bite’ or another unknown process.

3.2 NUMBER OF FLOATS PER MONTH

An average of 30 floats were in the water collecting data each month over the 31-month field experiment, from June 2016 through January 2019. As seen in Figure 3-2 and Table 3-2, the highest concentration of floats in the water collecting data occurred in November 2017 (60 floats) and December 2017 (59 floats) and the lowest concentration of floats occurred in December 2018 and January 2019, with only three floats.

The highest concentration of 300-dbar floats in the water collecting data also occurred in November 2017 (25 floats) and December 2017 (24 floats). The fewest number of floats occurred between December 2018 and January 2019, with no floats collecting data during that time. The average number of floats in the water per month was nine floats.

The floats ballasted at 1500 dbar had the highest monthly average of floats with 21 floats per month. Similar to the 300-dbar floats, the highest concentration of 1500-dbar floats occurred in November 2017 and December 2017 with 35 floats in the water each month. The fewest occurred in December 2018 and January 2019 with only three floats in the water each month.

Time period: June 2016-January 2019	Most	Fewest	Average
All Floats	60	3	30
300-dbar floats	25	0	9
1500-dbar floats	35	3	21

Table 3-2. Number of floats in the water per month during the DWDE experiment, June 2016 through January 2019.

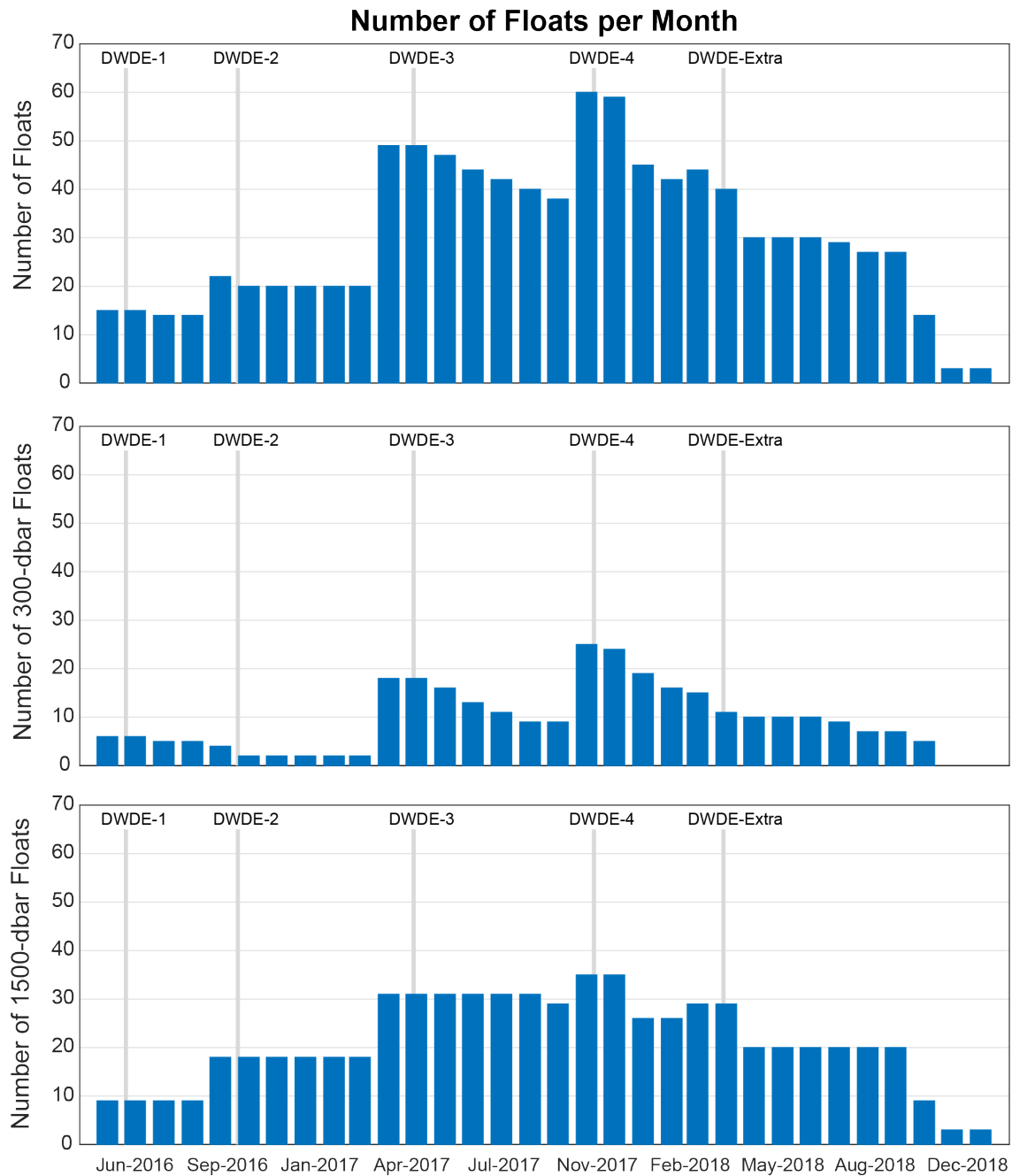


Figure 3-2. Histogram showing the number of floats in water per month during the DWDE field experiment, June 1, 2016 to February 1, 2019. The cruise name is depicted in gray. Top panel is all floats, middle panel is 300-dbar floats, bottom panel is 1500-dbar floats.

3.3 FLOAT SPEED

The 300-dbar floats: The range of along-track speed, calculated from the centered first difference between positions separated by 16 hours, for the 300-dbar floats was 0.02-102 cm s^{-1} with a mean of 13.4 cm s^{-1} (Table 3-3). The speed range 5–10 cm s^{-1} had the highest percentage of floats (28%). The maximum speeds were found in the Perdido Escarpment area (Figure 3-3). The lowest speeds were found over the Sigsbee Abyssal Plain and Campeche Escarpment.

The 1500-dbar floats: The mean along-track speed for the 1500-dbar floats was 5 cm s^{-1} (Table 3-4). The minimum speed was 0.03 cm s^{-1} and the maximum speed was 35 cm s^{-1} . The speed range 2–4 cm s^{-1} had the highest percentage of floats (29%). In contrast to the upper-layer floats, the highest speed values were found over the Sigsbee Abyssal Plain with low flow speeds distributed around most of the study area (Figure 3-4).

Speed Range (cm s^{-1})	Percentage of 300-dbar floats
0 – 5	17%
5 – 10	28%
10 – 15	21%
15 – 20	14%
20 – 25	8%
25 – 30	5%
30 – 35	3%
35 – 40	2%
40 – 45	1%
< 45	1%

Table 3-3. Speed ranges for 300-dbar floats.

Speed Range (cm s^{-1})	Percentage of 1500-dbar floats
0 – 2	18%
2 – 4	29%
4 – 6	22%
6 – 8	13%
8 – 10	8%
10 – 12	5%
12 – 14	2%
14 – 16	1%
16 – 18	1%
> 18	1%

Table 3-4. Speed ranges for 1500-dbar floats.

Scatter plot of speed for all 300-dbar floats

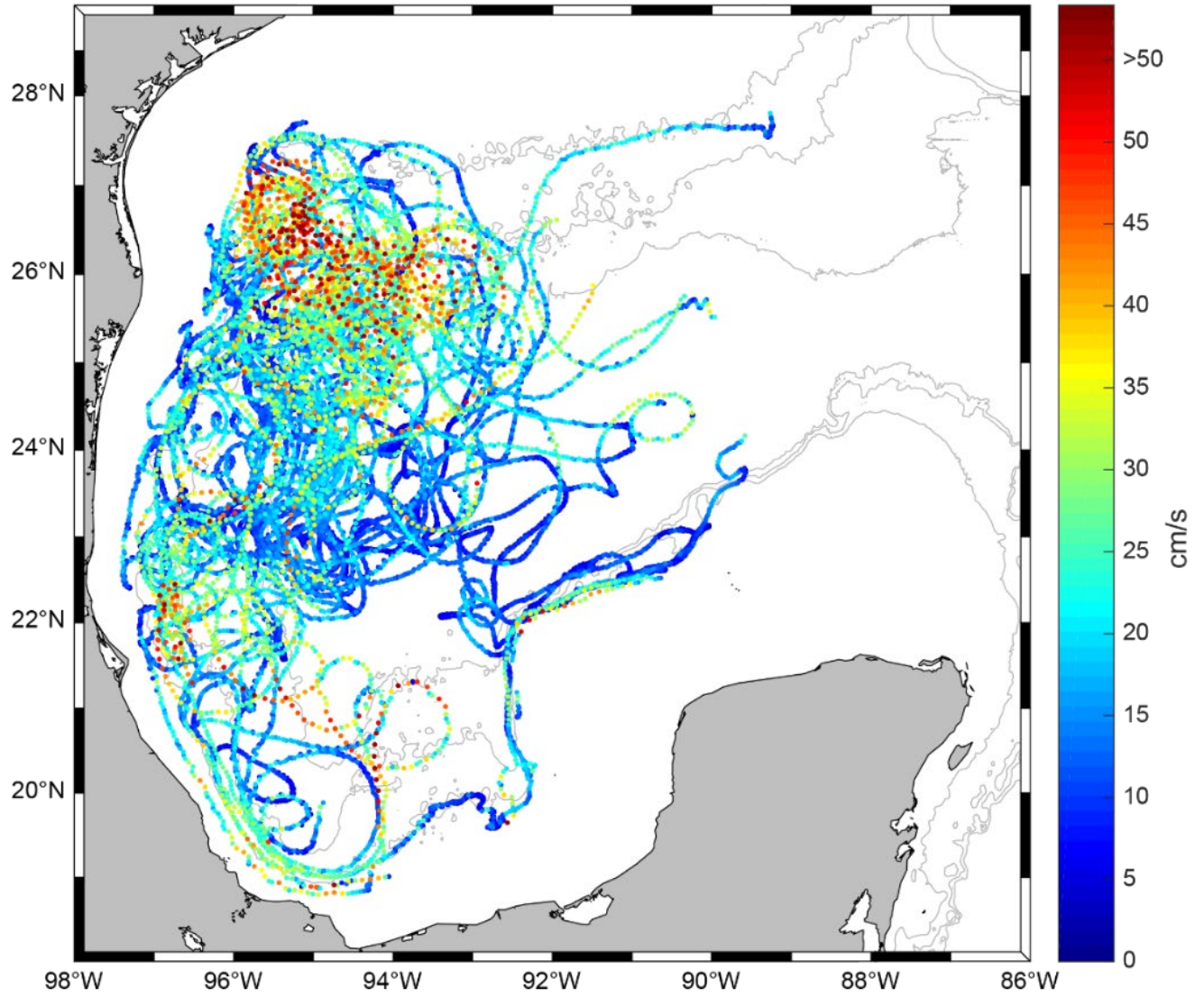


Figure 3-3. Spaghetti plot of 300-dbar float speed. The 1000-, 2000-, and 3000-m isobaths are drawn. Note the color scale is 0 to $>50 \text{ cm s}^{-1}$.

Scatter plot of speed for all 1500-dbar floats

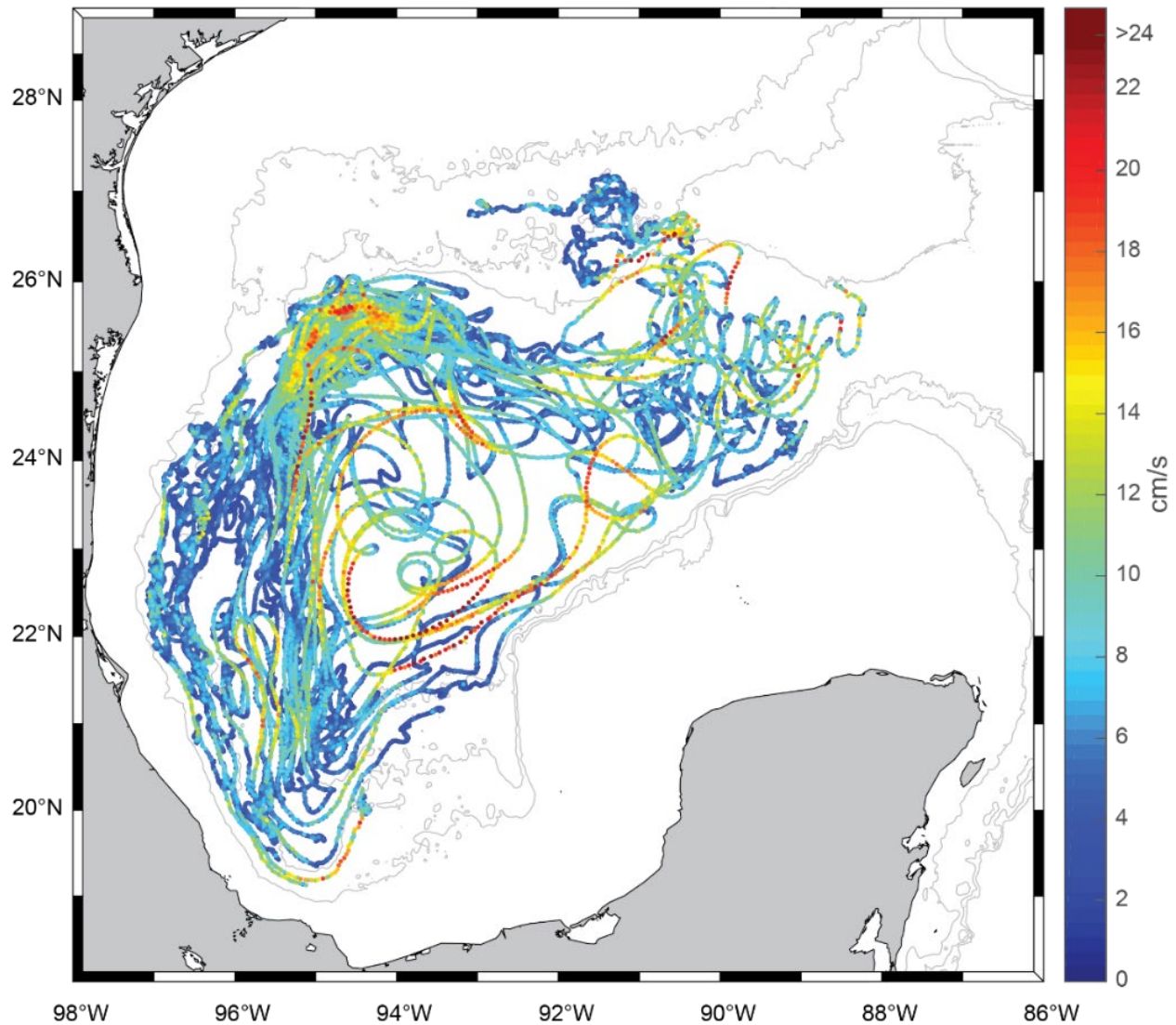


Figure 3-4. Spaghetti plot of 1500-dbar float speed. The 1000-, 2000-, and 3000-m isobaths are drawn. Note the color scale is 0 to >24 cm s^{-1} .

3.4 FLOAT DISPLACEMENT

Float displacements for both upper- and lower-layer floats are shown in Figure 3-5. Only the floats that had mission lengths of 250 days or greater are shown. The DWDE-3 (June 2017) 300-dbar float displacements were predominantly to the east, while the DWDE-4 (November 2017) 300-dbar float displacements were to the south. In the deeper layer, all deployments tend to have displacements that are both to the east and south, with the exception of the DWDE-extra floats, which were launched over the Sigsbee Escarpment rather than the Perdido slope. Floats from both the upper and lower layer have examples of floats that terminated their mission east of 90°W, in the eastern Gulf.

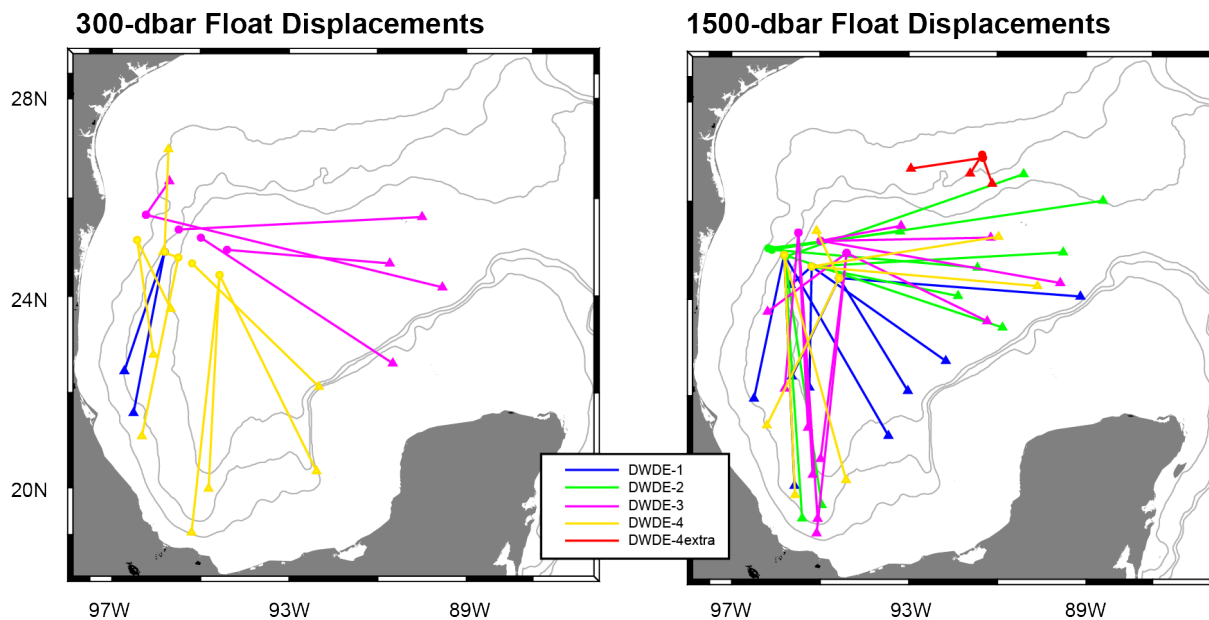


Figure 3-5. Displacements for 300-dbar (left) and 1500-dbar (right) floats with trajectory lengths of 250 days or greater, color-coded by deployment (see legend). The 1000-, 2000-, and 3000-m isobaths are drawn.

3.5 “LOOPINESS” RATIO

Fratantoni and Richardson (1999) used a value called the Loopiness Ratio to as a measure of the eddying of float trajectories. The Loopiness Ratio is the total along-track distance traveled versus the displacement of the float. A value of one, where the displacement and the distance traveled are equal, reflects a float traveling in a straight line, without any looping or meandering. The higher the value, the larger the distance traveled compared to the displacement, indicating more looping and meandering, which is indicative of energetic eddies and meanders in a weak mean flow. The lower the ratio, the lower the energy of the eddies, allowing the mean flow to dominate.

The overall Loopiness Ratio for all floats was low, with more than half the floats in the 1-10 range (Table 3-6, Figure 3-6). This indicates that the overall energy of the system was dominated by the mean flow. There were a couple of shallow floats that had very high looping ratios (>90). These floats were trapped in ~100km diameter eddies for most of their lifetimes, and surfaced quite close (a few 10s of km) to where they were launched. The Loopiness Ratio of the individual floats shown in the next section are float_serial_number: looping_ratio [1456:6; 1472:4; 1533:4; 1526:11; 1516:9; 1481:10; 1504:5; 1513:7; 1509:13].

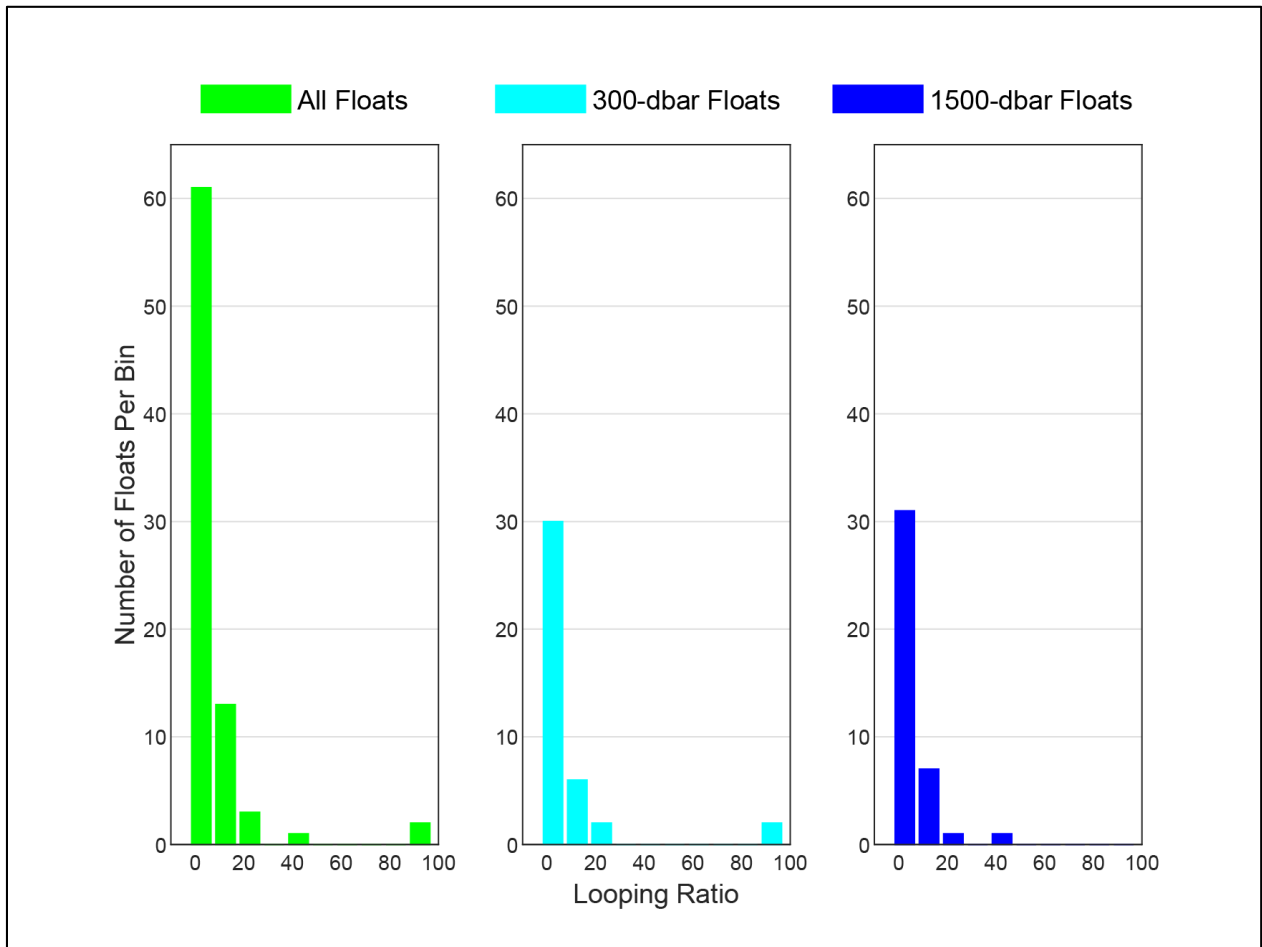


Figure 3-6. Loopiness Ratio, or distance travelled normalized by displacement for all floats (left), 300-dbar floats (middle), and 1500-dbar floats (right). The total number of floats is 80, 40 shallow and 40 deep.

Loopiness Value	Least Looping ←————→ Most Looping						
	1-10	11-20	21-30	31-40	41-51	51-90	91-100
Number of values within bin for all floats	61	13	3	0	1	0	2
Percentage of total for all floats	76	16	4	0	1	0	3
Number of values within bin for 300-dbar floats	30	6	2	0	0	0	2
Percentage of total for 300-dbar floats	75	15	5	0	0	0	5
Number of values within bin for 1500-dbar floats	31	7	1	0	1	0	0
Percentage of total for 1500-dbar floats	78	18	3	0	3	0	0

Table 3-5. Loopiness Ratios and percent Loopiness for all floats, 300-dbar floats, 1500-dbar floats.

3.6 INTERESTING EXAMPLES

The Lagrangian dataset revealed a variety of flow patterns in the upper and lower layers of the Gulf. In general, the flow patterns of the 1500-dbar floats are similar in nature to the previous deep RAFOS float study presented in Hamilton et al. (2017). The upper-layer float patterns presented here are the first Lagrangian particle pathways observed at this depth in this region. The following set of figures illustrate eight particularly vivid examples of current motions observed by floats.

Note that often the 300-dbar float missions were shorter than the programmed mission lengths, as these shallow floats were plagued by so-called ‘shark bites’. As near as we can tell, the float drop-weights, which keep the float at their intended depths, were yanked off by large marine predators. The float, immediately becoming much more buoyant, surfaces, and transmits its data. Several floats found later showed evidence of this type of catastrophic mission end. We consulted marine biologists who postulated that the predators were either sharks or swordfish, both of which hunt at the ballast depth of the 300-dbar floats. For the three upper-layer examples provided below (floats 1504, 1509, 1513), the actual mission lengths ranged from 11-18 months. The deep 1500-dbar floats did not encounter this problem, and completed their full missions.

FLOAT 1509, 300 DBAR:

Float 1509 shows a particularly vivid example of an upper-layer (0-1000 dbar) float trapped in two anticyclones found at different locations in the western Gulf (Figure 3-7). Many of the upper layer floats were trapped in this scale eddy. These ~50-100 km diameter eddies are likely remnants of LCRs that have pinched off from the Loop Current in the east and drifted westward to the so-called eddy graveyard. Float 1509 was launched in the Perdido region in the northwestern Gulf, in late April 2017, directly into an anticyclonic eddy. The float remains in the eddy for about 5 months, tracing out loops at speeds of about 50 cm s^{-1} that range from ~100 km in April, down to ~50 km by mid-September. The eddy remains nearly stationary, pressed against the western slope. The float is then ejected from the eddy and advected in an anticyclonic arc south to the Bay of Campeche. Once it reaches the slope, it travels cyclonically around the southwestern portion of the Bay at about 25 cm s^{-1} . The float is then trapped in a second anticyclone on the eastern side of the Bay. This anticyclone, with the float embedded in it, travels westward across

the Bay from December 2017-February 2018, while the float traces out loops of about 100 km diameter, at speeds about 50 cm s^{-1} . Once the float reaches the western slope, it is again re-oriented to drift along the boundary, tracing out a cyclonic path around the southwest Bay of Campeche, in a nearly identical path and at a similar speed as it did several months earlier. After the float's second journey around the Bay of Campeche, it takes a different route when it reaches the east side of the Bay. Tracking was lost when the float crossed the Campeche Knolls. Once tracking resumes, the float crosses the Campeche Canyon, begins to follow along an apparent boundary current which rounds the northwest Campeche corner, and then drifts along the Campeche Escarpment (25 cm s^{-1}). The float's mission ends in April 2018, as the float is travelling eastward along the Campeche Escarpment.

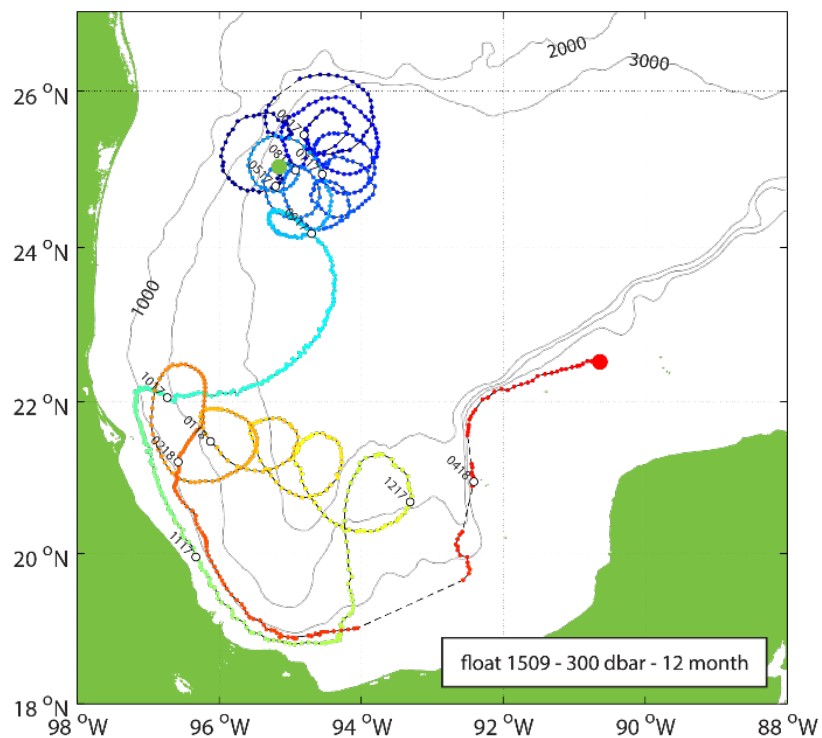


Figure 3-7. Trajectory of the 300-dbar float 1509. Color along the trajectory is a measure of time (from blue at the beginning of the track to red at the end) and circles are plotted at the beginning of each calendar month, and marked 'YYMM'. The large green and red dots mark the beginning and end of the trajectory, respectively.

FLOAT 1513, 300 DBAR:

Float 1513, also an upper-layer float, was launched at the same time as the previous example, Float 1509, and was presumably originally embedded in the same anticyclonic eddy (Figure 3-8). However, this float meets a much different fate than 1509. Float 1513 was launched in the Perdido Region in the northwestern Gulf, in late April 2017, into an anticyclonic eddy, at a station slightly inshore/upslope of the previous float example. The float remains in the eddy for about 5 months, similar to the previous float example, but traces out much smaller size loops ($\sim 10\text{-}20\text{ km}$) and travels more slowly at $\sim 30\text{ cm s}^{-1}$, which indicates that this float was trapped closer to the center of the eddy. The float is trapped from April to September 2017, when, similar to the previous example, it is ejected from the eddy, tracing a cyclonic arc towards the western slope of the Gulf. Instead of drifting southward once it hits the slope as Float 1509 did, it is advected northward. This difference in trajectory path may be because this float reached the western boundary about 100 km northward of Float 1509. Float 1513 continues tracing out a large 200-300 km anticyclonic arc around the central slope region, then follows an undulating pathway northward and southward, moving east at about 20 cm s^{-1} until its mission ends in late January. This float illustrates a persistent feature of the upper-layer float trajectories: inertial motions. Embedded in the large-scale loops traced by the float are smaller, tighter loops with a period of about 24-30 hours (3-4 data points, where each dot on the plot is 8 hours apart in time). These inertial motions were present in many of the 300-dbar float trajectories, and also in the 1500-dbar float trajectories to a lesser degree, with smaller diameters. As such, many of the trajectories have a small-scale zig-zag appearance superimposed over the larger pathways traced by the floats.

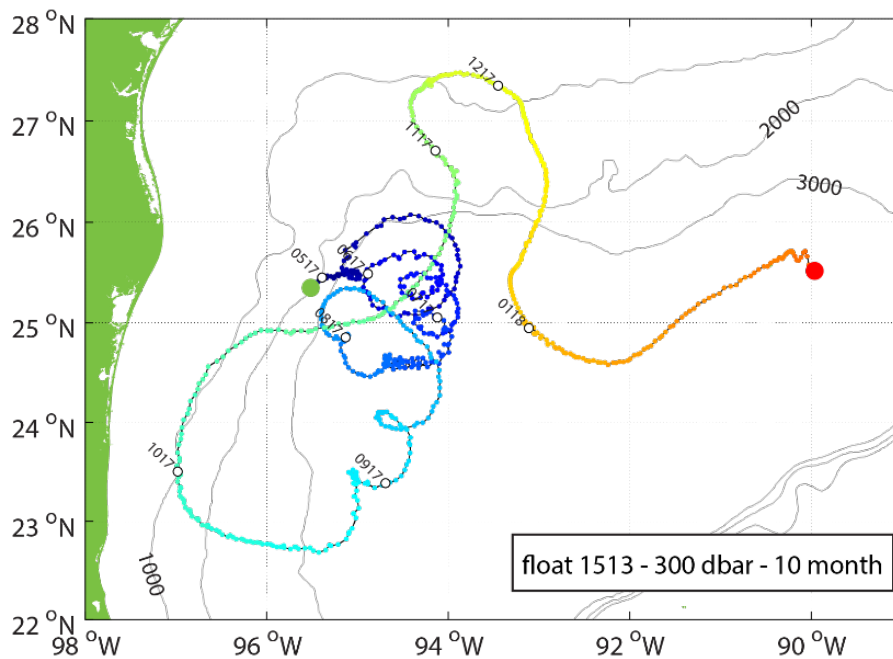


Figure 3-8. Trajectory of the 300-dbar float 1513, drawn as in Figure 3-7.

FLOAT 1504, 300 DBAR:

Float 1504 shows a third fate from the group of upper-layer floats deployed in April 2017 (Figure 3-9). In this example, the float was launched at a station inshore of the other two floats. This float shows no evidence of being trapped in the anticyclone present in the region (offshore) during launch. Instead, the float drifts slowly ($\sim 10 \text{ cm s}^{-1}$) through the Gulf for 18 months, first due eastward for a few hundred kilometers, then southward, then in a meandering fashion until it reaches the Campeche Escarpment at the northwest corner. One could imagine that this float is being advected along the outside of the existing eddies traced out by the previous two float examples. It reached the Campeche Escarpment in January 2018, about 8 months after launch. Once at the Escarpment, this float spends the next 10 months tracing out along-slope pathways ranging in length from several 10s to several 100s of kilometers. It is not obvious what causes these reversals in flow at this location, but the reversal resembles what will be shown in subsequent examples along the western Gulf slope. This float is one of the very few 300-dbar floats that remained untouched by attaching sharks for its full intended 18-month mission.

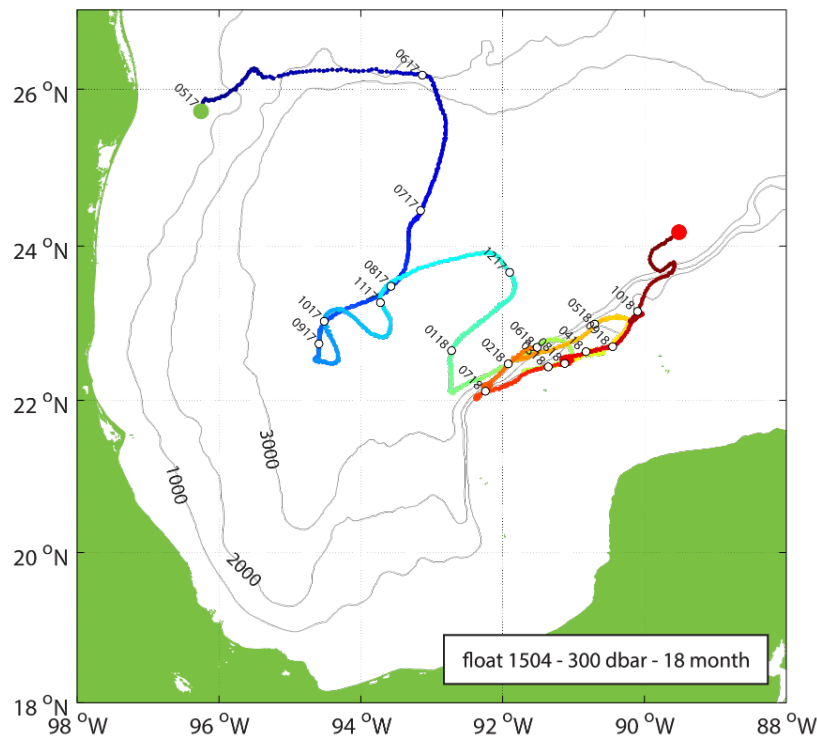


Figure 3-9. Trajectory of the 300-dbar float 1504, drawn as in Figure 3-7.

FLOAT 1481, 1500 DBAR:

Float 1481 was a deep-layer float launched in June 2016 during the first DWDE cruise on the *R/V Pelican* (Figure 3-10). In its 18-month journey, it traced out the approximate pathway of the Sigsbee Abyssal Gyre (SAG), which was determined to be in the deep flow field from a previous RAFOS float program (Pérez-Brunius et al. 2017). In other words, the SAG is still present in these deep data, and is a persistent feature of the deep circulation. The float shows a curious behavior, though, when it reaches the southwest corner of the SAG. Two times, in both fall 2016 (September–November) and summer 2017 (July–September), the float reverses its cyclonic journey around the SAG, and traces an angular anticyclonic circuit in the far southwest, over the deep (depth > 3000 m) basin of the Bay of Campeche. This deviation from the SAG, located in nearly the same place, at two different time periods is curious: is this a persistent circulation feature, or a remnant anticyclone(s) affecting the float advection? While in the SAG, the float is travelling at about 10 cm s^{-1} , and at 5 cm s^{-1} while in the anticyclonic circuits.

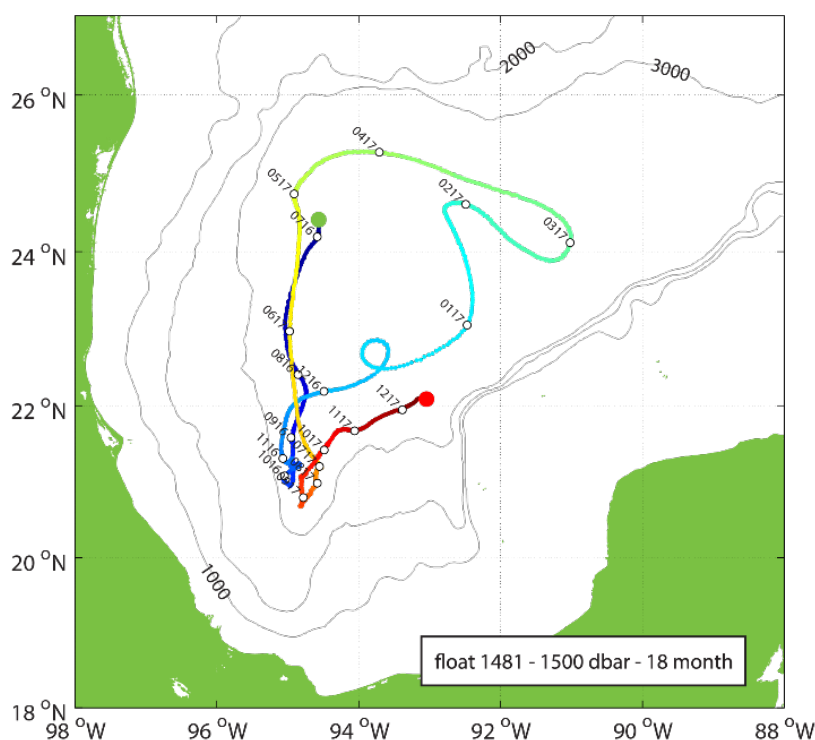


Figure 3-10. Trajectory of the 1500-dbar 18-month float 1481, drawn as in Figure 3-7.

FLOAT 1516, 1500 DBAR:

Float 1516 was launched about a year later, in June 2017, at a station located slightly inshore of the previous example, but still offshore of the 3000-m isobaths. This deep float exhibits an entirely different behavior (Figure 3-11). It shows no evidence of being trapped in the SAG, but does appear to be driven

by bathymetric constraints, generally following the isobaths along the western slope for the first 12 months of its mission. This float appears to be in part of the deep cyclonic boundary current, another persistent feature seen in the last float program (Case A, Figure 3-6, Hamilton et al. 2017, for an example; Pérez-Brunius et al. 2017). While in this boundary flow, this float exhibits the back-and-forth motion in both the far northwest corner of the Gulf (10-15 cm s⁻¹) and then in the southwest Gulf (5-10 cm s⁻¹). It may be that these motions are related to topographic Rossby waves, though this has not been proven. This behavior is also similar in nature to that seen with the previous group of floats (Case B, Figure 3-7, Hamilton et al. 2017, for an example). Once past the Bay of Campeche, the float travels across the Campeche Knolls, and traces the bathymetry along the Campeche Canyon and around the northwest corner of the Campeche Escarpment from July 2018 through the end of its mission in November 2018. This float is unique for this data set in that at the end of its trajectory the float is advected off the slope and begins to trace out an anticyclonic eddy, similar to those found in previous years (Case E, Figure 3-10, Hamilton et al. 2017; Furey et al. 2018). This is one of only two floats to end up in one of the anticyclones that were found in an earlier study to be generated at this location. As the float rounds the northwest corner and later diverts from the slope, it speeds up from 5 cm s⁻¹ to 15 cm s⁻¹. There were few 1500-dbar floats from this project that ended up along the Campeche Escarpment slope - most passed by this location farther offshore. There seems to have been little opportunity for this group of floats to become part of the boundary current or embedded in anticyclonic eddy formation at this location.

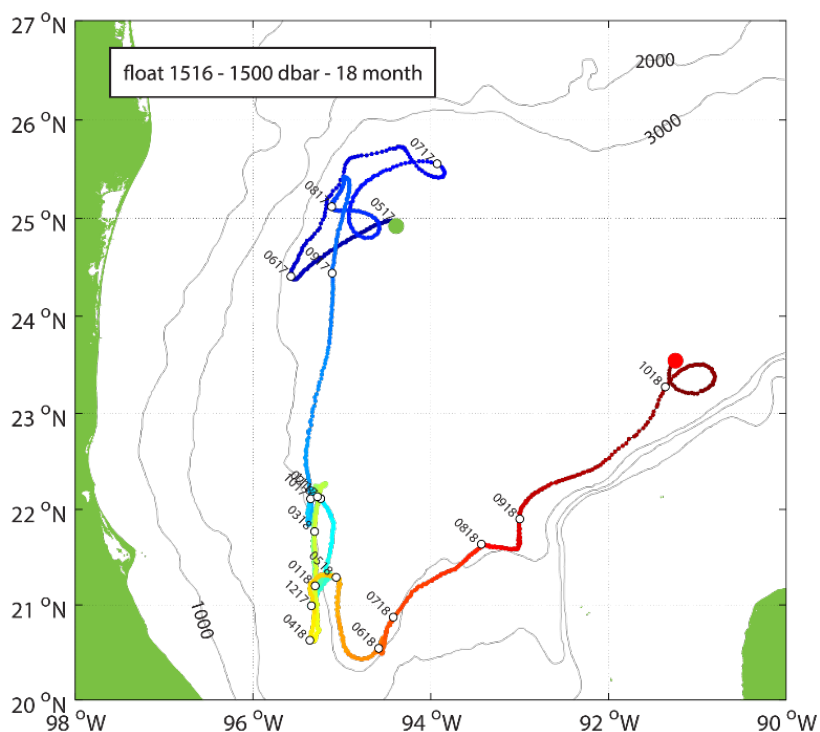


Figure 3-11. Trajectory of the 1500-dbar, 18-month float 1516, drawn as in Figure 3-7.

FLOAT 1526, 1500 DBAR:

Float 1526 exhibits behavior almost identical to what was seen in the last float program – see Case B, Figure 3-7 from Hamilton et al. 2017. The launch and surface location are in relatively close proximity after an 18-month underwater mission, belying the distance the float travelled in the same time period (Figure 3-12). For the entire 18 months, this float arced out back-and-forth along-slope motions ranging from tens to a few hundred kilometers in distance between reversals. Float speeds were between 5 and 15 cm s^{-1} . Perhaps this float is exhibiting a combination of behaviors: advection in the mean cyclonic boundary current, combined with advection along arcs of deep eddies and advection by topographic Rossby waves.

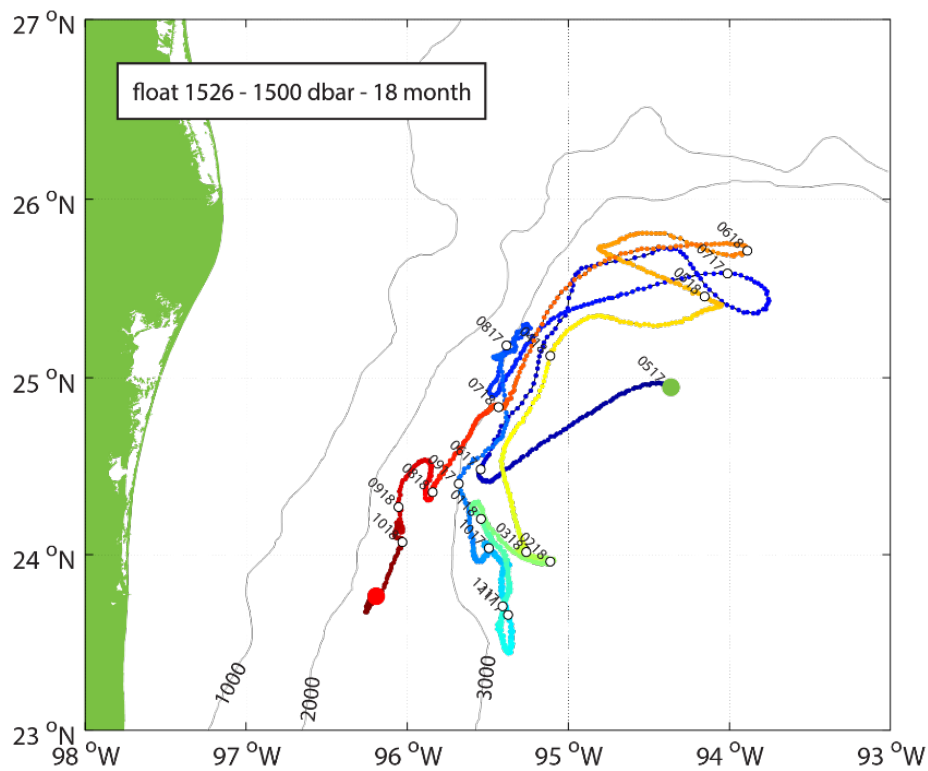


Figure 3-12. Trajectory of the 1500-dbar, 18-month float 1526, drawn as in Figure 3-7.

FLOAT 1533, 1500 DBAR:

Float 1533 shows a pathway from the western to eastern Gulf not often seen in the previous float program, and one contrary to the mean circulation of the lower-layer (Figure 3-13). This 12-month mission float was launched in December 2017, and surfaced a year later east of 90°W, in the eastern Gulf. It never participated in the cyclonic travel through the SAG or cyclonic boundary current around the perimeter of the western Gulf. Instead, this float travelled nearly due east for 9 months at about 10 cm s⁻¹, to about 88.5°W, whereupon it began a slow meander westward until it completed its mission east of 90°W in December 2018.

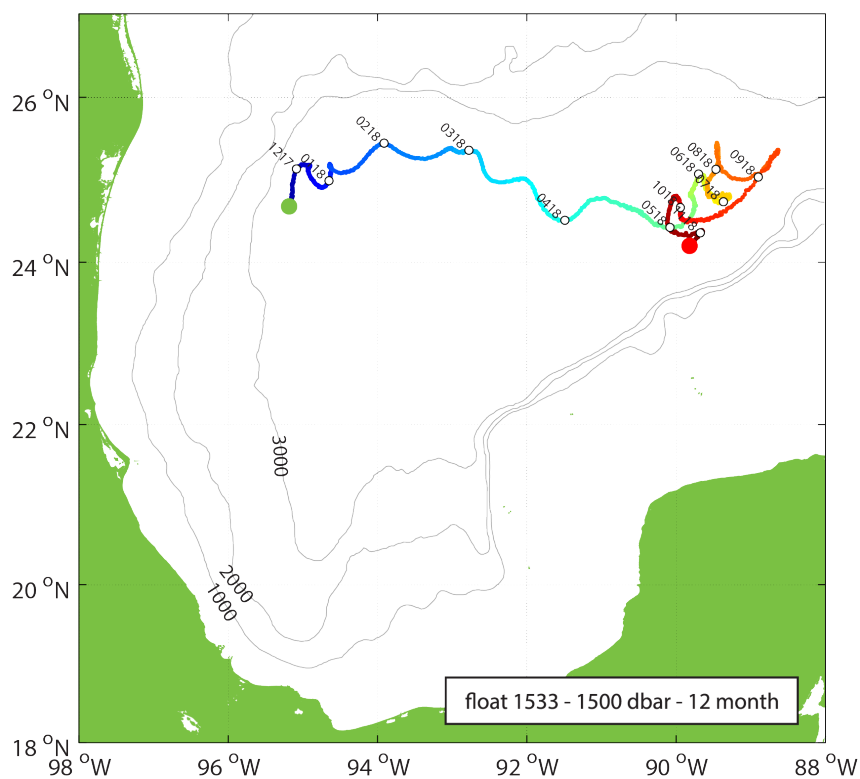


Figure 3-13. Trajectory of the 1500-dbar, 12-month float 1533, drawn as in Figure 3-7.

FLOATS 1456 AND 1472, 1500 DBAR:

The final example from our chosen case studies is one that illustrates a pair of floats launched at the same time and position during the second DWDE cruise in October 2016 (Figure 3-14). Almost all 300- and 1500-dbar floats were launched as pairs, triplets or even quadruplets, in order for the data to be used to study dispersion at these two depths. Floats 1456 and 1472 were launched on 17 October 2016 in about 3500-m water depth at the most offshore station of the DWDE cross-slope stations, surfacing on 10 April 2018.

What is remarkable about this pair of floats is that they stayed together, drifting in the same parcel of water, for about eight months. Both floats traveled through the SAG until about March 2017, and remained paired in a cyclonic angular meander just east of the SAG through June 2017. The continuous similarity in their pathways for at least eight months is remarkable. From June 2017 to April 2018, the floats meandered in distinct, nearby regions northeast of the SAG, traveling further apart. They surfaced about 400 km apart from each other in April 2018.

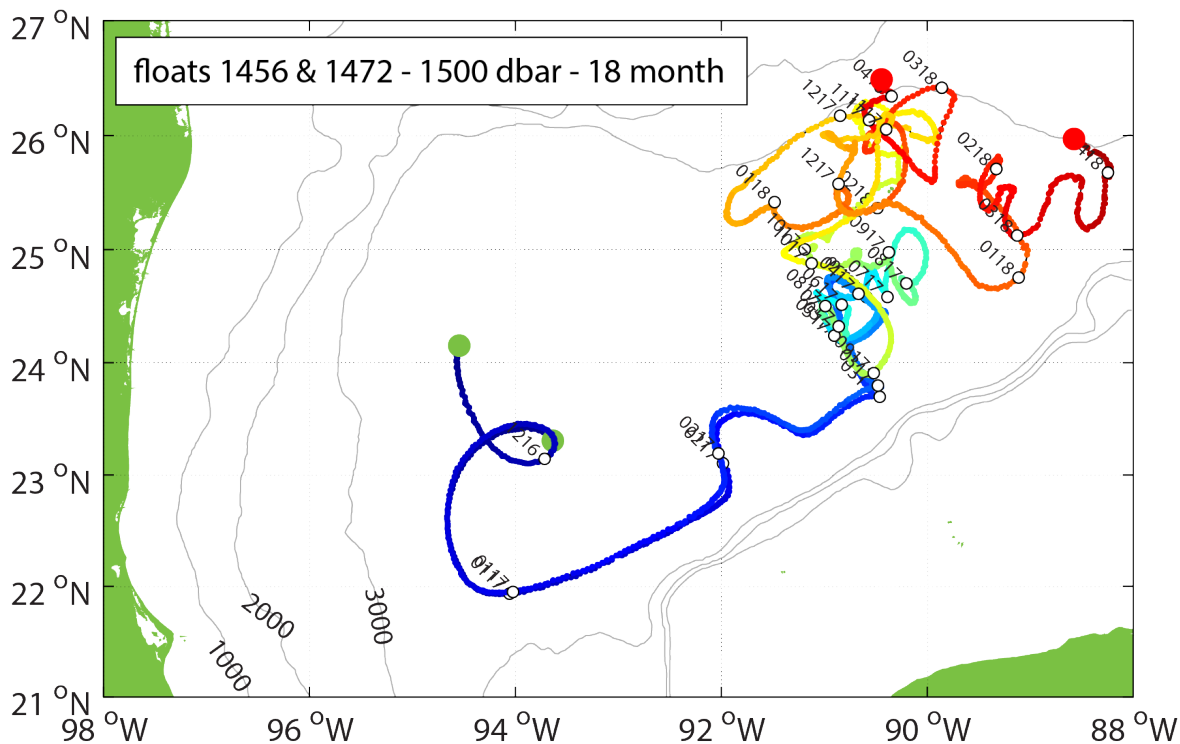


Figure 3-14. Trajectories of the 1500-dbar, 18-month floats 1456 and 1472, drawn as in Figure 3-7.

3.7 EDDY CENSUS

OVERVIEW

At times, the RAFOS floats were embedded in flow that exhibited looping motion, indicative of coherent eddies capable of trapping and transporting water (and floats). Tracking and kinematic description of upper layer eddies has been done numerous times using surface drifters (e.g., Hamilton et al. 1999). One similar study of deep (1500 dbar) eddies using RAFOS floats was documented by Hamilton et al. 2017 and Furey et al. 2018. Below will be the first time upper layer eddies will be kinematically described using subsurface floats.

METHOD

For this investigation, we will use a wavelet transform analysis technique (Lilly and Olhede, 2009a,b, 2010a,b, 2012) that allows for the analytical identification of eddies, yielding the objective determination of polarity, pathway, and kinematic properties. This same technique has been used before, with the relevant examples being Hamilton et al. (2017) and Furey et al. (2018).

A full description of the method may be found in Hamilton et al. 2017, and in Bower et al. 2013. In this study, we tuned the parameters to identify looping events of three rotations or more as an eddy, to align with the results of Hamilton et al. 2017. All input parameters mirrored those used in Hamilton et al. 2017, except for wavelet duration, a measure of allowed translation of an eddy through geographic space. In this study, wavelet duration was set to 2.5, where it had been set to 3 in the Hamilton et al. 2017 study: we found that using the lower value of 2.5 cut out a few wavelet identifications that seemed physically unrealistic. As in Hamilton et al. 2017, the minimum rotation period was cut off at twice the inertial period, where the single inertial period is approximately 39 hours at 19°N (five 8-hourly trajectory points) to 26 hours at 28°N (three 8-hourly trajectory points), meaning that all eddies included in our census were looping at a rate of at least twice the inertial period.

Algorithm output parameters include the segment of trajectory identified as positively being in rotation, the residual path of the trajectory once rotation is removed, and ellipse parameters of geometric mean radius, mean velocity, and Rossby number $Ro = V/2Rf$ (where V is the velocity, R is the radius, and f is the Coriolis parameter), or ω/f the ratio of the vertical component of relative to planetary vorticity. Because of edge effects, as shown by Bower et al. 2013, output was discarded for the first and last rotation periods; however, the residual trajectory was retained for the entire identified eddy duration.

RESULTS

Out of 80 float trajectories, 17 were identified to contain eddies of three loops or more, some with multiple independent eddies in the same trajectory. Out of the 80 floats with trajectories, many were short duration. In total 1,519 float days out of 25,680 float days were measured in eddies of three loops or more, or 6% of the total trajectory data. The 300-dbar floats were in eddies 17% of the time (1132 ft-days/6811 ft-days), while the 1500-dbar floats were in eddies only 2% of the time (387 ft-days/18869 ft-days). These percentages vary considerably depending on the number of loops used for the wavelet analysis, although the skew between upper- and lower-layer time spent in eddies (O(several) times more time in upper than lower layer) is similar no matter the choice of loop criterion. Table 3-6 lists the count of eddies sorted by float depth and sense of rotation. A nearly equal number of cyclones and anticyclones were found in this data set, and three times more eddies found in the upper-layer than the lower-layer data.

	Total # eddies	# anticyclones	# cyclones
All Trajectories	20	11	9
Upper layer (300 dbar)	13	6	7
Lower layer (1500 dbar)	7	4	3

Table 3-6. *Table of number of eddies by depth and sense of rotation.*

Eddies identified using the wavelet analysis are shown in Figure 3-15, separated into upper- and lower-layer eddy segments overlaid on the entire 300- or 1500-dbar trajectory data set. Most apparent is the larger number of eddies in the upper versus lower layers. A single example from the analysis is shown in Figure 3-16, to illustrate the technique. In this example, float 1496 was launched along the Perdido Escarpment (green dot) and meandered eastward until it was entrained in a westward drifting cyclone of about 40 km radius. The cyclone drifted westward and was measured by the float until the float's mission ended, and the float surfaced (red triangle). The swirl speed, or azimuthal velocity, was about 40 cm s^{-1} , looping period was about 10 days, and Ro was about 0.15. Each of the kinematic properties varied slightly over the measurement period. The green segments of the property time series are where edge effects occur - defined as one rotation period at the beginning and ending of each record (see appendix in Bower et al. 2013 - attached). The properties are considered accurate for the black portion of the record only.

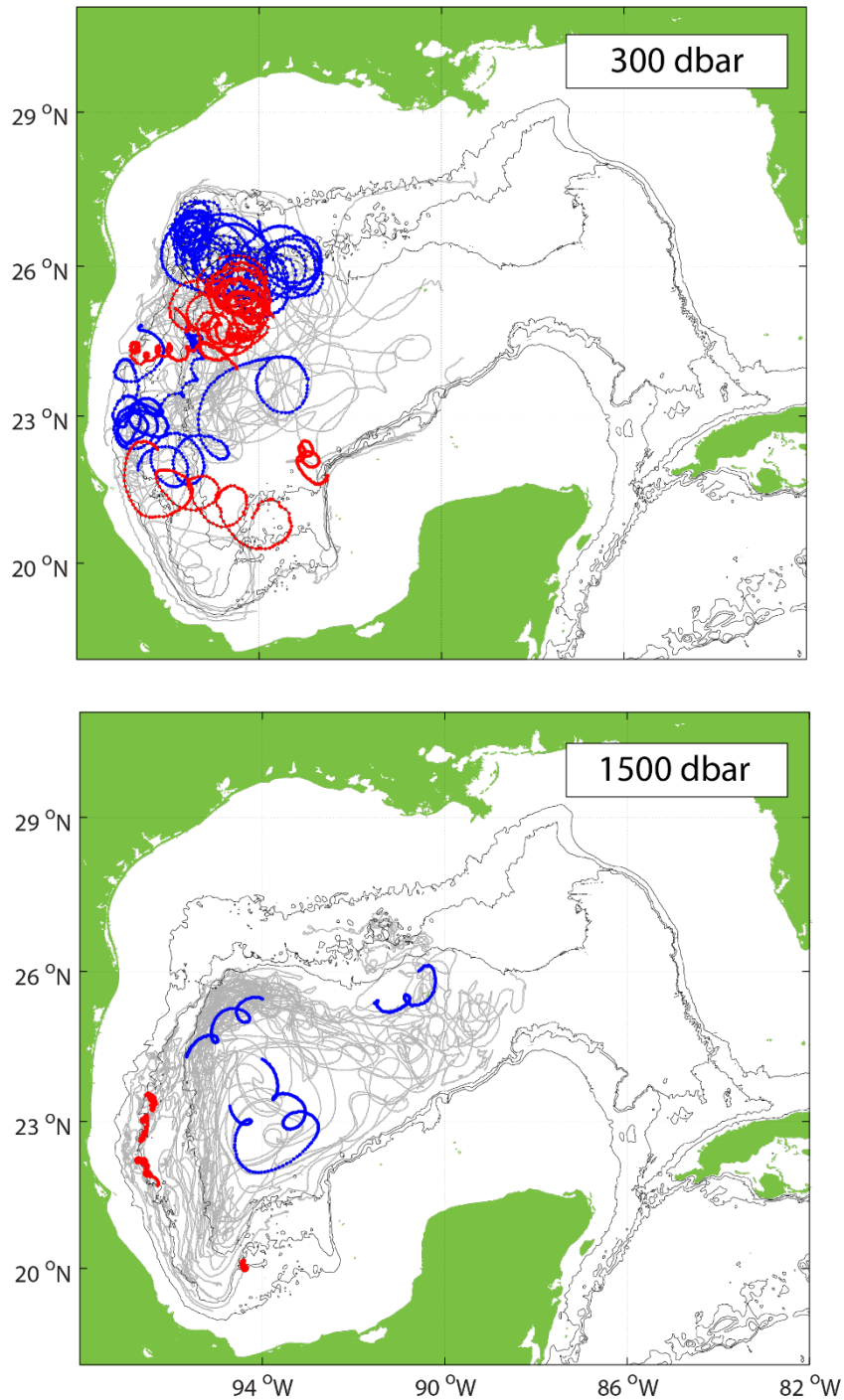


Figure 3-15. Trajectory eddy segments plotted by float pressure level. (top) All 300-dbar trajectories (gray), cyclonic trajectory segments (blue) and anticyclonic trajectory segments (red). Only eddies of 3-loops or more are highlighted. Dots plotted along eddy segments are 8-hourly. The 1000-, 2000-, and 3000-m isobaths are drawn.

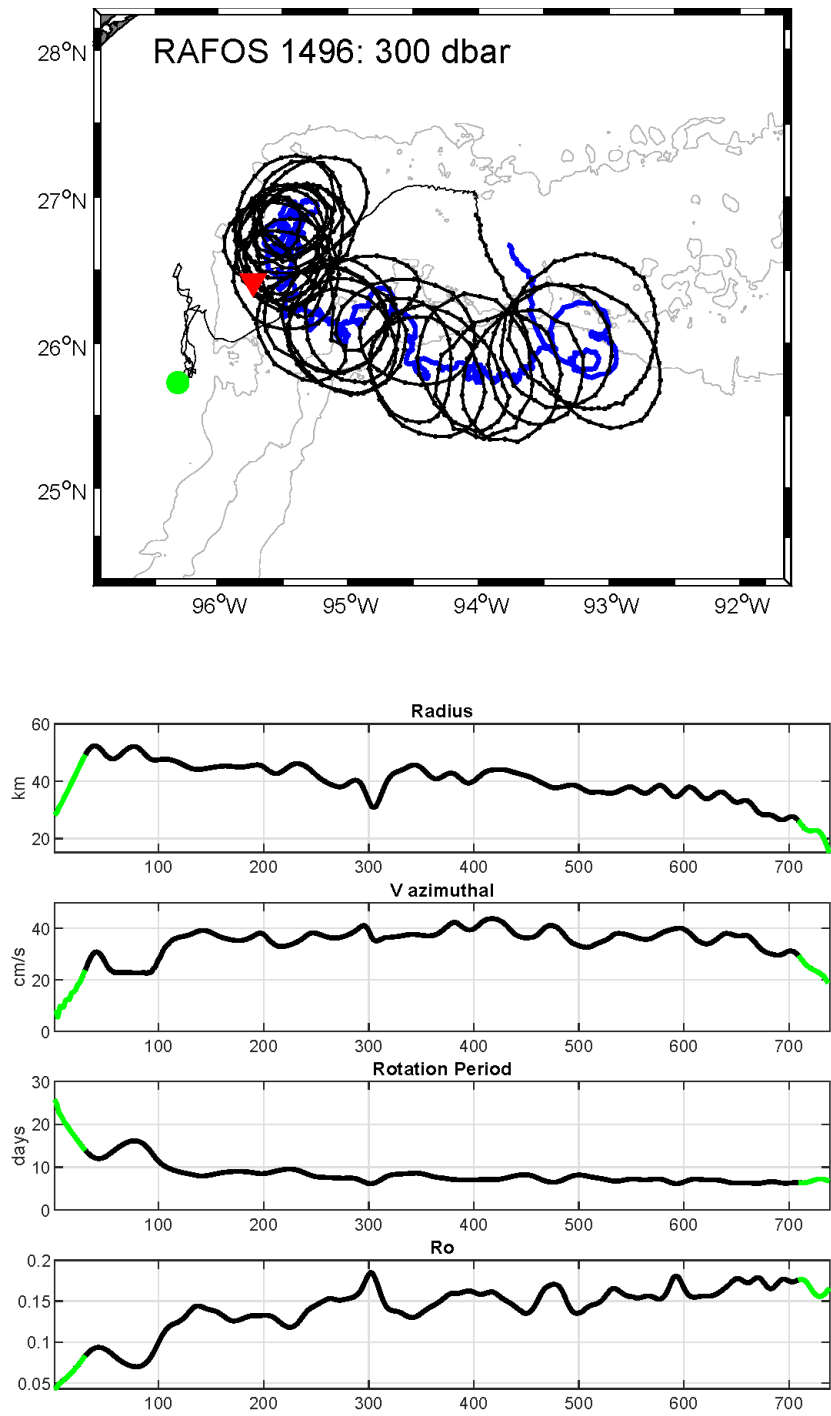


Figure 3-16. Example of an eddy. Trajectory segment identified as being in an eddy is rendered as a thick black line, and overlaid on the entire float trajectory (thin black). Residual trajectory is drawn in blue, and eddy kinematic properties of radius, azimuthal velocity, rotation period, and Rossby number versus record number are plotted in subplots underneath. Time interval is 8-hours.

The upper-layer dataset is unique, showing the prevalence of eddies of both polarities, all on the order of several 10s of kilometers radius. The lower layer panel of Figure 3-15 shows similarities when compared to the 2011-2015 data set presented in Hamilton et al. (2017) and Furey et al. (2018). In the previous study, 1500-dbar eddies were grouped into categories based on common characteristics. In this 2016-2019 data, we again find the 1500-dbar eddies falling into similar categories: ‘interior eddies’ are present in water depth greater than 3000 m and appear to be freely drifting with interior ocean currents. These eddies are the three cyclones seen in the lower panel of Figure 3-15. The remaining eddies captured in these data are ‘boundary eddies,’ which are small scale (~5 km radius) anticyclones following the boundary. They appear to be formed as the deep cyclonic boundary current interacts with rough bathymetric features, possibly spinning up anticyclonic eddies between the boundary current and slope. The eddy kinematic characteristics for each category are presented in Table 3-7. The sample sizes are low, so the statistics should be viewed with caution. On average, upper-layer cyclones and anticyclones have radii of about 35 km, azimuthal velocity of 18 cm s^{-1} , period of 13 days, and absolute value of Ro of 0.15. In the deep layer, the interior eddies are a bit smaller (27 km radius), slower (10 cm s^{-1} azimuthal velocity with 22 day period), and weaker (Ro order 0.1). The deep boundary eddies, similar to the previous deep float study, are relatively stronger with Ro of 0.26, and radius 4km, 6 cm s^{-1} azimuthal velocity, period 6 days.

Parameter (mean/std)	Upper Layer Eddies	Deep Interior Eddies	Deep Boundary Eddies
Sample Size	13	4	3
Radius (km)	35±20	27±12	4±1
Azimuthal Velocity (cm s^{-1} , absolute value)	18±7	10±4	6±2
Period (days)	13±7	22±6	6±3
Ro (absolute value)	0.15±0.11	0.07±0.02	0.26±0.08

Table 3-7. Eddy mean statistics by category.

One category of deep Gulf of Mexico eddy that was not clearly evident in this analysis were the anticyclones that are generated off the Campeche Escarpment, at the eastern edge of the Sigsbee Abyssal Gyre (e.g., Furey et al 2018). As can be seen in Figure 3-15, lower panel, only 5 floats passed by the northwest corner of the Campeche Escarpment, and most offshore. A blowup of this region (Figure 3-17) more clearly shows that two of the five floats were embedded in flow that began to form anticyclones just as the floats’ missions ended and the floats surfaced. Other floats that pass through what is the southern portion of the SAG, where the gyre comes in closest proximity to the wall of the Campeche Escarpment, also exhibit anticyclonic motions downstream of this location. But only the two floats rendered in bold in Figure 3-17 appear to possibly be capturing Campeche Escarpment Eddy (CEE) formation events. This behavior is similar to other anticyclones observed to form at this site: the float velocity accelerates as the float passes a horizontal ‘bump’ in bathymetry (at the southeast portion of the black section line, Figure 3-17), and the float exhibits anticyclonic curvature a couple of inertial periods after acceleration begins. Speeds of the floats passing through this portion of the SAG range from 2 to 20 cm s^{-1} . Unlike the few eddies observed in 2011-2015 (Furey et al. 2018), there is not a strong difference in speed between the floats that end up in possible eddy formation events, and one of the floats in the

gyre current. What is consistent is the cross-slope location of the floats that end up in possible CEEs versus floats that do not. The two floats in the CEEs are closer to the escarpment slope than the other three that pass the cross section point, and in a similar location as in the previous study.

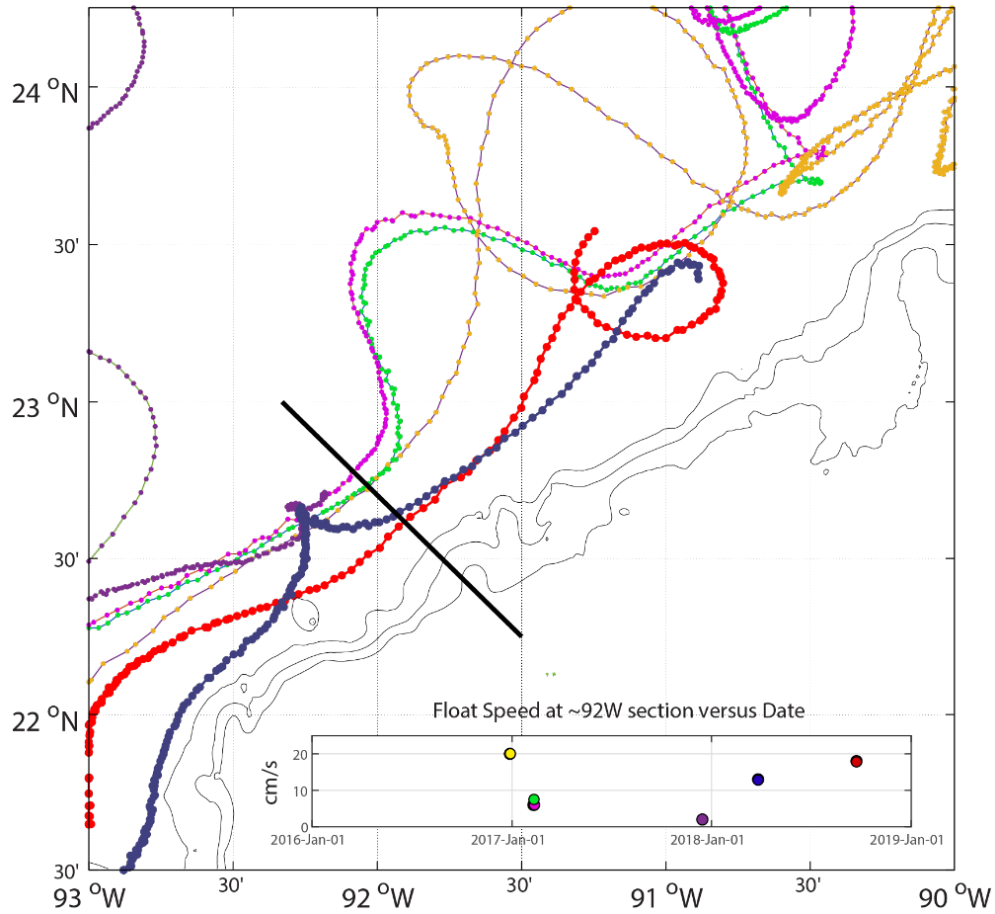


Figure 3-17: Deep anticyclone formation off of the Campeche Escarpment. Each 1500-dbar float is drawn in a different color; dots mark 8-hourly observations. Floats 1478 (dark blue) and 1516 (bright red) are in bold. Float surface positions are marked as triangles. The 1000- 2000- and 3000- isobaths are drawn. The bold back line that is drawn across the Campeche Escarpment marks the location where the float speeds were observed, and is located at the section used in Furey et al. (2018).

3.8 Lagrangian Integral Time Scales

The Lagrangian Integral Time Scale (LITS) is a fundamental variable in Lagrangian fluid mechanics. It is an estimate of the time needed for a particle's velocity to lose any correlation with previous measurements. The autocorrelation function and the LITS are defined as:

$$\begin{aligned}\vec{u}'(x, t) &= \vec{u}(x, t) - \langle \vec{u}(x, t) \rangle \\ R(\tau) &= \langle \vec{u}'(x, t) \cdot \vec{u}'(x, t + \tau) \rangle \langle \vec{u}'(x, t) \cdot \vec{u}'(x, t) \rangle^{-1} \\ T_l &= \int_0^\infty R(\tau) d\tau\end{aligned}$$

where T_l is the LITS, τ is the time lag, t is time, R is the autocorrelation function, u is the velocity and u' is the velocity anomaly.

In this work, LITS were computed for two distinct purposes:

1. Estimate the degrees of freedom of each grid point for the computation of a mean circulation from the float displacements. As the measurements of a single float become decorrelated in time, ergodicity can be assumed. One long time series can then be considered as a set of independent shorter time series and the number of degrees of freedom is increased.
2. LITS are also directly linked to single-particle dispersion and yield estimates of the diffusion coefficient D , which are key variables for the assessment of tracer diffusion in the deep GoM.

Single particle dispersion is defined as:

$$\langle \|\vec{\delta r}\|^2 \rangle = 2\langle \|\vec{u}'\|^2 \rangle T_l t$$

and the Taylor diffusion coefficient is:

$$D = \langle \|\vec{u}'\|^2 \rangle T_l$$

Autocorrelation functions against time lag are shown in Figures 3-18 and 3-19 for the 300-dbar and 1500-dbar RAFOS datasets. At both depths, autocorrelation decays exponentially with increasing time lag, with highly variable rates. Large amplitude oscillations are obvious in both 300 dbar and 1500 dbar examples, and correspond to floats circling around eddies. Integrating the autocorrelation functions with respect to time lag yields mean values of the LITS of 2.4 and 4.9 days for the 300-dbar and 1500-dbar floats, respectively.

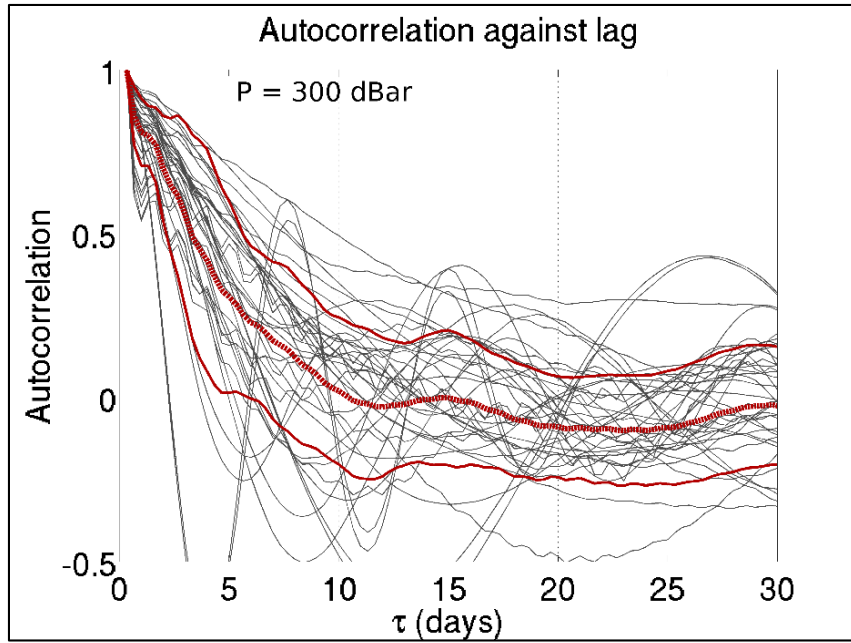


Figure 3-18. Autocorrelation of the velocity anomaly time series against time lag τ for the 300-dbar RAFOS dataset. The black lines are individual floats while the thick dashed red line represents the ensemble mean. The thin red lines represent two standard deviations.

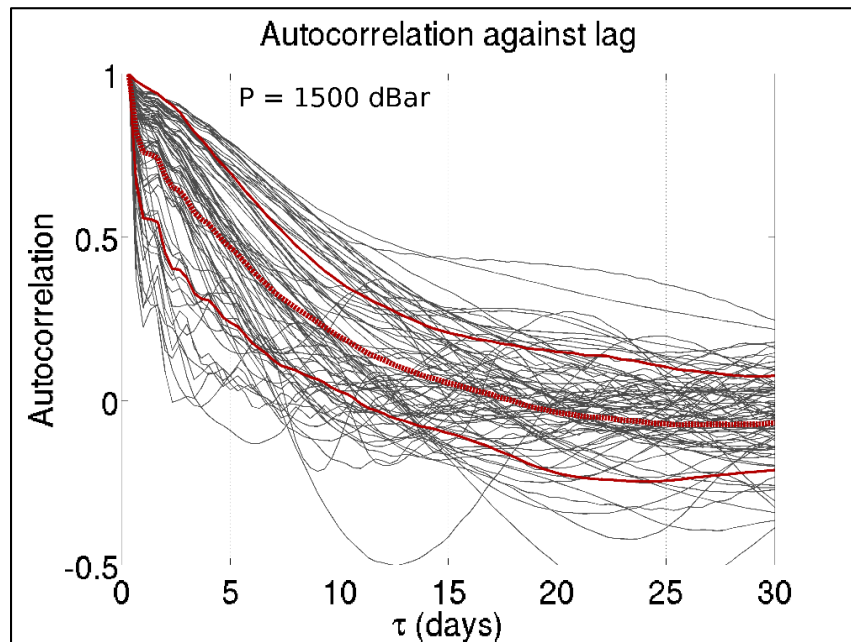


Figure 3-19. Same as Figure 3-18, but for the 1500-dbar RAFOS floats

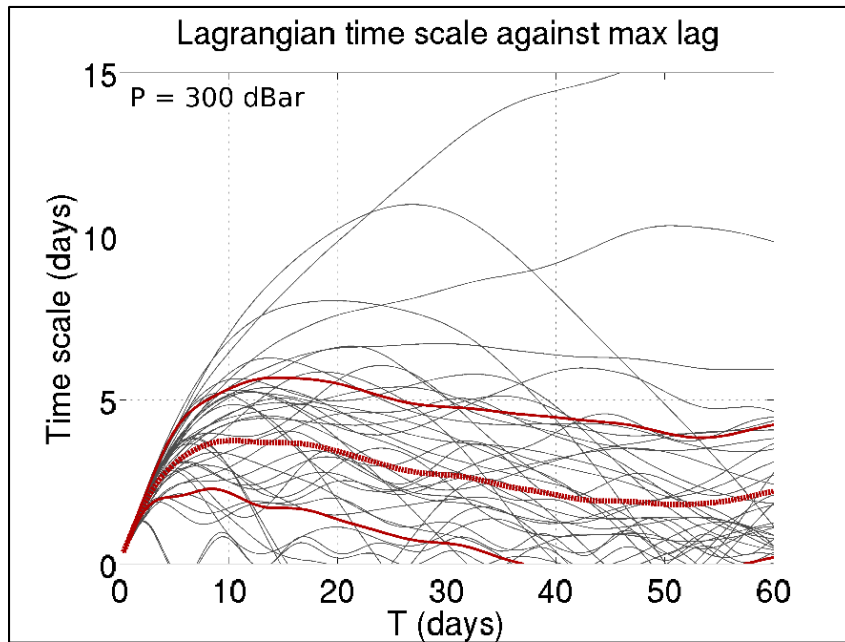


Figure 3-20. Lagrangian integral time scale against integration limit $T = \max(\tau)$ for the 300-dbar RAFOS floats.

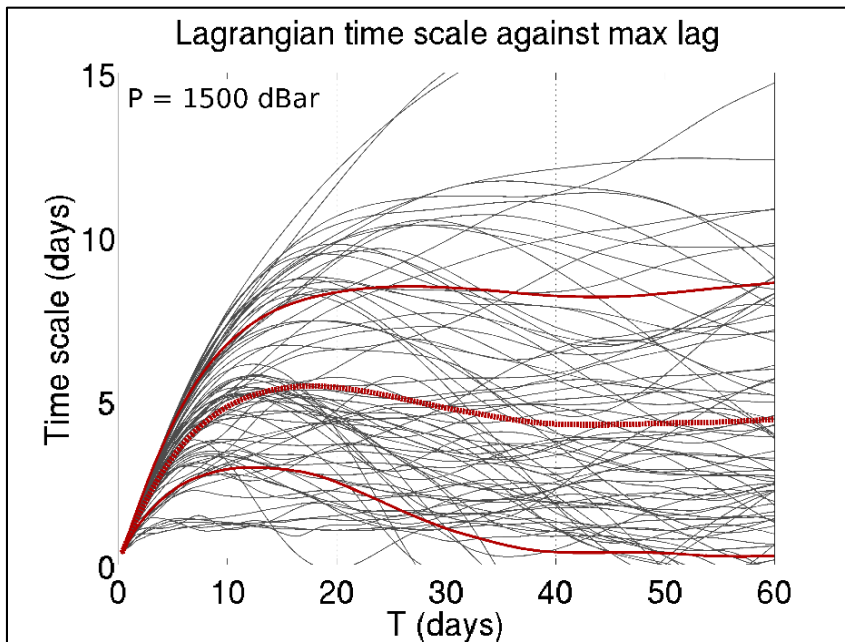


Figure 3-21. Same as Figure 3-20 for the 1500-dbar RAFOS floats.

In theory, autocorrelation functions should be integrated until infinity. To estimate a value for a reasonable maximum time lag, and the convergence of LITS with increasing time lag, we integrated the auto-correlation function over a wide range of time lags. LITS against maximal time lag is shown in Figures 3-20 and 3-21 for the 300-dbar and 1500-dbar data, respectively. While, on average, integrating over 10 days seems sufficient for LITS to converge for the 300-dbar floats, 15 days are necessary for the 1500-dbar floats. Note that there is significant variability and some cases never actually converge. For instance, this is observed in the cases of floats circling eddies, where the LITS oscillates rather than converging towards a final value. Large variability along with slow convergence of some floats should encourage prudence in the interpretation of LITS and derived variables.

It is of interest, however, to estimate the order of magnitude of the Taylor diffusivity. Histograms of diffusion coefficients are shown in Figure 3-22 at 300 dbar and 1500 dbar. At both depths, diffusivity values range over one order of magnitude: $[2500-17000] m^2s^{-1}$ for the 300-dbar floats and $[215-6000] m^2s^{-1}$ for the 1500-dbar floats. On average, diffusivity at 1500 dbar is smaller than at 300 dbar, with mean values of 2500 and $8000 m^2s^{-1}$, respectively.

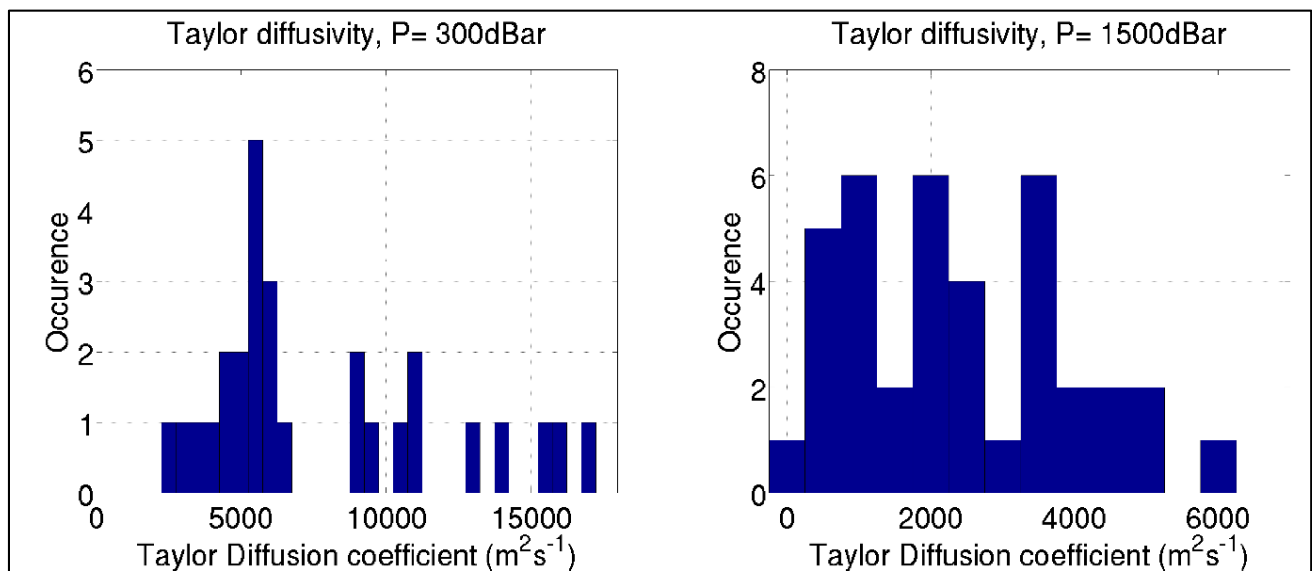


Figure 3-22. Probability density function of the Taylor diffusivity at 300- and 1500-dbar.

3.9 LOOP CURRENT RINGS

During the DWDE experiment, six distinct LCRs detached and drifted across the Gulf of Mexico. Figure 3-23 shows a diagram of their life cycles and interactions. For the simplicity of the nomenclature, rather

than using the names assigned to the eddies by the industry, we assigned them a letter. When an eddy splits, the subsequent eddies are assigned a subscript (e.g. A_1 and A_2). When two eddies merge, their name is concatenated (e.g. eddy AB). In some occasions, eddies experience several splitting and merging events, and this iterative naming procedure eventually results in complicated names (e.g. eddy $(CB_1(B_2(A_1A_2)_2)_1)_1$), that illustrate well the complex eddy interactions that take place in the western GoM. The eddies surveyed by DWDE RAFOS floats are labeled by purple text boxes in the diagram of Figure 3-23. The date ranges of the sampling of LCRs by the DWDE RAFOS floats is provided in the table included in the figure.

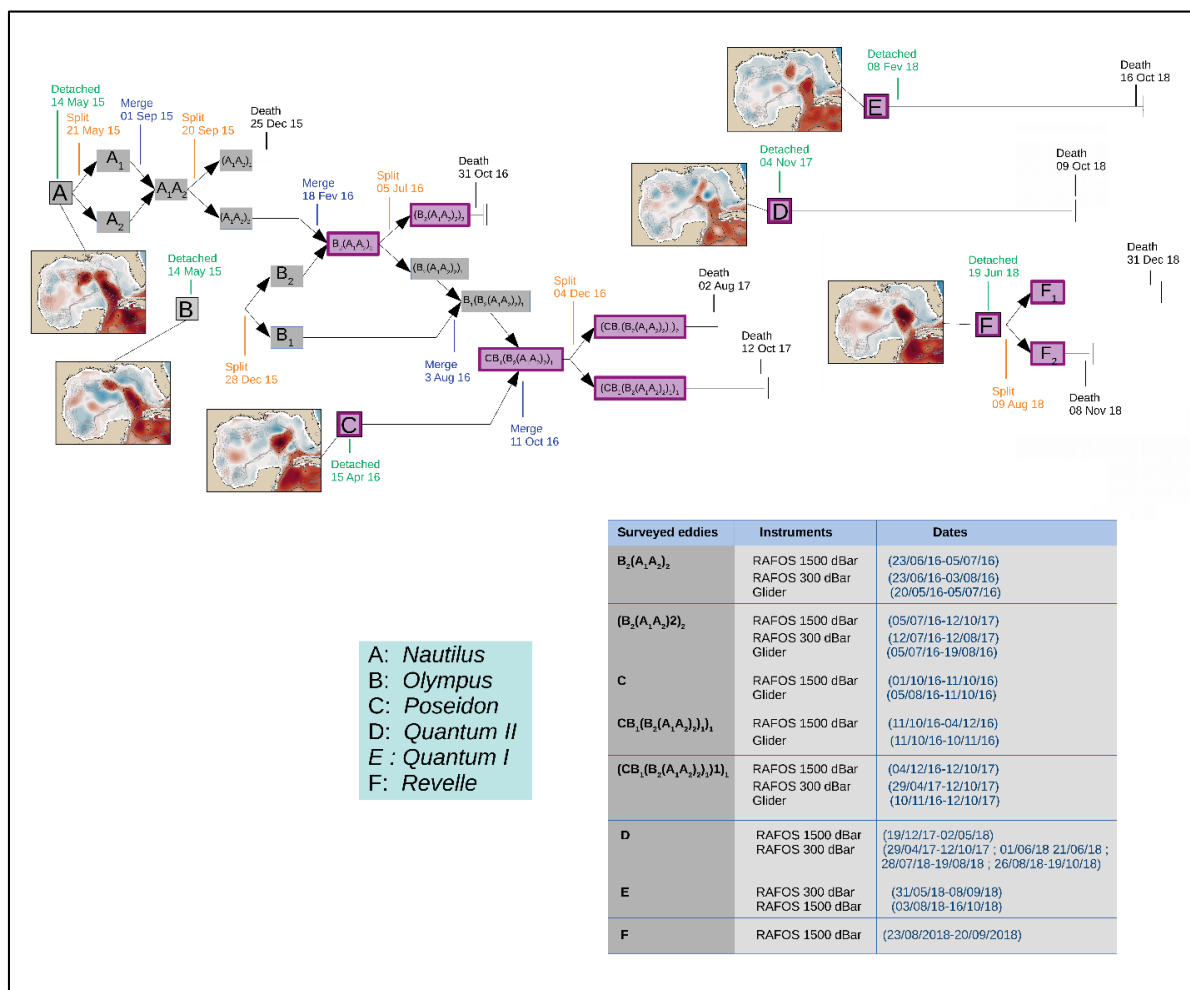


Figure 3-23. Diagram of the life cycles and interactions of the six LCRs surveyed during the DWDE project. The diagram indicates the detachment dates as well as all splitting and merging events, and proposes a nomenclature for the resulting new eddies. The SSH map at the eddies' detachment date is also shown. The dates at which the RAFOS floats sampled each LCR are indicated in the table.

LCR A (Nautilus) detached from the Loop Current in May 2015, one year before the first DWDE float was launched. After a series of splitting and re-merging events, it merged with LCR B (*Olympus*) in February 2016. The latter had detached from the LC in October 2015 and also had experienced splitting. The product of the merging of LCRs A and B, eddy $B_2(A_1A_2)_2$ was surveyed by 1500-dbar and 300-dbar RAFOS floats between 23 June 2020 and 12 August 2017.

LCR C (Poseidon) detached from the LC on 15 April 2016, and drifted through the GoM until it eventually merged with eddy $B_1(B_2(A_1A_2)_2)_1$ in October 2016. The resulting eddy then split in December 2016. The main LCR as well as all sub-eddies resulting from splitting and merging events were surveyed by RAFOS floats between 01 October 2016 and 12 October 2017.

LCR D (Quantum II) detached from the LC on 04 November 2017 and drifted through the GoM until its demise in October 2018 without suffering any splitting, or interaction with any other LCR. It was surveyed by RAFOS floats soon after detachment and until its death (19 December 2017-19 October 2018).

LCR E (Quantum I) detached on 08 February 2018 and also drifted through the GoM without splitting or interacting with previously detached eddies. It was surveyed by the RAFOS floats from 31 May 2018 until its death (09 October 2018).

LCR F (Revelle) detached on 19 June 2018 and split into two sub-eddies on 09 August 2018. The original LCR as well as the secondary eddies were sampled by the RAFOS floats between 23 August 2018 and 20 September 2018.

The LCR's edge contours are chosen to be the maximum circulation contour. This corresponds to the SSH contour where the Okubo Weiss parameter changes sign. This criterion thus allows the enclosure of the coherent part of the eddies (negative OW) only. The edge contours and the center's trajectories of the six LCRs from detachment to death are shown in Figures 3-24, 3-26, 3-28, 3-30, 3-32, 3-34.

Time series of edge contour SSH, total area, circulation, revolution period, mean radius, rotation rate, volume anomaly, average vorticity, and mean edge velocity, were computed for each of the six LCRs, and are shown in Figures 3-25, 3-27, 3-29, 3-31, 3-33, 3-35. The definition of the variables is provided in table 3-8.

The SSH at the eddy's edge contour varies both with time and from one LCR to another. It ranges between 0.1 and 0.4 m, and exhibits a general decreasing trend with time for nearly all eddies. These results suggest that defining the edge of a LCR using a chosen fixed SSH contour might overestimate the eddy's size soon after detachment, and underestimate their lifetime once the edge contour decreases below the threshold value of the chosen fixed contour.

While the areas of the eddies show strong variability and, in general, no obvious trend, the circulation of all eddies tends to decay regularly with time. Relative vorticity also decreases with time. It ranges between 0.3 times the Coriolis frequency for young LCRs and 0.1 for old eddies. LCRs thus have a rather high dynamical Rossby number. The rotation rates also show a general decrease with time, but exhibit more variability than vorticity. Therefore, the revolution period is naturally more variable, and tends to increase with time. The volume anomaly, which was shown to be proportional to the total heat content anomaly of the eddies (Meunier, 2020), also shows a decaying tendency.

The wide range of each of these variables, and the fact that the RAFOS floats sampled a large number of LCRs at different stages of their life cycle, suggests that a detailed analysis of the DWDE data should provide new information on LCR dynamics in a variety of situations.

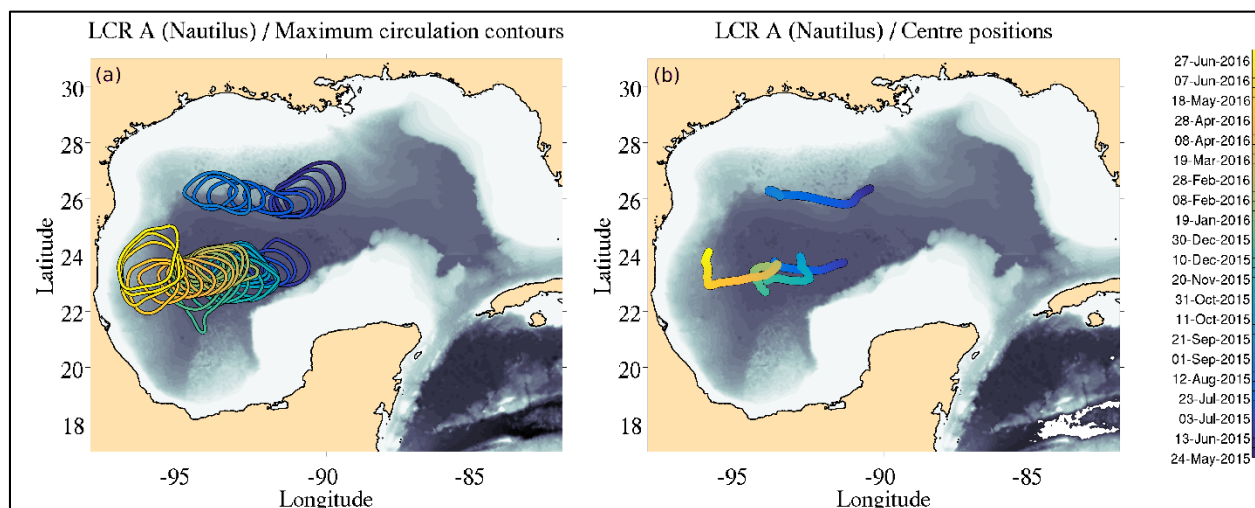


Figure 3-24. Time evolution of Eddy Nautilus and its ‘children’ eddies. (a) Outer boundary of the LCR as defined by maximum circulation contour, and (b) pathway of the LCR defined by the center position of the area defined by the maximum circulation contour at each time step.

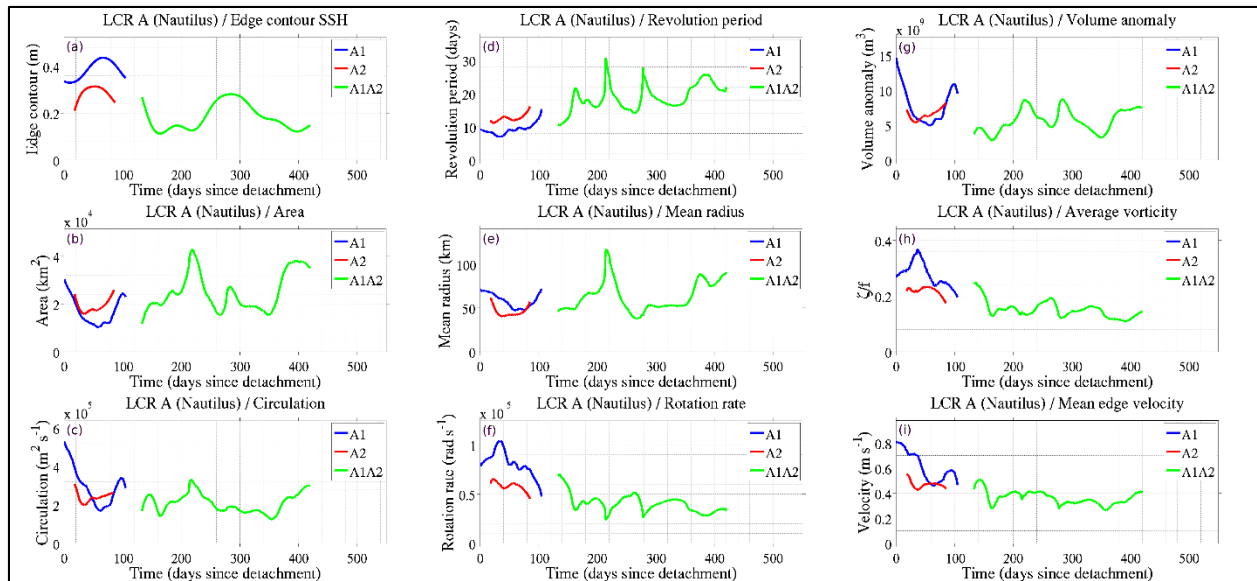


Figure 3-25. Time evolution of LCR A's properties, computed from Aviso ADT product. The blue and red lines represent the eddies A1 and A2, respectively, while the green lines represent eddy A1A2, which arose from the merger of the two smaller eddies. The eddy's edge is defined as the maximum circulation contour. a: SSH at the eddy's edge. b: Total area. c: Total circulation. d: Revolution period, defined as the time necessary for a virtual particle to circle the eddies along their edge contour. e: Mean eddy radius (defined as the average distance between the edge contour and its centroid). f: Rotation rate at the edge contour location. g: Total volume anomaly defined as the surface integral of SSH anomaly over the eddy. h: Mean vorticity (normalized by the Coriolis frequency at the eddy's center). i: Mean velocity along the edge contour.

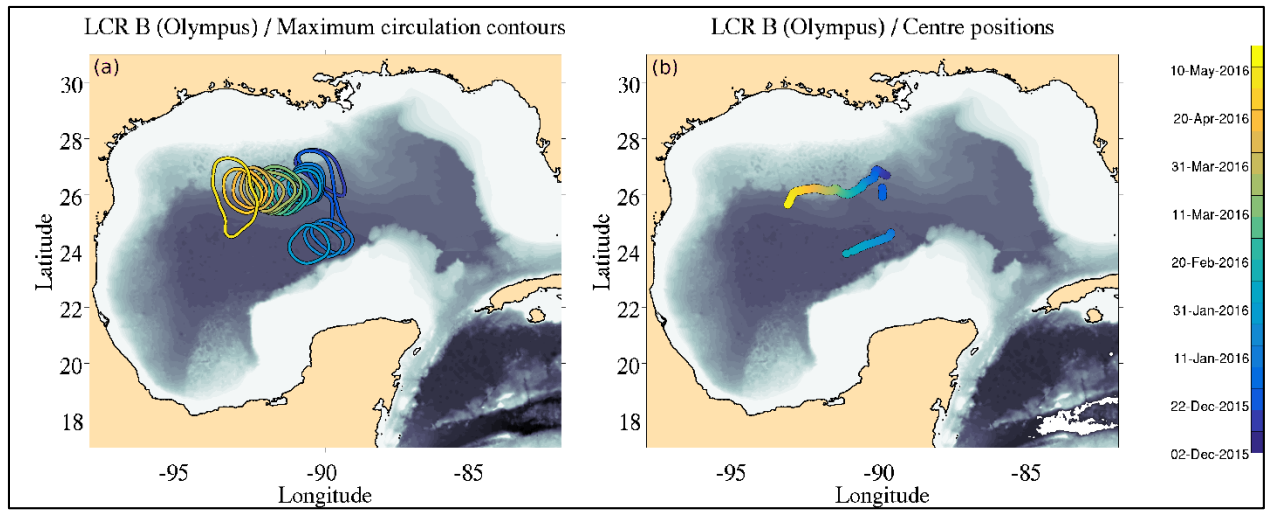


Figure 3-26. Same as Figure 3-24 for LCR B.

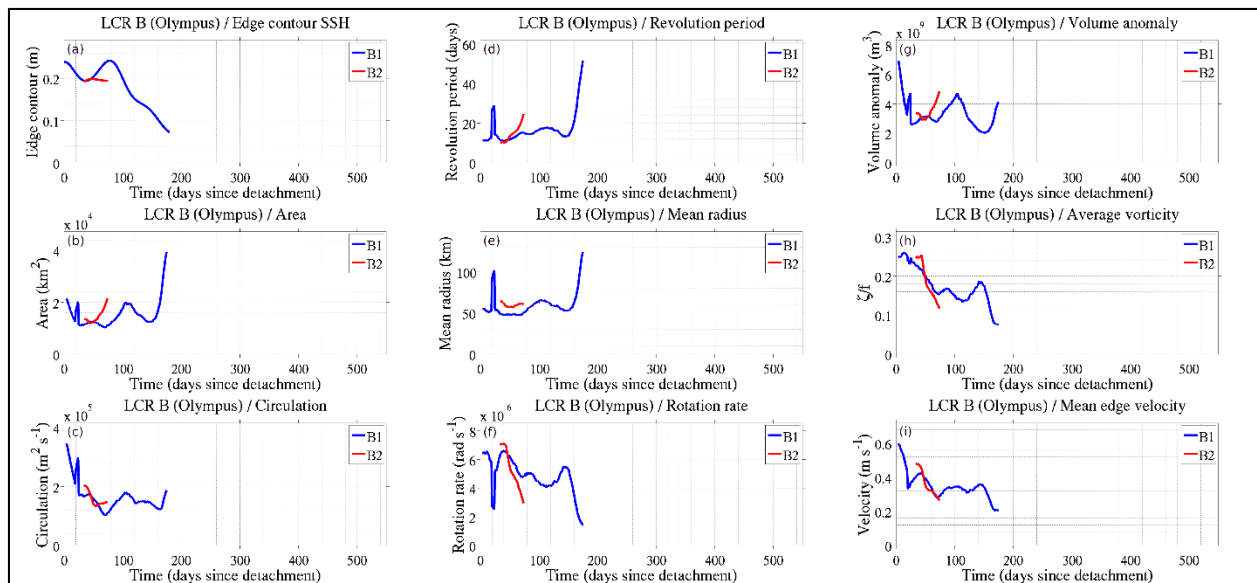


Figure 3-27. Same as Figure 3-25 for LCR B.

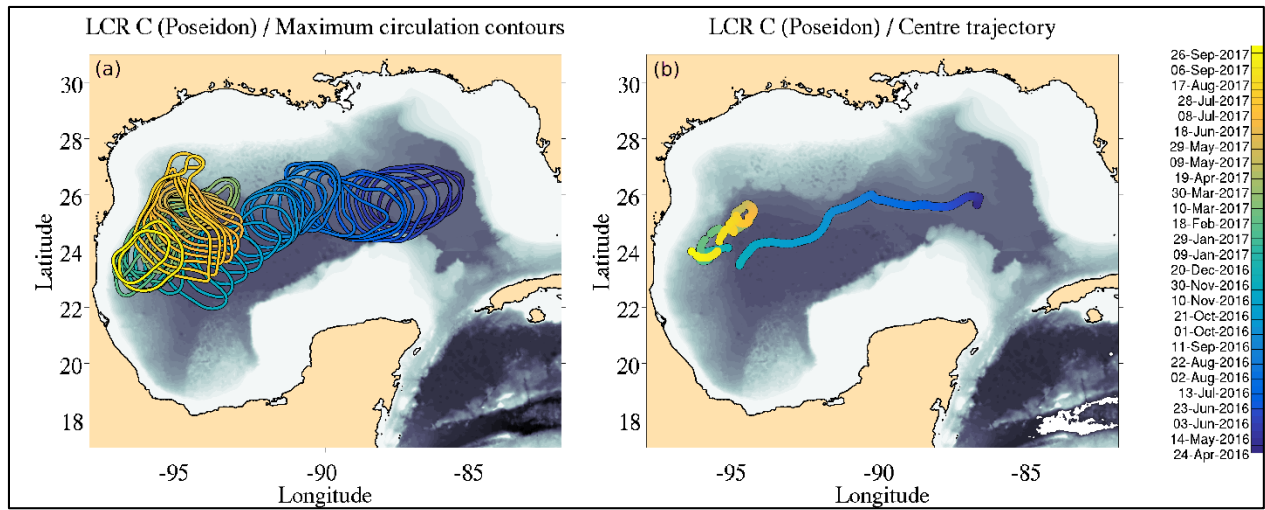


Figure 3-28. Same as Figure 3-24 for LCR C.

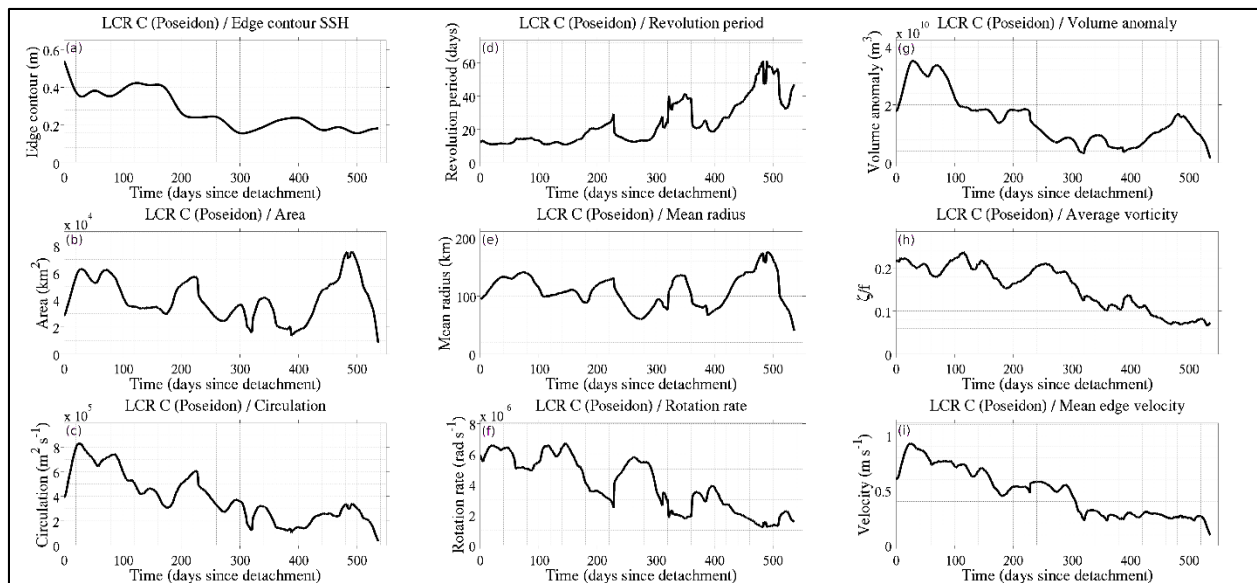


Figure 3-29. Same as Figure 3-25 for LCR C.

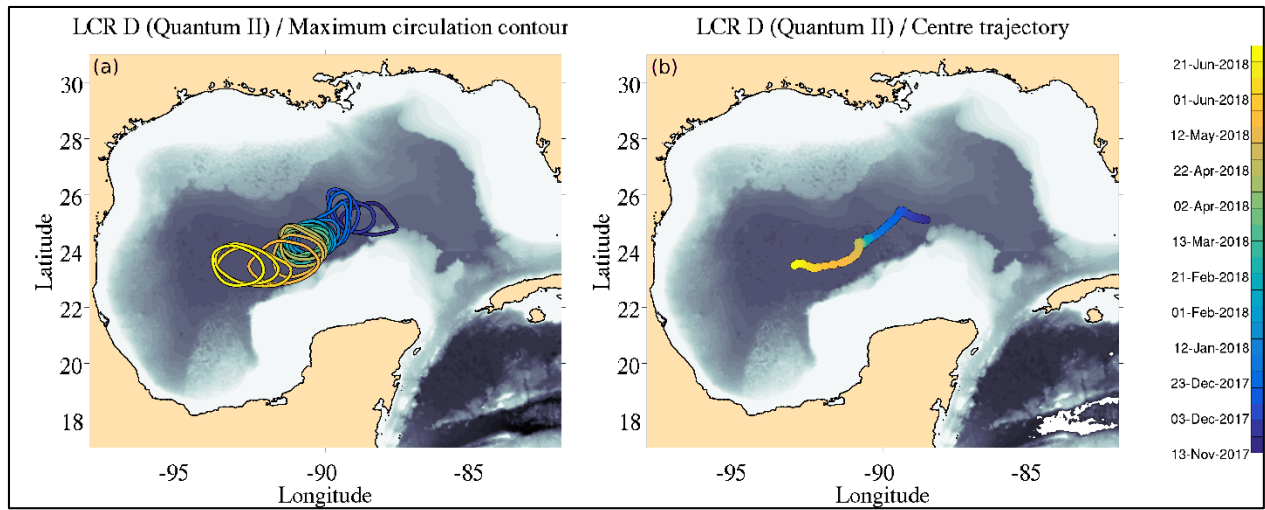


Figure 3-30. Same as Figure 3-24 for LCR D.

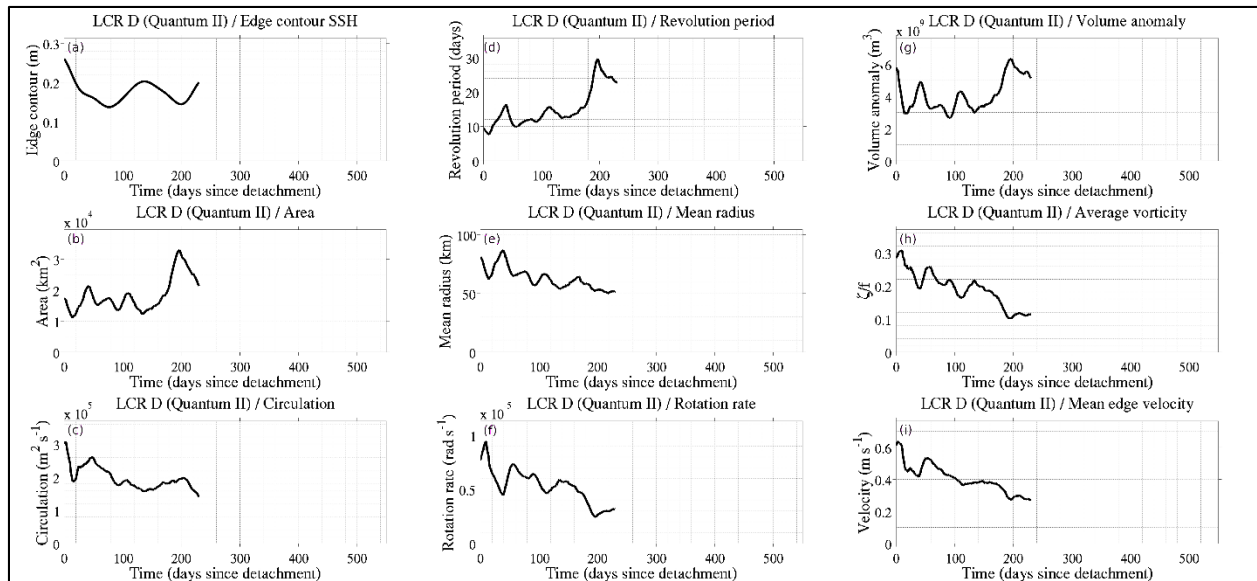


Figure 3-31. Same as Figure 3-25 for LCR D.

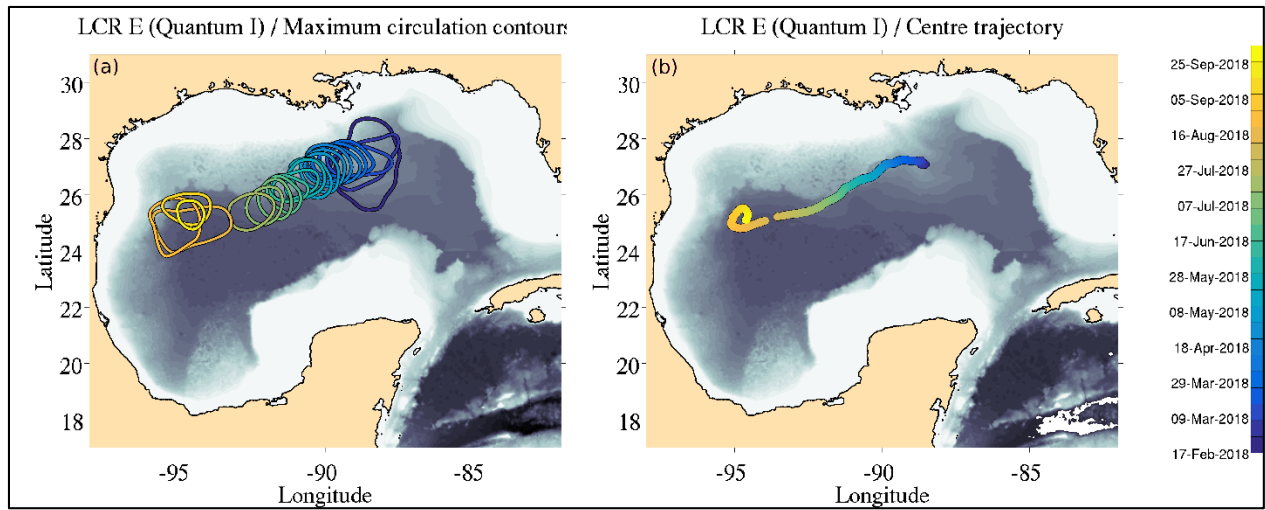


Figure 3-32. Same as Figure 3-24 for LCR E.

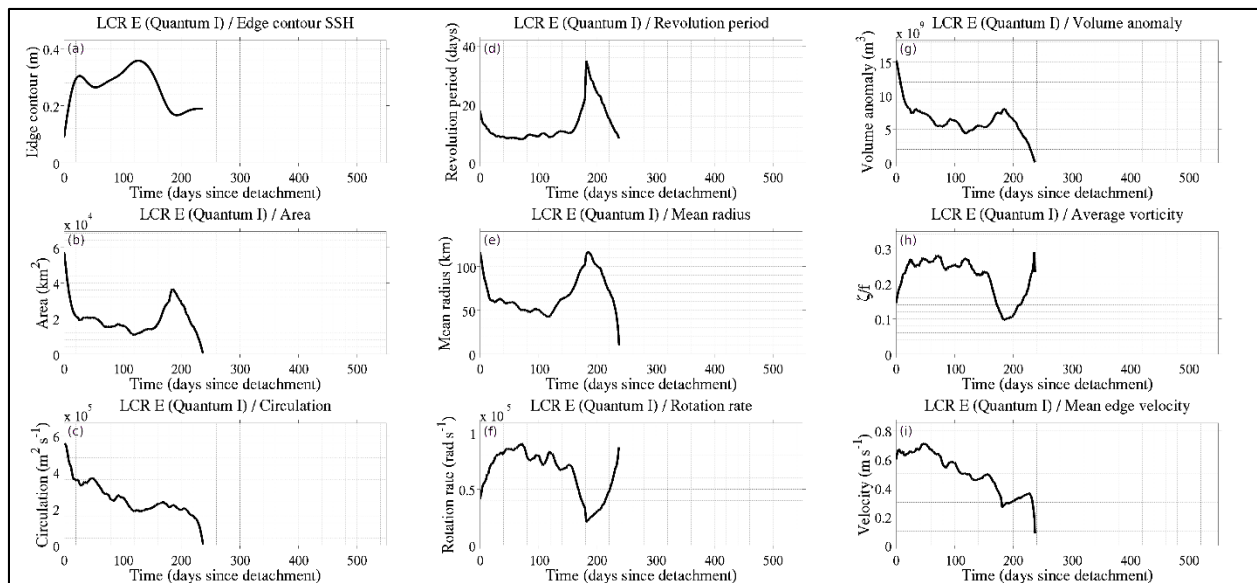


Figure 3-33. Same as Figure 3-25 for LCR E.

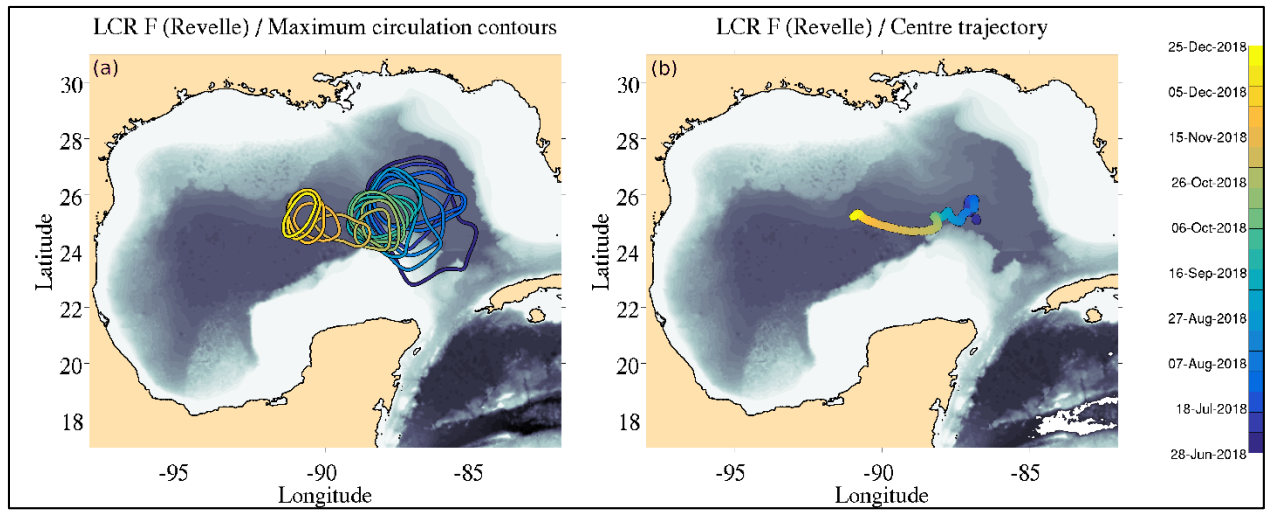


Figure 3-34. Same as Figure 3-24 for LCR F.

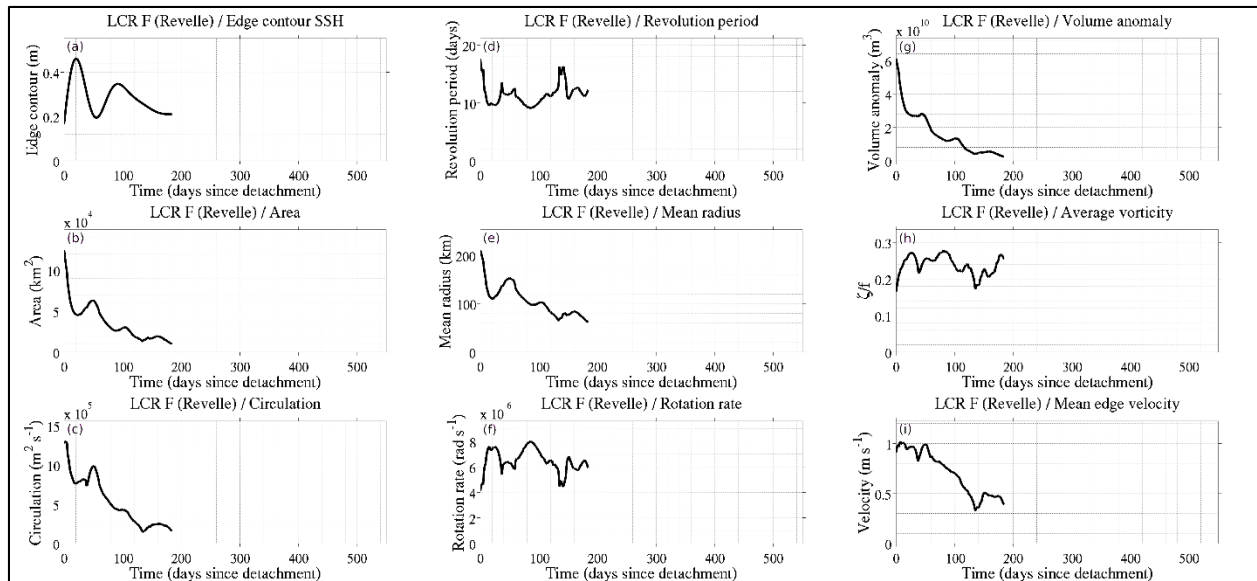


Figure 3-35. Same as Figure 3-25 for LCR F.

Variable	Abbreviation and units	Definition
SSH anomaly	η [m]	$\eta = \text{ADT-mode}(\text{ADT})$
Area	\mathcal{A} [m^2]	$\mathcal{A} = \iint_S dS$
Circumference	L [m]	$L = \oint_{\mathcal{L}} dl$
Centre	$[x_c, y_c]$ [m]	$[x_c, y_c] = \frac{1}{L} \oint_{\mathcal{L}} [x(l), y(l)] dl$
Radius	R [m]	$R = \frac{1}{L} \oint_{\mathcal{L}} \sqrt{(x(l) - x_c)^2 + (y(l) - y_c)^2} dl$
Volume	V [m^3]	$V = \iint_S \eta dS$
Circulation	C [$m^2 s^{-1}$]	$C = \oint_{\mathcal{L}} \vec{u} \bullet \vec{dl}$
Mean vorticity	$\bar{\zeta}$ [s^{-1}]	$\bar{\zeta} = \frac{C}{\mathcal{A}}$
Revolution period	τ [s]	$\tau = \oint_{\mathcal{L}} \frac{dl}{u}$
Rotation rate	Ω [s^{-1}]	$\Omega = \frac{2\pi}{\tau}$

Table 3-8. List of the variables' definitions and abbreviations used in section 3.4.

3.10 PSEUDO EULERIAN STATISTICS AND DOMINANT CIRCULATION PATTERNS

This program adds to the knowledge of deep Gulf circulation in the western Gulf from observation, specifically Lagrangian observations as seen in Hamilton et al. (2017) and Pérez-Brunius et al. (2018). The deep circulation in the Gulf has been studied using models, e.g. Oey (2008), but only a few observations in the deep Gulf have been made, limiting our understanding of deep flow variability and mean. Morey et al. 2020 used deep Lagrangian observations, specifically gridded fields derived from RAFOS float observations at 1500 dbar, to validate different ocean model deep circulations. The data collected as part of this experiment adds to the repository of 1500-dbar data, especially in the under-sampled western Gulf, and also provides novel 300-dbar data from which upper layer circulation can be better understood.

Similar to the methods used in Pérez-Brunius et al. (2018), the Lagrangian observations were gridded to provide quasi-mean statistics of the Eulerian velocity field. Provided below are the mean gridded velocity vectors, variance ellipses, eddy kinetic energy (EKE), mean kinetic energy (MKE), and ratio of mean kinetic energy to total kinetic energy. The Gulf circulation is not a stable regime, with the Loop Current extending into the Gulf and periodically pinching off a LCR once every ~ 8 -14 months. Other eddies spun up around the Loop Current as well. We caution that the resultant gridded fields from the DWDE Lagrangian data

need to be understood in the context of transitory events, specifically large eddies that were present at the time of the deployments and duration of the project. This caution is especially relevant to the upper layer (300 dbar) gridded fields.

What stands out from the pseudo-Eulerian fields from the DWDE dataset at 300 dbar are a strong anticyclonic circulation in the northwest Gulf, which is dominated by the eddies present in the region at the time, and the cyclonic Campeche Gyre (Pérez-Brunius et al., 2013). In the deep western Gulf, the cyclonic SAG is present in the mean, as was first discovered by Pérez-Brunius et al. (2018). Additionally, a weak western boundary current exists, which is consistent with results from the previous deep RAFOS program (Pérez-Brunius et al., 2018). The presence of the deep features in both the 2011-2015 and the 2016-2019 float data sets gives weight to the persistence of these features.

METHODOLOGY

The dominant circulation patterns of the region were evaluated by calculating bin statistics on each of the two groups of data (300 dbar and 1500 dbar). Since the Gulf is well-represented as a two-layer system, the upper layer spanning from the surface to 800-1000 m and the lower layer spanning from 1200 m to the seafloor (e.g., Hamilton, 2009), we expect the floats at the two depth levels to exhibit different circulation patterns. Therefore, the two layers were processed identically but separately, using the methodology described in Hamilton et al. (2017) and Pérez-Brunius et al. (2018).

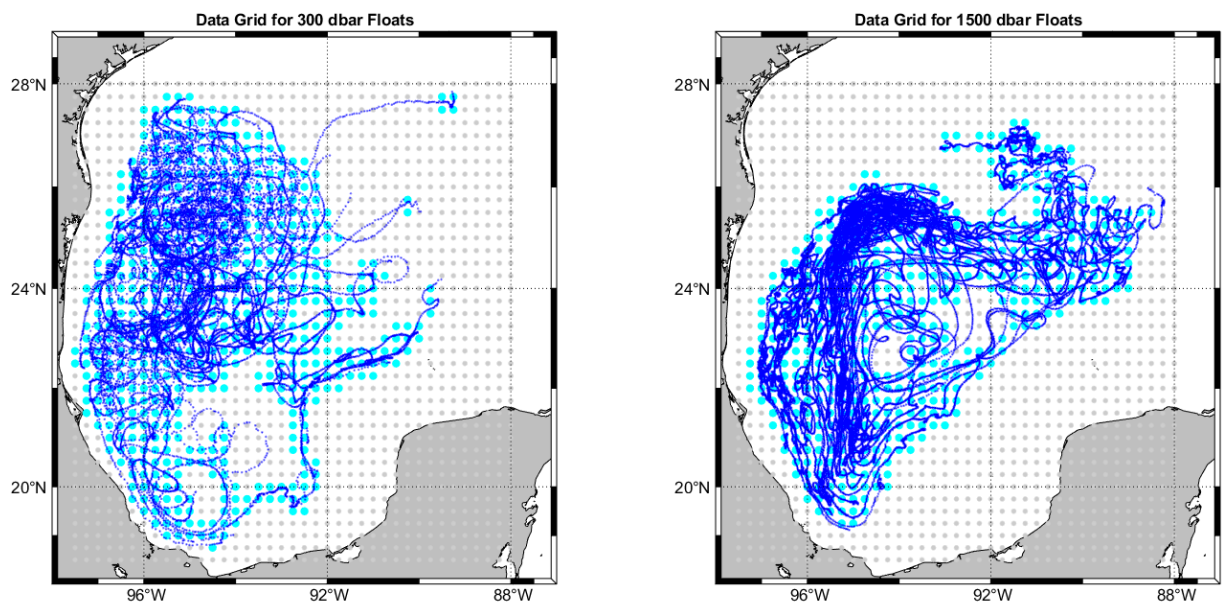


Figure 3-36. Entire data grid for study area (gray dots), grid boxes containing float data with five degrees of freedom or greater (defined below; cyan dots), float trajectories (blue dotted lines) for 300-dbar (left panel) and 1500-dbar (right panel).

The first step was to divide the study area (97.5 - 88 W, 18.5 - 28 N) into gridded fields of 0.5° x 0.5° overlapping boxes (for smoothing of results), centered on 0.25° x 0.25° grid (gray dots in Figure 3.5.1). The result was a 39 x 39 matrix, with 1,521 grid boxes.

Working with the 300-dbar and 1500-dbar float data separately, all data were assigned to a grid box. The *Number of Observations* is the sum of data points in each grid box. Figure 3-37 shows the *Number of Observations* field after the *Degrees of Freedom* criteria have been applied (see below). The *Number of Observations* for the 300-dbar data ranged from 19 to 465, with the highest observation near the Perdido Escarpment. The *Number of Observations* for the 1500-dbar floats ranged between 48 to 2,023 with the highest concentration on the slope below the Perdido Escarpment.

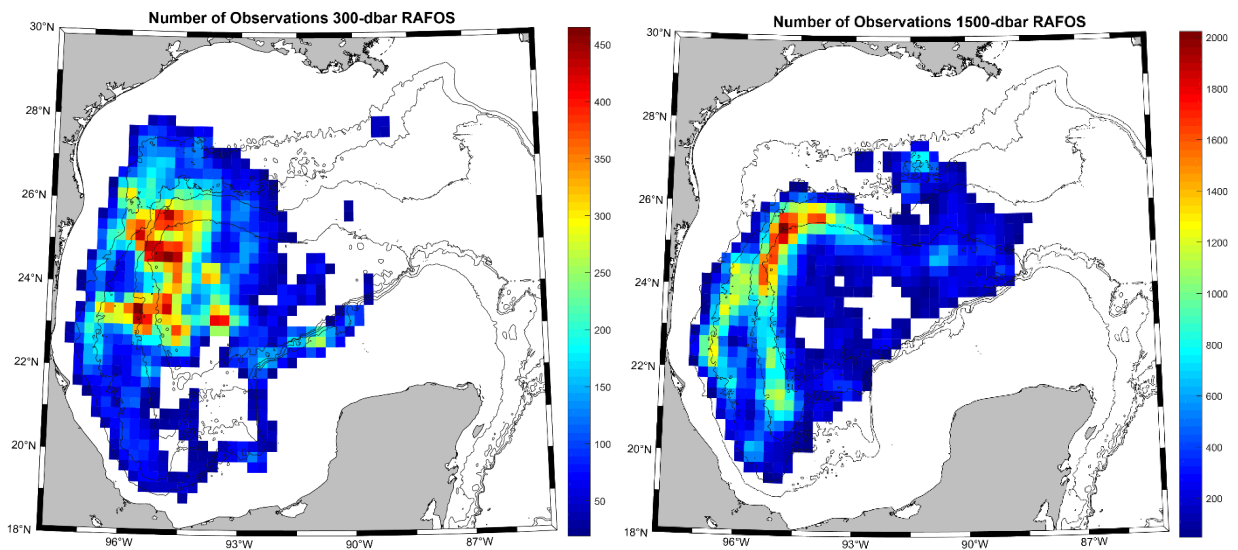


Figure 3-37. *Number of Observations per grid box for 300-dbar floats (left) and 1500-dbar floats (right). Grid boxes that fell below 5 degrees-of-freedom were eliminated prior to plotting. The 1000-, 2000-, 3000-, and 3500-m isobaths are drawn. Note the color scales are not the same.*

Once the data were assigned to a spatial grid box, the data within each box were binned into 24-hour intervals. The number of observations within each of these temporal bins was tallied. The number of unique days (N) that contained data was divided by an integral time scale (T) to calculate the *Degrees of Freedom*. (Integral time scale calculations may be found in Section 3.3 of this report.) Only bins with greater than five Degrees of Freedom are used in the analysis.

$$\text{Degrees of Freedom} = N/T$$

N = number of unique days that contained data

T = 2.4 days for 300-dbar floats

T = 4.9 days for 1500-dbar floats

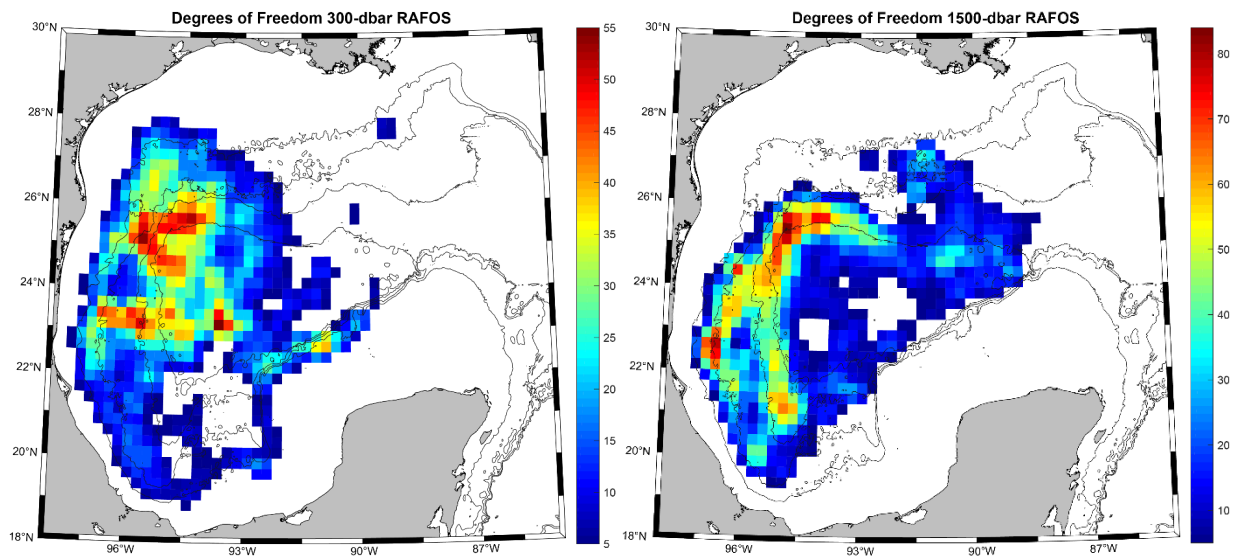


Figure 3-38. Degrees of Freedom for 300-dbar floats (left) and 1500-dbar floats (right). Bins with less than 5 Degrees of Freedom are not plotted. The 1000-, 2000-, 3000-, and 3500-m isobaths are drawn. Note the color scales are not the same.

An estimated number of *Degrees of Freedom* may be used for estimating the standard error of a dataset that is finite and does not consist entirely of independent measurements. The maximum *Degrees of Freedom* value for the 300-dbar data is 55, and 84 for the 1500-dbar data, (Figure 3-38). Confidence intervals are then used to test the reliability of the *Degrees of Freedom* calculated: the 95% confidence interval, for example, is the range of values for which it is 95% certain the values are the true mean of the data. The resulting data were used for analysis.

MEAN VELOCITY VECTORS

Mean velocity vectors of the gridded data for both the 300-dbar floats and the 1500-dbar floats are presented in Figure 3-39. The means were calculated using the velocity values within a gridded bin, and placed at the center of the bin. The data presented are either black arrows, indicating that the means are larger than the 95% confidence intervals, or red arrows, indicating the means are smaller than the 95% confidence interval, and therefore not significantly different from zero.

There are two easily discernible, statistically significant, cyclonic eddies visible in the 300-dbar float data. The first is the well-known cyclonic Campeche Gyre located in the Bay of Campeche ($\sim 10\text{-}40\text{ cm s}^{-1}$ velocity; Pérez-Brunius et al. 2013). The second is located near the Perdido Escarpment in the northwest corner of the Gulf of Mexico between the 1000- and 2000-m isobaths ($\sim 10\text{-}30\text{ cm s}^{-1}$ velocity). A weaker and elongated anti-cyclonic eddy, with velocities ranging from 5 to 20 cm s^{-1} , is apparent just south of the Perdido Escarpment. We suspect that the cyclone and anticyclone in the northwestern Gulf are transitory

remnants of a LCR which is anticyclonic, and cyclones spun up by the LCR. Several 300-dbar floats were trapped in these features. For example, float 1496 was trapped in the cyclonic feature for about 240 days (see Figure 3-16 in section 3.2 Eddy Census).

The pseudo-Eulerian mean velocities from the 1500-dbar float data are much weaker than those from the 300-dbar floats. There are two dominant, statistically significant circulation features of the deep flow field: first is a weak ($<5 \text{ cm s}^{-1}$) cyclonic boundary current along the 2000-m isobath in the western Gulf and around the Bay of Campeche. The second is the cyclonic SAG above the Sigsbee Abyssal Plain, which is constrained by a closed contour of planetary potential vorticity (f/H). The velocity in the cyclonic eddy is $\sim 8\text{-}10 \text{ cm s}^{-1}$. Both of these features were found in the similarly-derived gridded velocity fields during the observational period 2011-2015 (Pérez-Brunius et al., 2018).

One contrast in the deep flow field between the earlier study and this study is the flow just south of the Sigsbee Escarpment ($25^\circ\text{N } 92^\circ\text{W}$). In the earlier study, this statistically significant flow was from east to west, whereas in this time period, the flow was from west to east. In both cases, velocity magnitudes were about $5\text{-}10 \text{ cm s}^{-1}$.

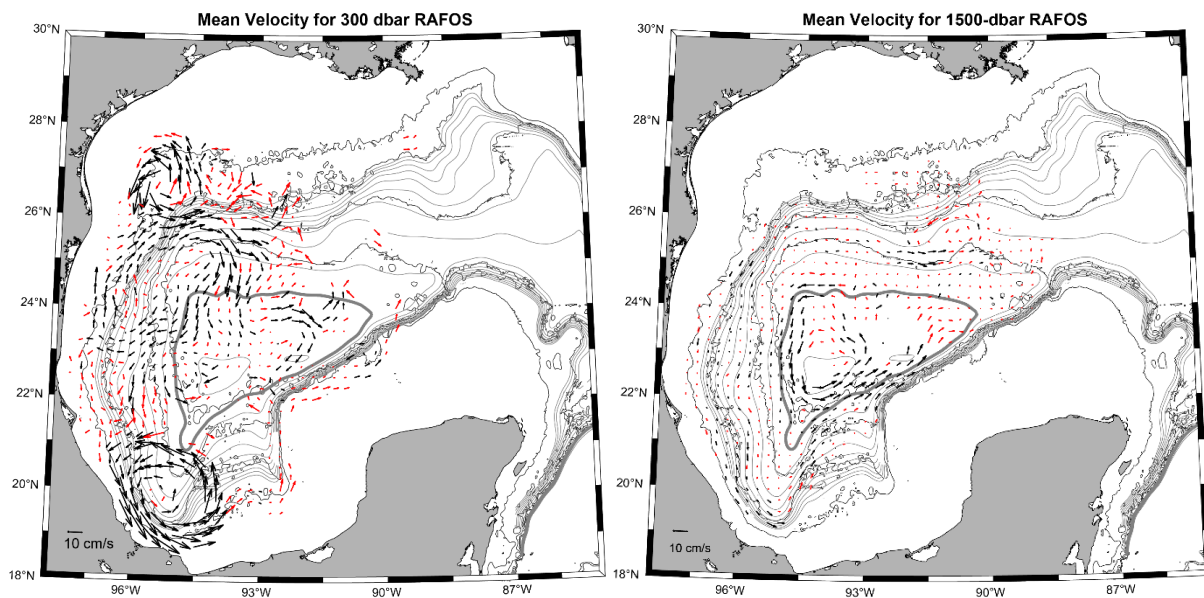


Figure 3-39. Mean velocity vectors for 300-dbar floats (left) and 1500-dbar floats (right). Black (red) arrows indicate that the float bin averages are (are not) significantly different from zero at the 95% confidence level. Planetary potential vorticity (f/H) contours are drawn in gray, where f is the local Coriolis parameter and H is the bottom depth. Closed f/H contour $1.61 \times 10^{-8} \text{ m}^{-1} \text{ s}^{-1}$ is shown with a thick gray line. Black contours show the 1000-, 2000-, 3000-, and 3500-m isobaths.

VARIANCE ELLIPSES

Variance ellipses of speed were calculated and are presented in Figure 3-40. Variance ellipses are an indication of anisotropy (degree of directionality) of the flow (Lilly, 2019). In general, the flow at 300 dbar is more isotropic, indicating that the direction of the flow frequently changes angle of direction. This is expected in a region such as the northwest Gulf, where upper layer flow is generally detached from the lower layer and comprises a variable field of westward drifting eddies. In the Campeche Gyre, located over the Bay of Campeche to the south, however, the flow does become more anisotropic, with ellipses' major axes oriented along the geographic slope.

The velocity field at 1500 dbar is generally anisotropic, with strongest anisotropy along the boundary current where the cyclonic flow follows the bathymetric slope. The exception to this is in the central Gulf where direction of the flow is sometimes perpendicular to the planetary potential vorticity contours, but this occurs in a region where results are not generally statistically significant.

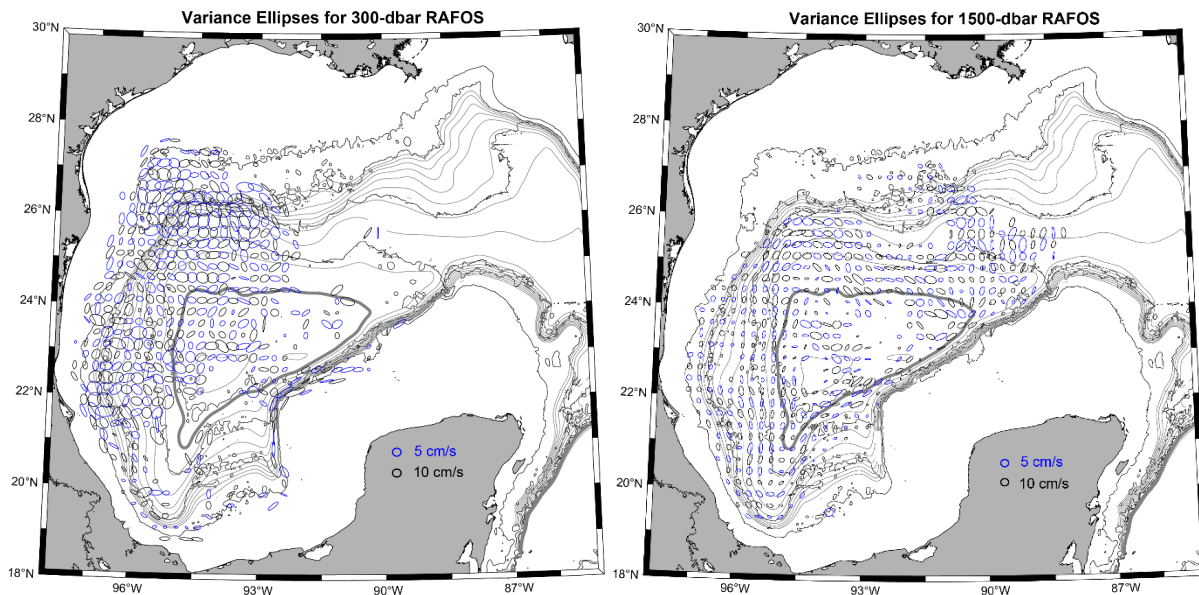


Figure 3-40. Variance ellipses for 300-dbar floats (left) and 1500-dbar floats (right). The blue ellipses represent mean values $< 10 \text{ cm s}^{-1}$; the black ellipses are mean values $\geq 10 \text{ cm s}^{-1}$. Planetary potential vorticity (f/H) contours are drawn in gray, where f is the local Coriolis parameter and H is the bottom depth. Closed f/H contour $1.61 \times 10^{-8} \text{ m}^{-1} \text{ s}^{-1}$ is shown with a thick gray line. Black contours show the 1000-, 2000-, 3000-, and 3500-m isobaths.

TOPOGRAPHY ANISOTROPY

In order to assess the impact of topography on the currents in the western Gulf, a statistical analysis of topographic anisotropy was performed on the RAFOS and surface drifter datasets. We used the bathymetric 1-minute gridded dataset ETOPO1 (<https://www.ngdc.noaa.gov/mgg/global/>) and ran a 2-D Gaussian low-pass filter with a decorrelation radius of 50 km to smooth the bathymetry and coast line. Along and cross-shore velocity components were computed by projecting the velocity vectors on the 1000-m isobath contour. We assess topographic anisotropy through two simple variables: the angle θ between the velocity vector and the 1000-m isobath, and the ratio of along to cross-shore velocity. Polar distributions of θ are shown in Figures 3-41a, b, and c for the surface drifters, the 300- and the 1500-dbar RAFOS floats, respectively. Distribution of the velocity ratio is shown in Figures 3-41d, e, and f.

The effects of topography on the surface velocity appear to be moderate, with a mode of the velocity ratio at 1.11, corresponding to an increase of about 10% of alongshore velocity compared to cross-shore velocity. The moderate anisotropy is also visible in the polar diagram, as an elliptical distribution with a great axis directed towards $\theta = 0$. At 300 dbar, evidence for anisotropy is less clear and the polar distribution exhibits more noise because of a smaller sample size. The mode of the velocity ratio is however still above unity (1.08). At 1500 dbar, both the polar diagram and the velocity distribution show a clear anisotropy. The polar distribution is elliptical with a great axis directed towards $\theta = 0$, and the velocity ratio has a mode of 1.41, meaning that along shore currents are approximately 40% faster than cross-shore currents. These results suggest that the flow at 1500 dbar is strongly affected by the topography.

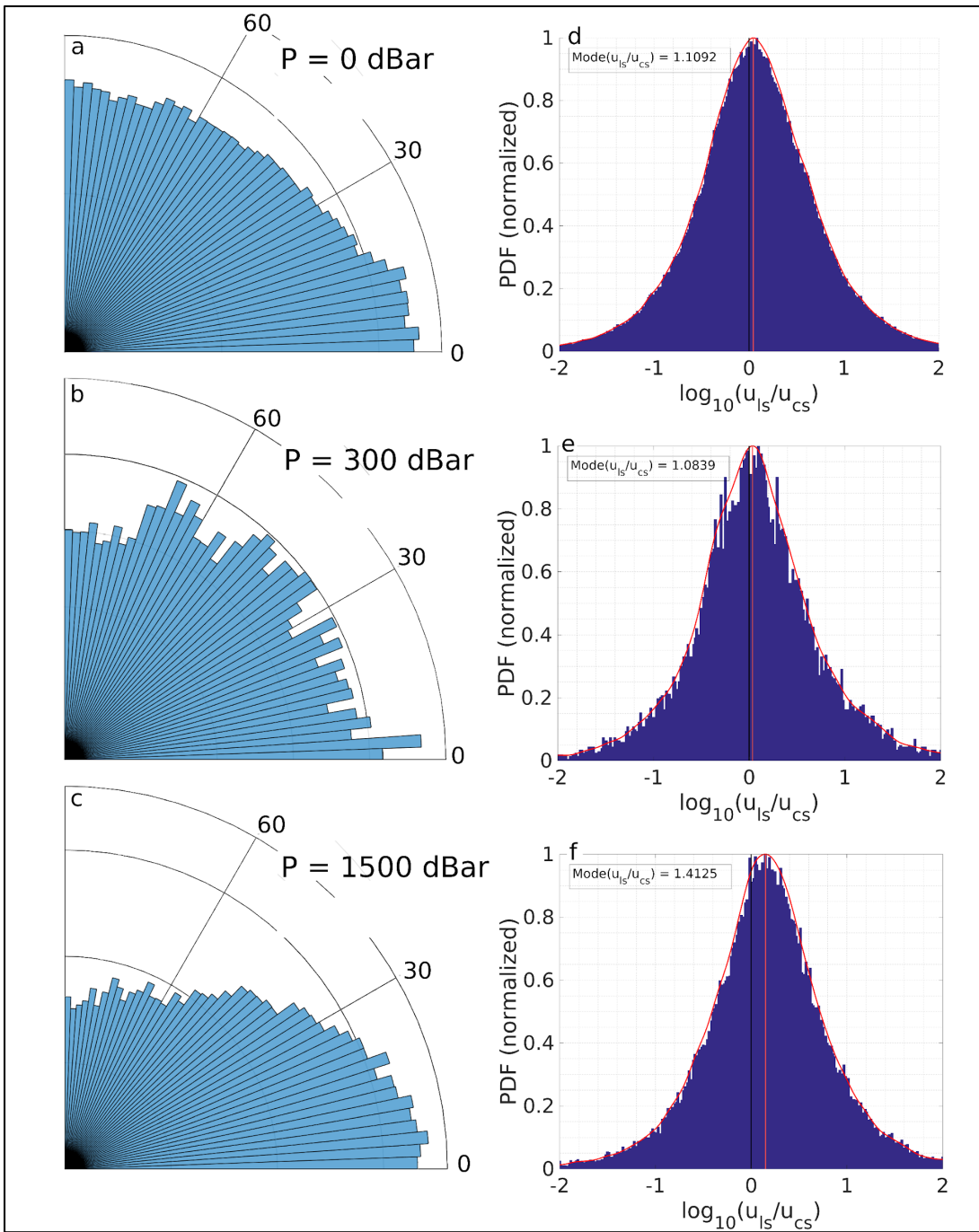


Figure 3-41. *a, b, and c:* polar distribution of the angle between the velocity vectors and the 1000 m isobath for the surface drifters, 300-, and 1500-dbar RAFOS floats, respectively. *d, e, and f:* Histogram of the ratio of the along-shore and cross-shore components of the velocity vectors for the surface drifters, 300-dbar, and 1500-dbar RAFOS floats, respectively.

MEAN KINETIC ENERGY

Mean kinetic energy density (hereafter, just ‘Mean Kinetic Energy’ (MKE)) is proportional to mean flow calculated over a specified time interval. The MKE, defined below, is used to identify the strength and location of stable circulation features.

$$K_M(x, y) = 0.5(\bar{u}^2 + \bar{v}^2)$$

\bar{u} = mean zonal velocity in each grid box

\bar{v} = mean meridional velocity in each grid box

Overall, the MKE values for 300-dbar floats were 3-4 times higher than for the 1500-dbar floats (Table 3-9) and had a much larger range. This is expected, as the velocities at 300 dbar are higher, and can be seen in the difference in magnitude (a factor of about 2) between the upper and lower gridded velocity fields. The mapped MKE field (Figure 3-42) shows ‘hot spots’ in the Bay of Campeche, which has the highest MKE, and on the slope northwest of Perdido Escarpment between 500-1000 meters. The high MKE region in the Bay of Campeche is related to the relatively stationary Campeche Gyre, and forms a nearly closed bolus of high MKE of a few hundred kilometers diameter. The high MKE patch in the northwest Gulf in the upper layer is related to the persistent eddies found in the northwest corner of the Gulf during this study period. We suspect that the eddies that travel into this region, whose leading wall reaches water shallower than 1000 m depth, may begin to become ‘stuck,’ and remain in this location for a length of time before fading or disintegrating. The example float 1496 in Figure 3-16 in section 3.2 was trapped in this location for about half the time the float was trapped in the eddy, so ~120 days. This persistence in location would explain the patch of high MKE in this location during this time period.

The deep MKE field shows a single dominant region of higher MKE, tracing out the SAG, similar to what was found in Pérez-Brunius et al. (2018). There is a small elongated patch of weak MKE residing on the east side of the Bay of Campeche in the deep layer that was also seen in the earlier time period (Pérez-Brunius et al., 2018) which indicates persistent weak flow in this location.

	Minimum	Maximum	Mean	Median	Mode
MKE (cm² s⁻²)					
300 dbar	0.0	321.3	31.6	13.1	0.0
1500 dbar	0.00	67.9	5.1	1.4	1.4
EKE (cm² s⁻²)					
300 dbar	5.6	550.2	112.1	86.4	10.2
1500 dbar	2.2	83.8	19.8	16.5	8.1
MKE/(MKE+EKE) (cm² s⁻²)					
300 dbar	0.0	90.9	19.3	13.6	0.3
1500 dbar	0.0	82.8	15.4	8.2	15.0

Table 3-9. Basic statistics for MKE, EKE, MKE/(MKE+EKE) of 300-dbar and 1500-dbar floats.

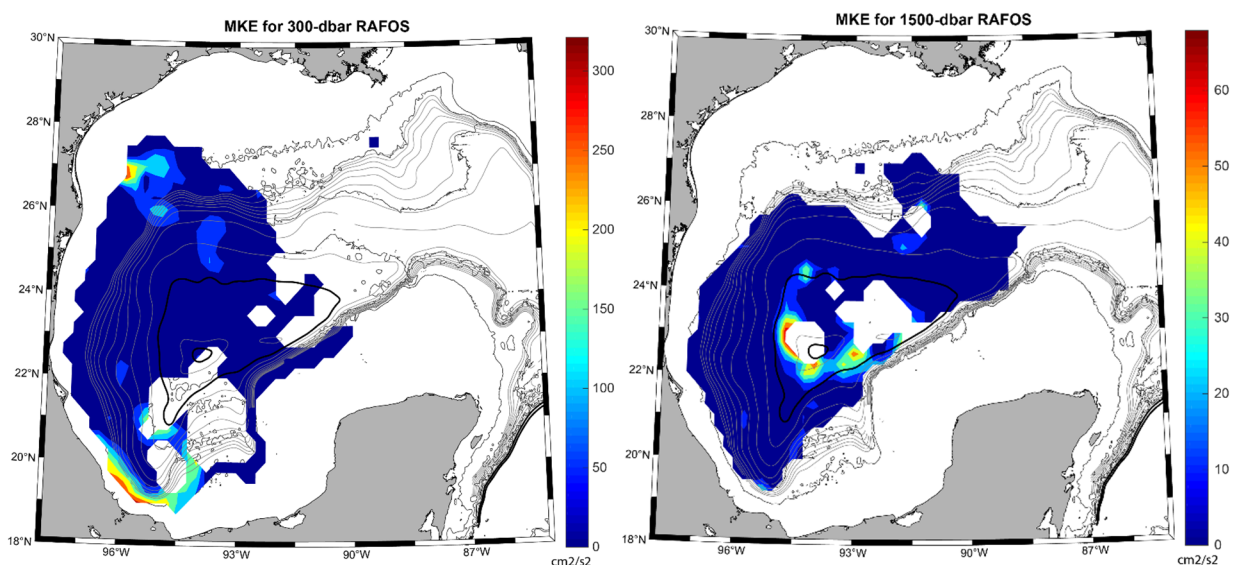


Figure 3-42. Mean kinetic energy for 300-dbar floats (left) and 1500-dbar floats (right). Bathymetry and planetary potential vorticity (f/H) drawn as in Figure 3-40. Note color scales are not the same.

EDDY KINETIC ENERGY

Eddy Kinetic Energy (EKE) is the time-varying component of the total energy of the flow, or the deviation from the mean. EKE measures the strength of the variability of the flow. The EKE of the study region was higher in magnitude than the MKE in both shallow and deep water.

$$K_E(x, y) = 0.5 \overline{(u'^2 + v'^2)}$$

u' = standard deviation of zonal velocity in each grid box

v' = standard deviation of meridional velocity in each grid box

The highest EKE values for the 300-dbar floats were located in the Perdido Escarpment region, in an east-west oriented patch from about 93-97°W. Two additional areas with moderate EKE are located on the East Mexico Shelf between 1500-2000 meters and just north of the Bay of Campeche. This is evident even with the gap of data in that area. We suspect that these higher EKE regions are due to the vigorous eddy field along the northern wall of the Campeche Gyre, part of the 'eddy graveyard.'

The highest EKE values for the 1500-dbar floats are along the northeast portion of the SAG, and a couple of patches at the eastern edge of the float observation region, in the central Gulf. The high EKE near the SAG was also seen in the previous deep float study (Pérez-Brunius et al. 2018). This EKE signature is related to eddies, particularly anticyclonic eddies, that are spun up at the easternmost location and travel westward along the northern boundary of the SAG. These eddies may make up the northern wall of the SAG. In this study, only two partial formation events were observed (Figure 3-17 in section 3.3 Eddy

Census). There were, however, other trajectories seen in Figure 3-17 which show evidence of being entrained in the anticyclones in this region. The higher EKE patches in the central Gulf (which is the eastern boundary of this data set) make sense in context of the EKE results from Pérez-Brunius et al. (2018), which covered the entire Gulf: these patches are in the western boundary of the high EKE region under the Loop Current.

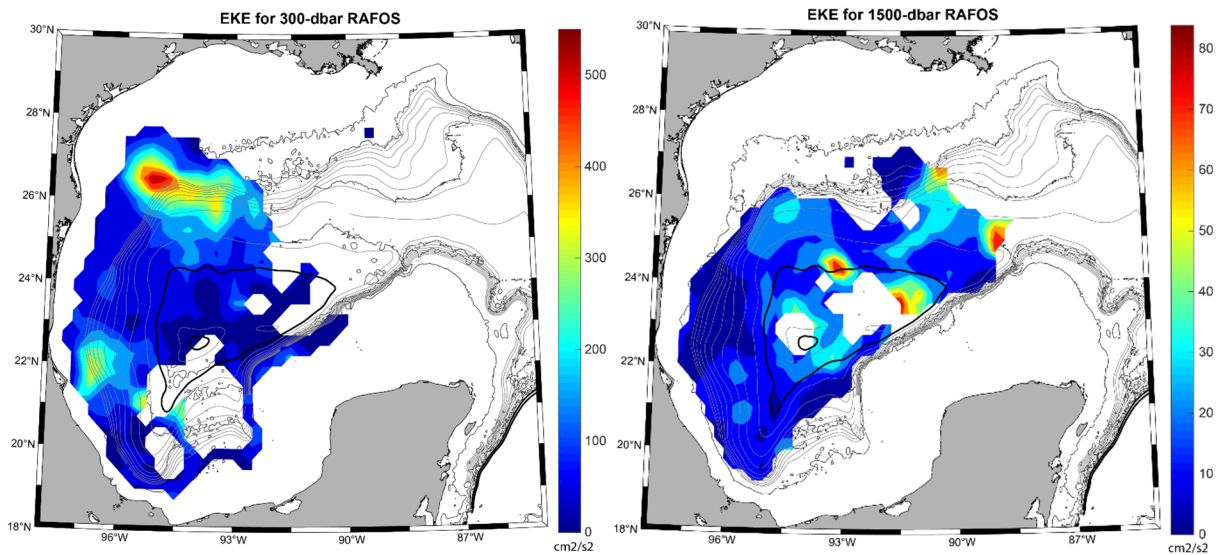


Figure 3-43. Eddy kinetic energy for 300-dbar floats (left) and 1500-dbar floats (right). Bathymetry and planetary potential vorticity (f/H) drawn as in Figure 3.5.4. Note color scales are not the same.

PERCENTAGE OF MEAN TO TOTAL KINETIC ENERGY

Calculating the percent of MKE relative to total kinetic energy highlights the dominance of mean flow regions when compared to the combined EKE and MKE in the same location. The 300-dbar percentage of MKE to total KE (Figure 3-44) shows that the dominant energy of the Campeche Gyre was from the MKE. The Campeche Gyre stands out as the only area that was dominated by MKE.

Similarly, in the lower layer the dominant MKE signature relative to the total KE is traced out by the Sigsbee Abyssal Gyre. This result is similar to that seen in Pérez-Brunius et al. (2018). One other interesting feature in the lower field is the hint of a persistent ‘vein’ of higher percentage of MKE to total KE along the 2000-m isobath from about 22.5°N southward around the boundary of the deep Bay of Campeche. This may be a signature of the persistent mean deep cyclonic boundary current.

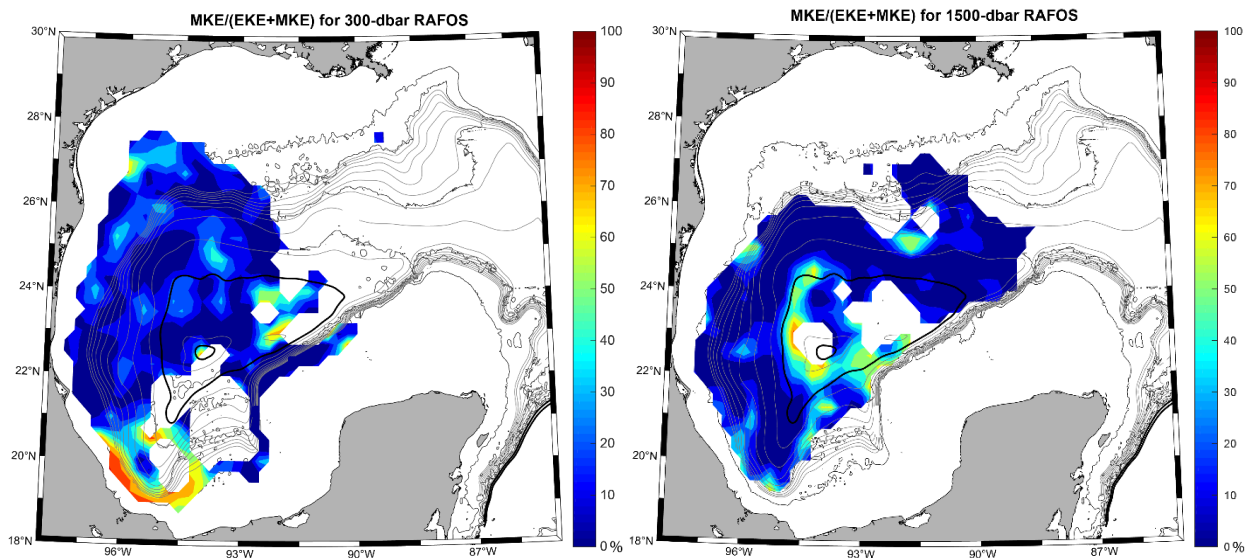


Figure 3-44. Percentage of mean to total kinetic energy [$MKE/(MKE+EKE) \times 100$] for 300-dbar floats (top) and 1500-dbar floats (bottom). Bathymetry and planetary potential vorticity (f/H) drawn as in Figure 3-40. In this case, color scales are the same.

CHAPTER 4. FLOAT ANALYSIS

4.1 Absolute Dynamic Topography and Trajectory Data

Absolute dynamic topography is a good indicator of upper layer circulation, specifically the Loop Current position, the LCR, and the eddy field across the Gulf. Plots of 15 trajectory segments of the 300-dbar and 1500-dbar floats, along with ADT, show that, in general, the upper layer floats move with the circulation pattern indicated by the ADT field, and the lower layer floats do not. There is some evidence indicating the existence of a dipole under a westward travelling LCR, which has previously been observed in the western Gulf (Tenreiro et al. 2018, Furey et al 2019). For example, in November 2016 (Figure 4-3, top 2 panels), deep floats cross directly under the center of the LCR Poseidon (see Figure 3-28). Transiting from northeast to southwest across the LCR, the floats trace out a cyclonic feature – possibly the trailing cyclone of a dipole pair. Deep floats seem energized by upper layer features (contrast the floats under and outside the upper layer LCR), but not following the same upper layer circulation as the 300-dbar floats do (for example August 1- 15 2017, Figure 4-7, lower left panel). From August – October 2017, the shallow floats clearly are trapped in the upper layer counter-rotating eddies observed in the ADT field (Figures 4-7 and 4-8). At first the deep floats appear sluggish and disorganized, but then accelerate southward along the western slope, increasing in speed by 10 cm s^{-1} during the same time that the upper layer eddies are impinging on the western boundary. In particular, when the leading anticyclone in the upper layer appears to dissipate (Figure 4-8, lower panels), the deep floats along the western slope return to sluggish $<5 \text{ cm s}^{-1}$ velocities.

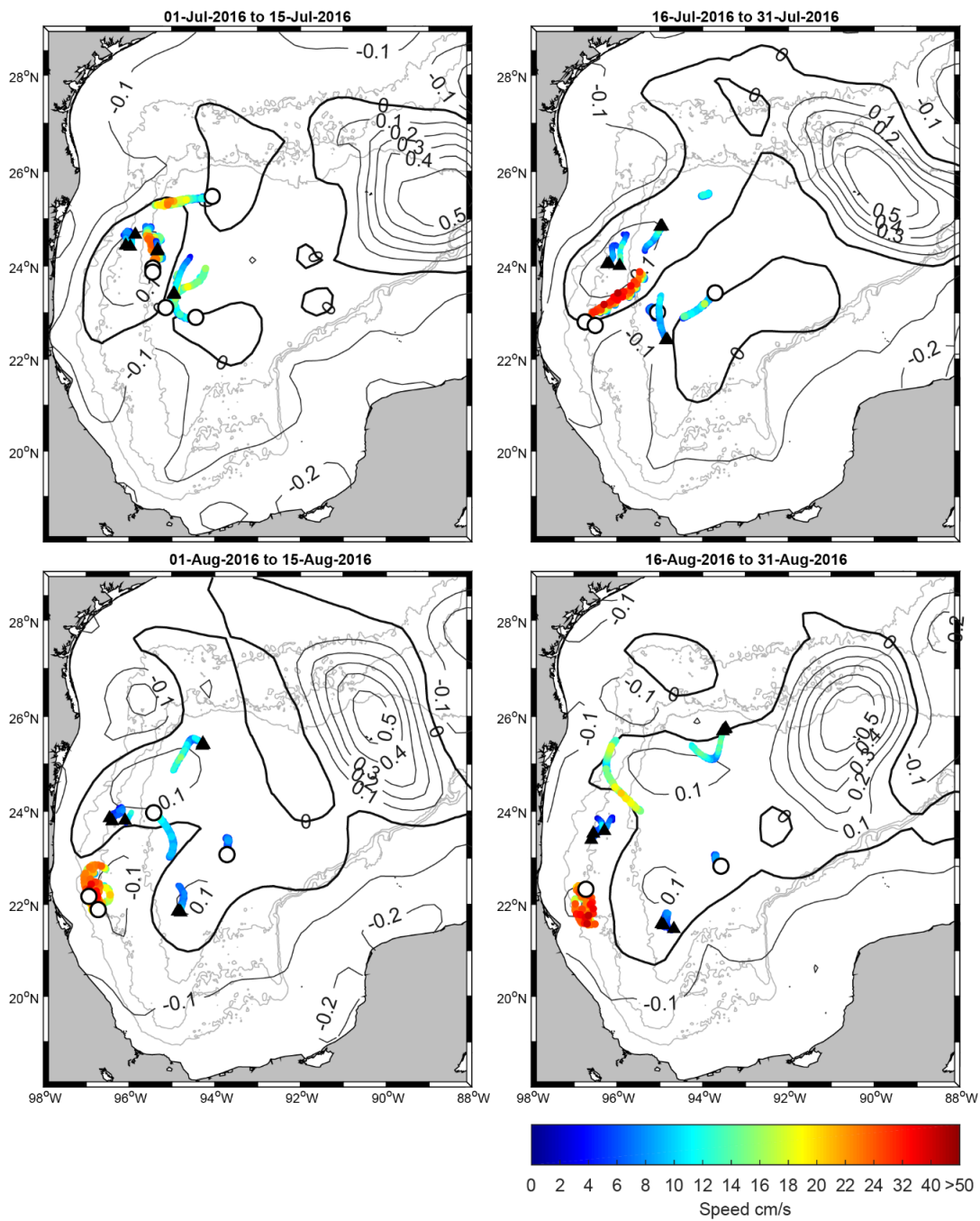


Figure 4-1. Fifteen-day length float trajectory segments with contoured absolute dynamic topography (ADT) at the center date of each segment. Date ranges for each panel are in the title, ADT is plotted at 0.1 m increments with the zero contour in bold. 300-dbar floats are marked with circles on the last day of each segment, and 1500-dbar floats with triangles. Float trajectory segments are color coded by speed. Bathymetry is drawn as gray lines at 1000, 2000, and 3000 m depth.

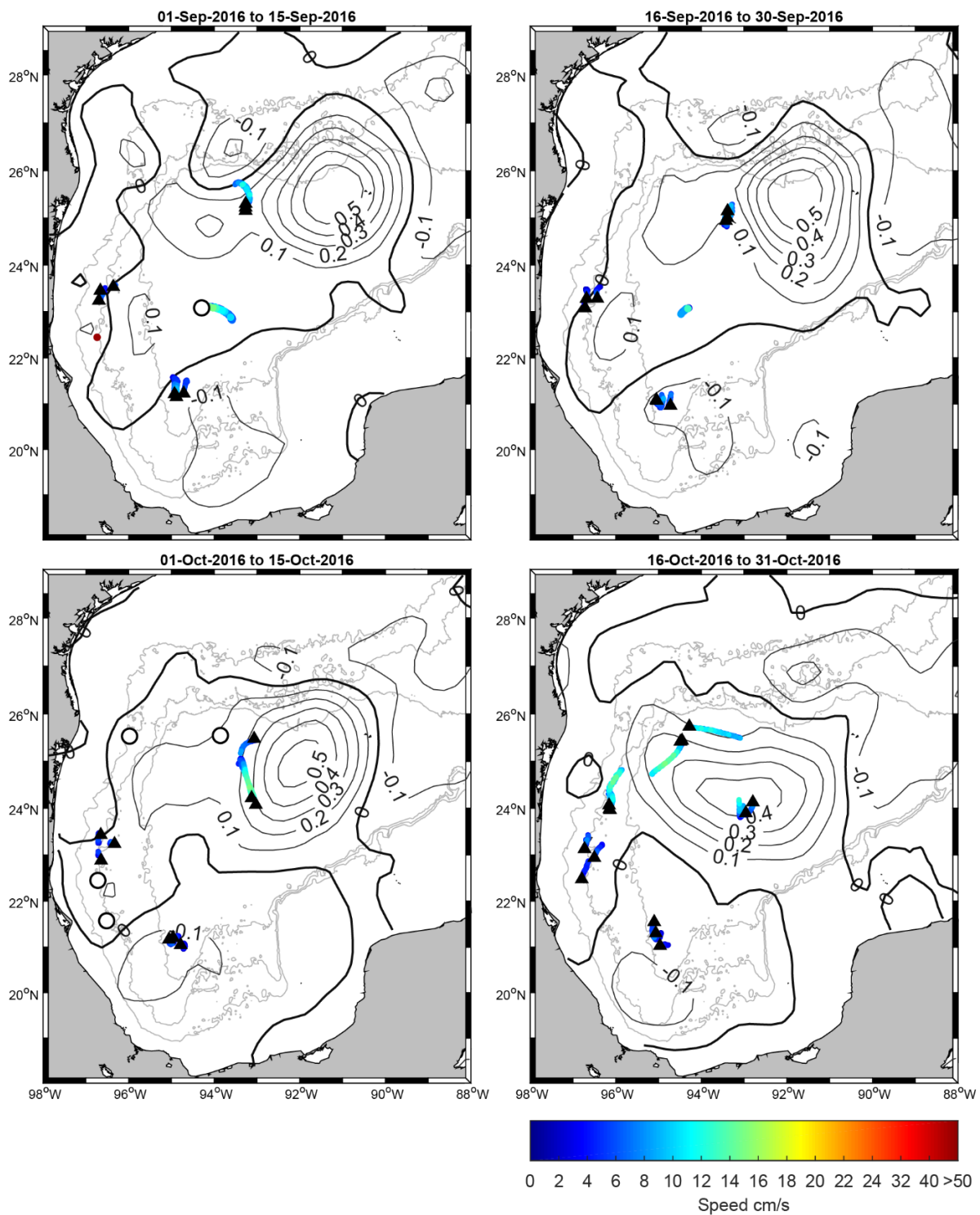


Figure 4-2. As in Figure 4-1, but for 01 September through 31 October 2016.

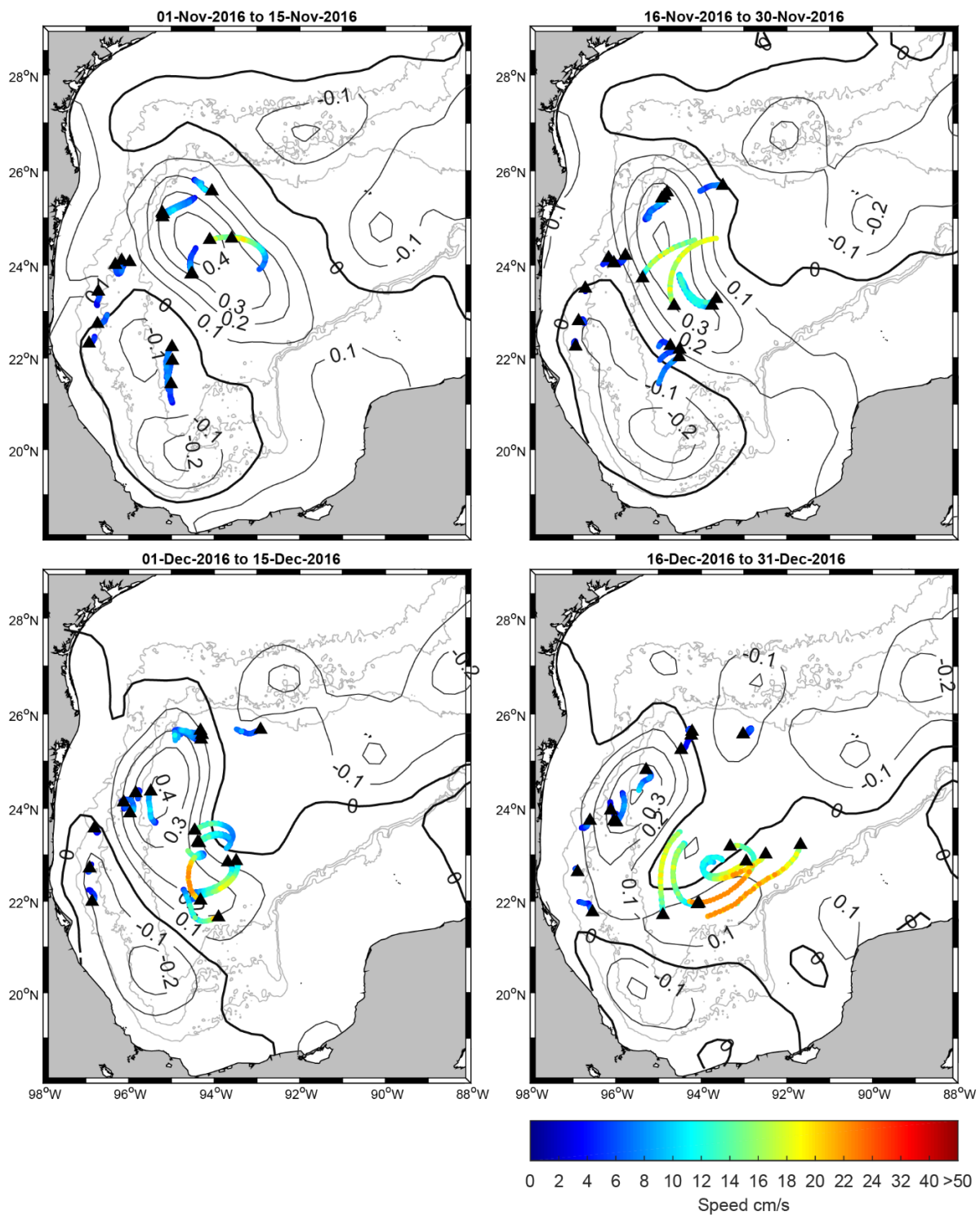


Figure 4-3. As in Figure 4-1, but for 01 November through 31 December 2016.

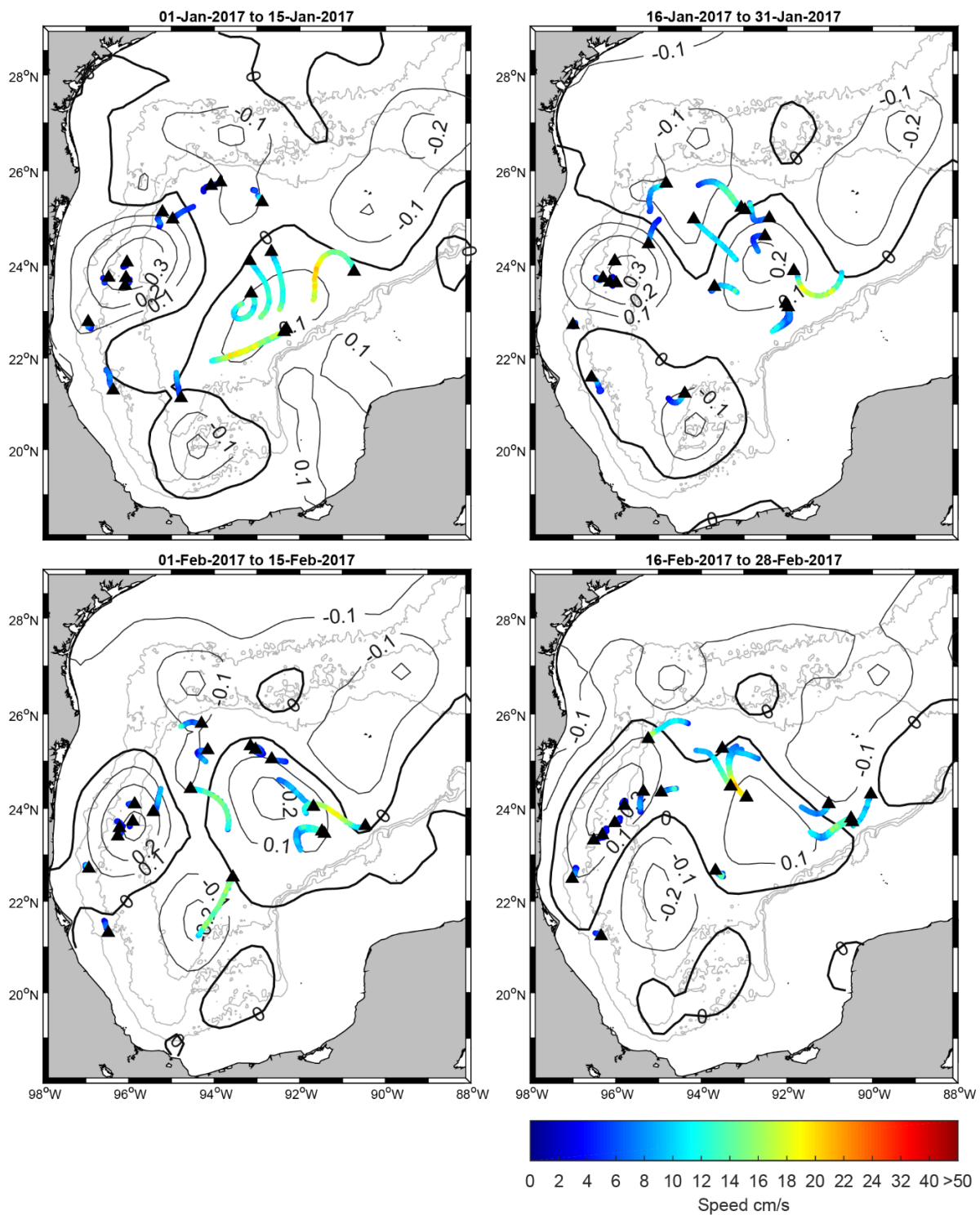


Figure 4-4. As in Figure 4-1, but for 01 January through 28 February 2017.

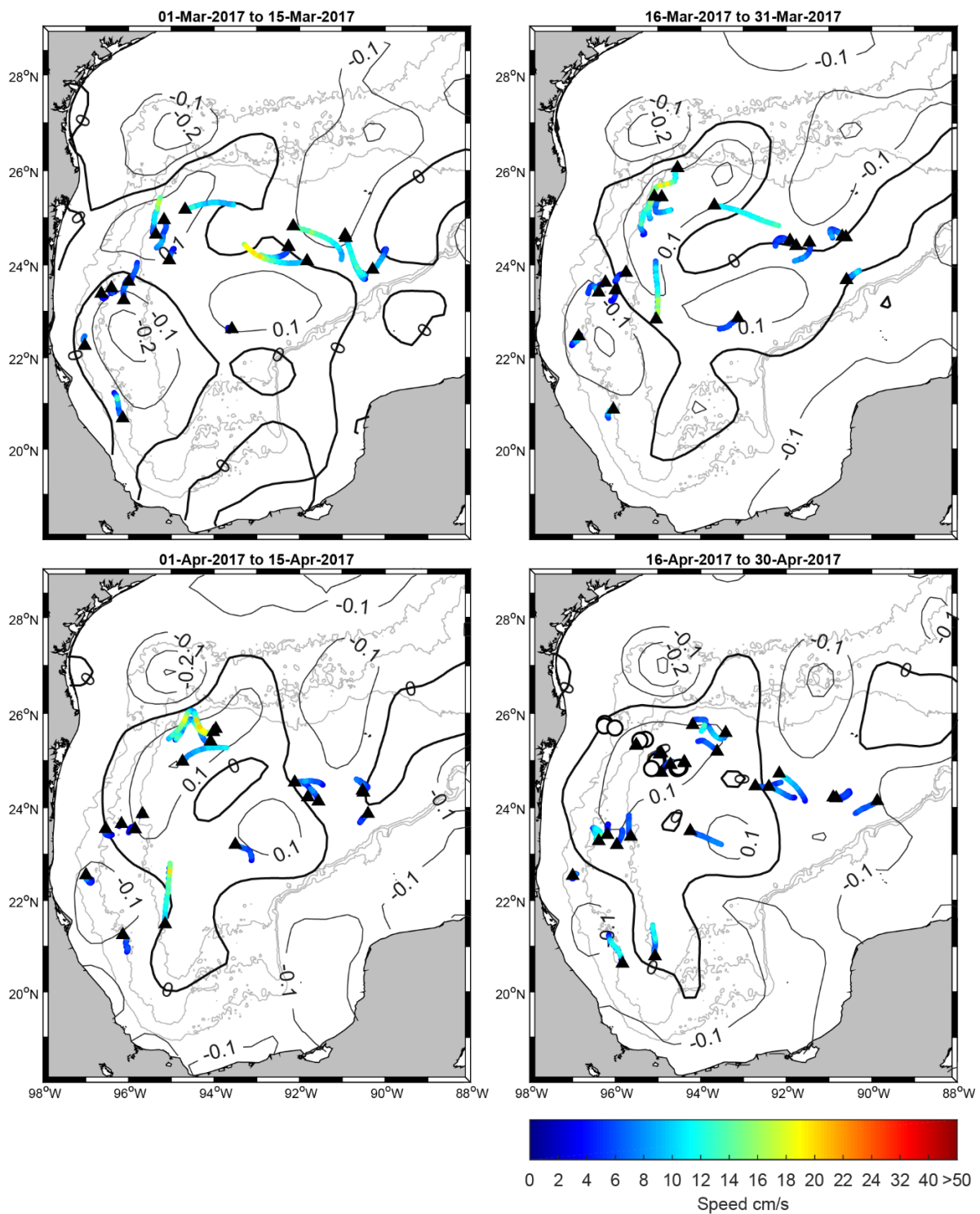


Figure 4-5. As in Figure 4-1, but for 01 March through 30 April 2017.

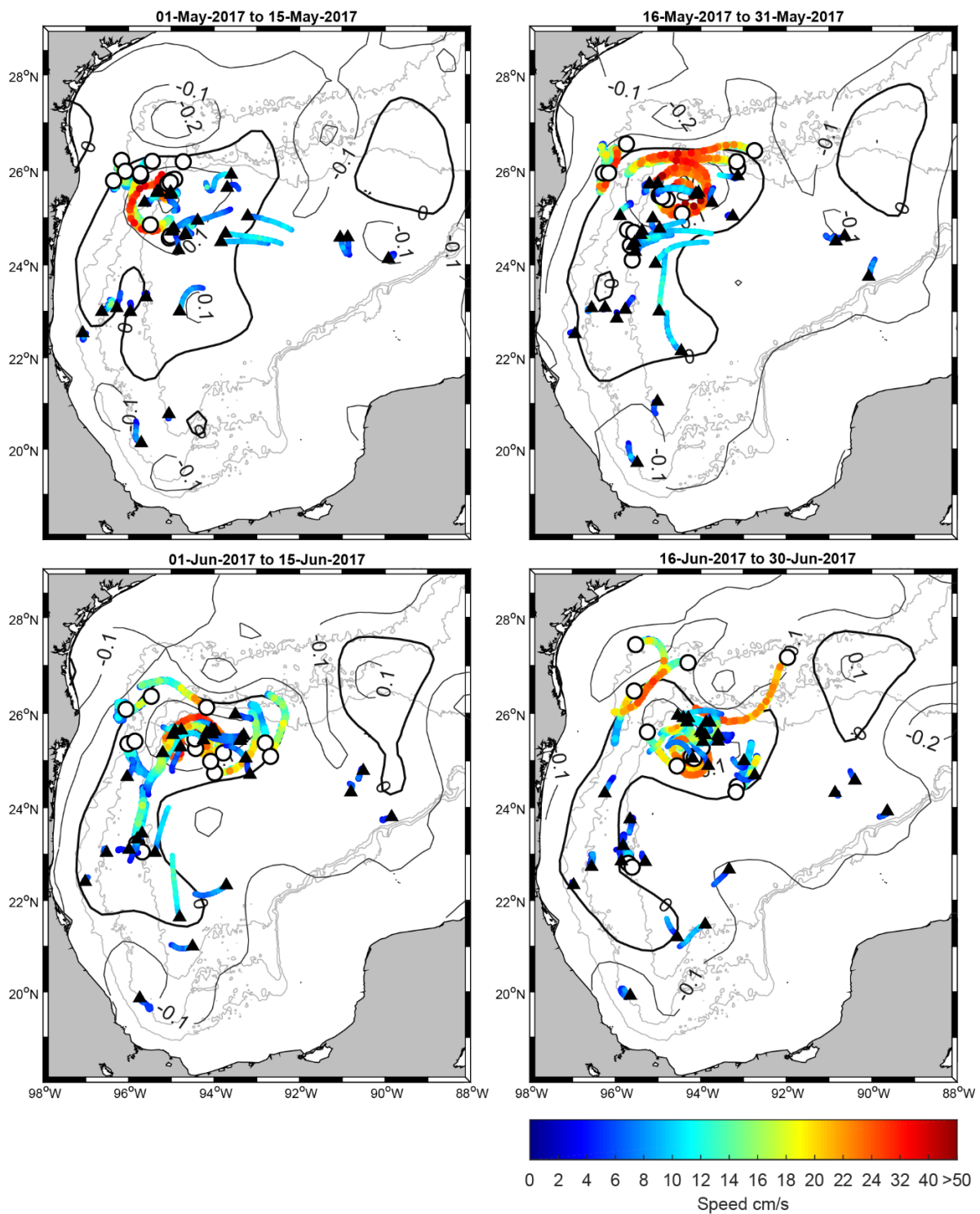


Figure 4-6. As in Figure 4-1, but for 01 May through 30 June 2017.

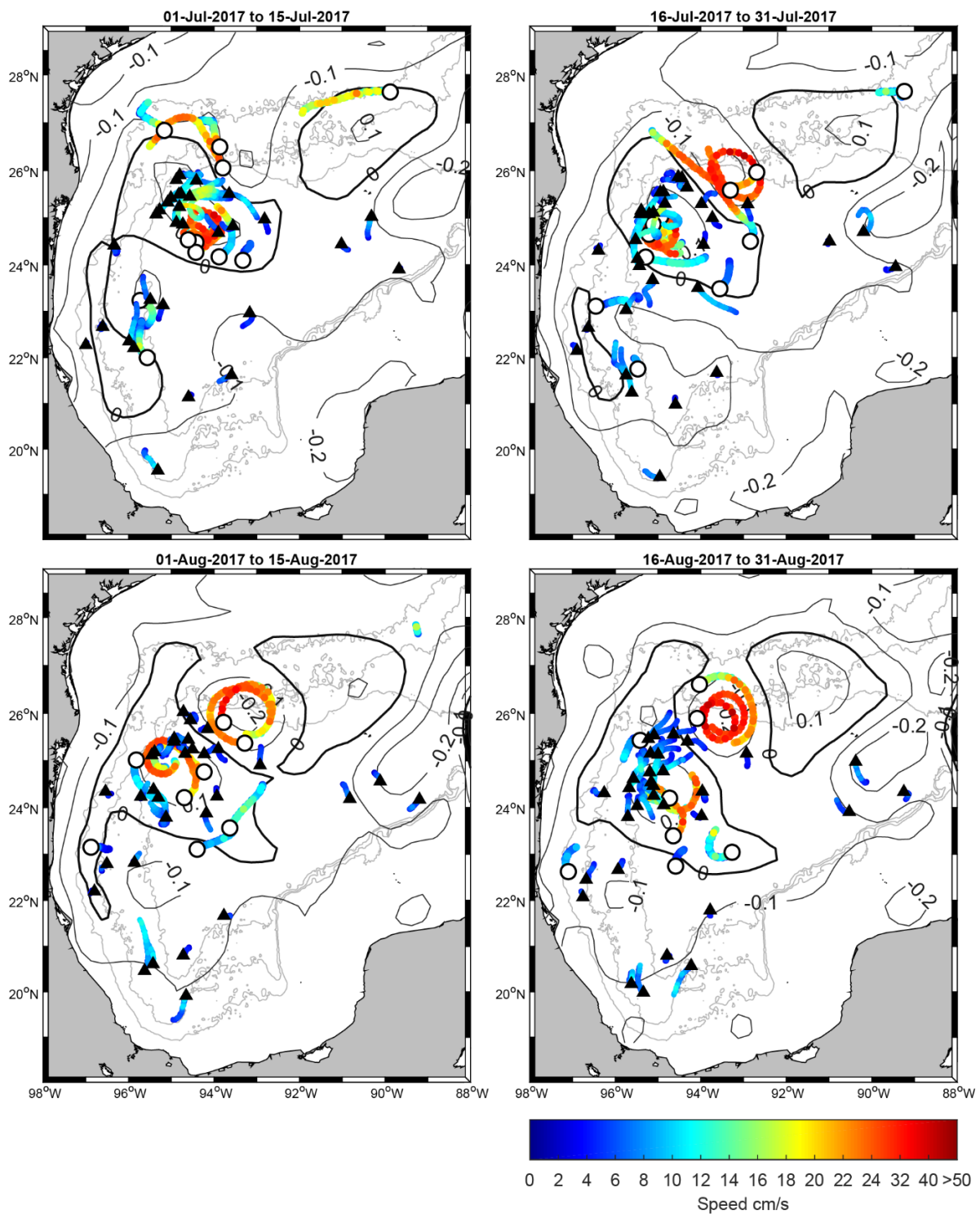


Figure 4-7. As in Figure 4-1, but for 01 July through 31 August 2017.

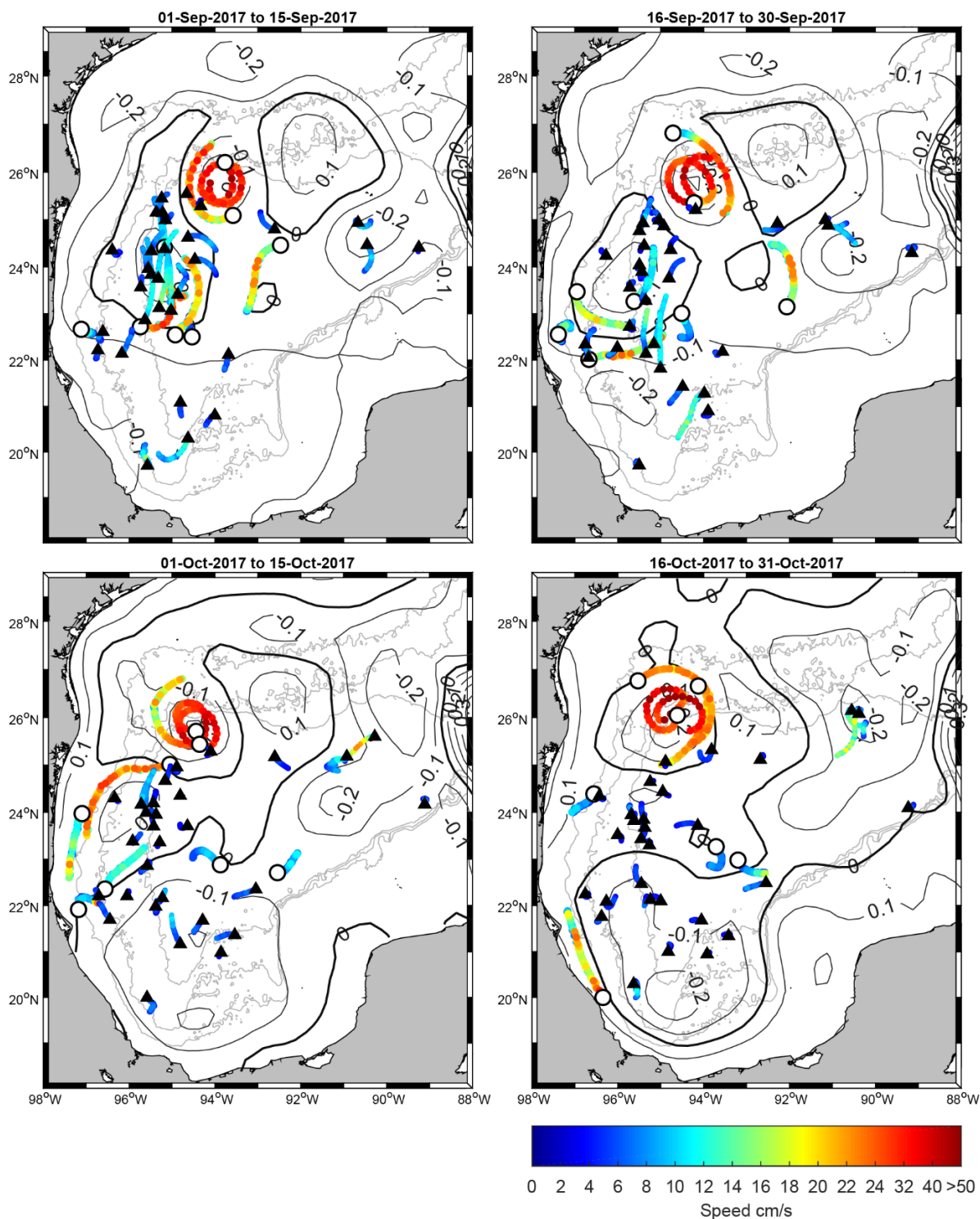


Figure 4-8. As in Figure 4-1, but for 01 September through 31 October 2017.

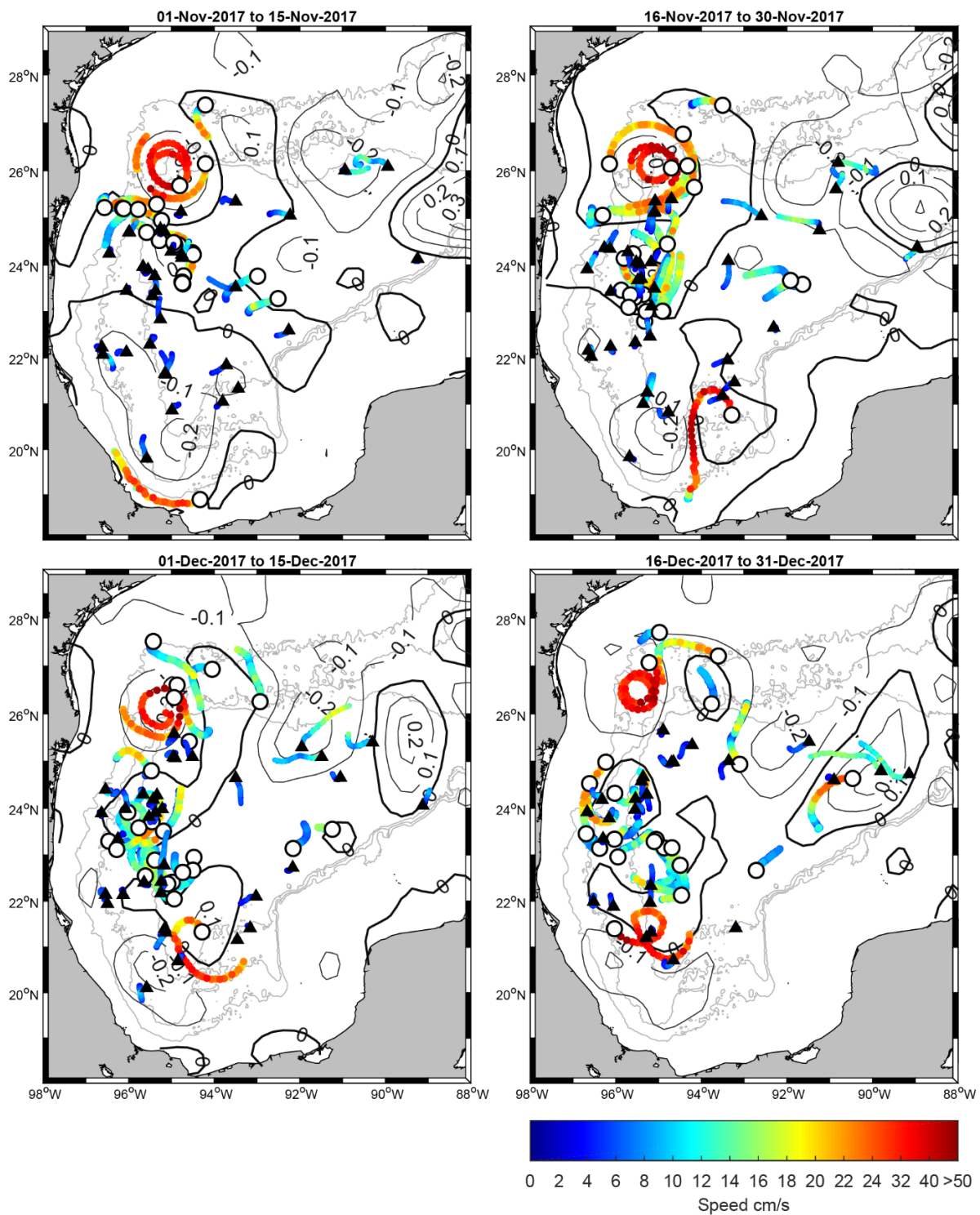


Figure 4-9. As in Figure 4-1, but for 01 November through 31 December 2017.

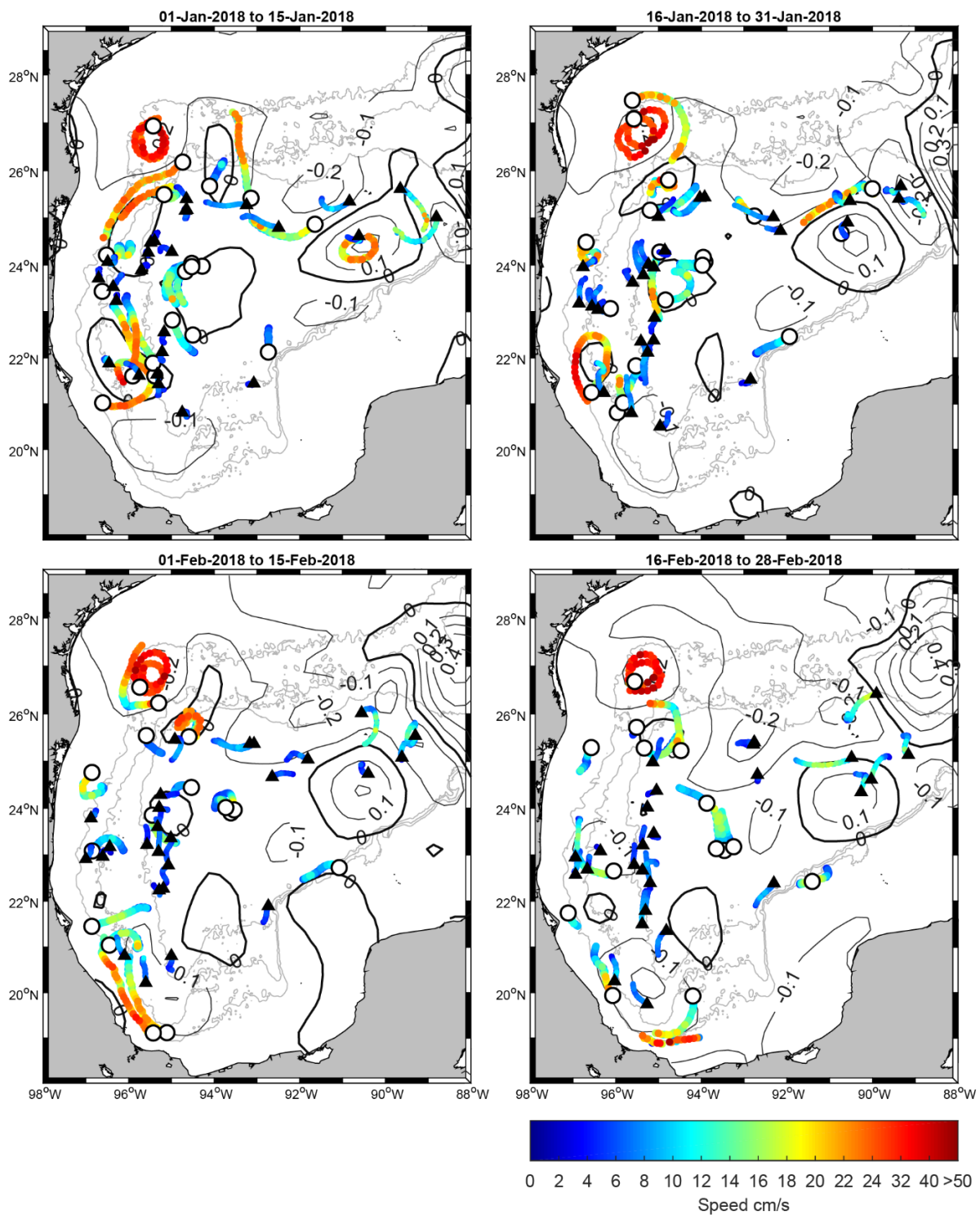


Figure 4-10. As in Figure 4-1, but for 01 January through 28 February 2018.

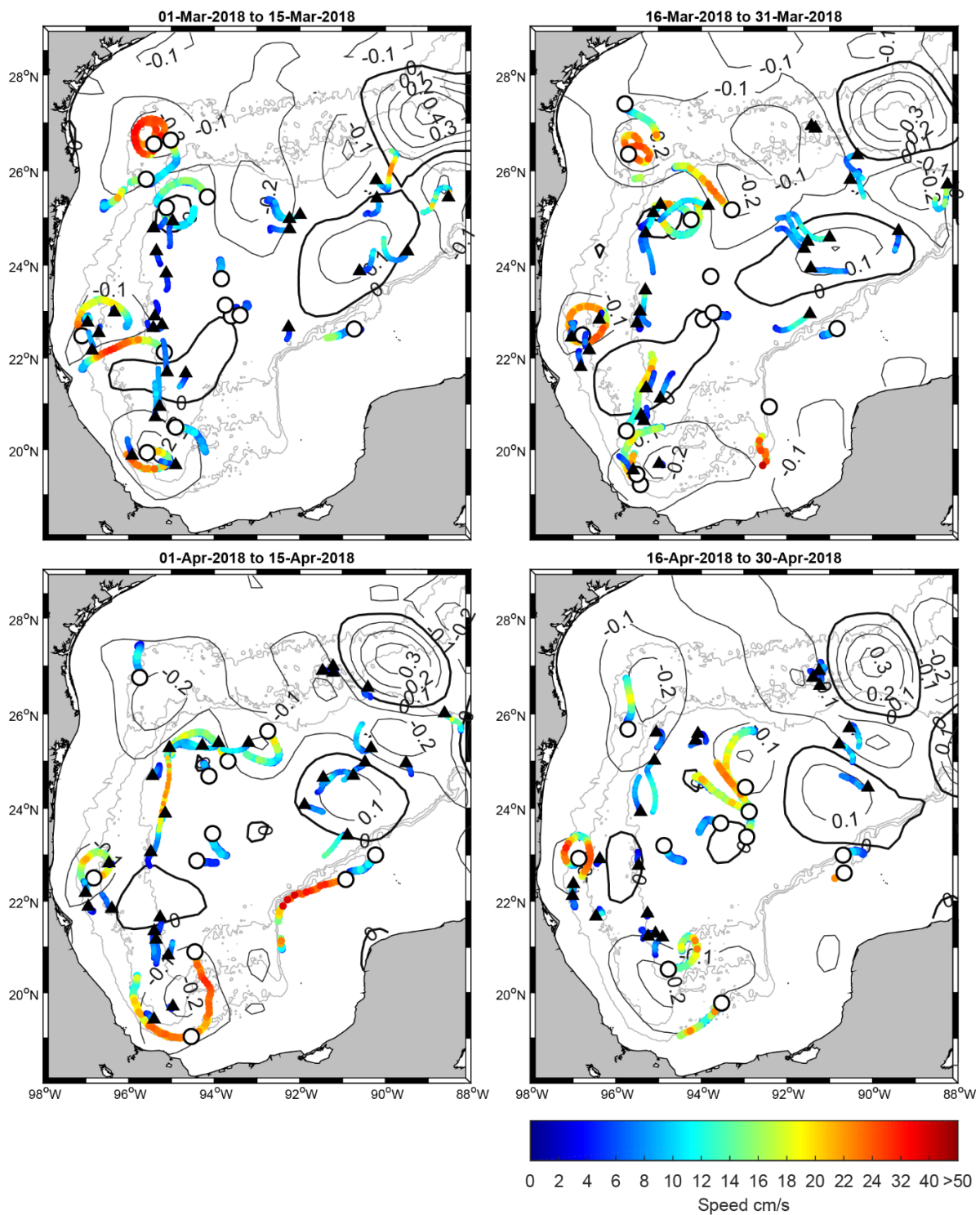


Figure 4-11. As in Figure 4-1, but for 0-March through 30 April 2018.

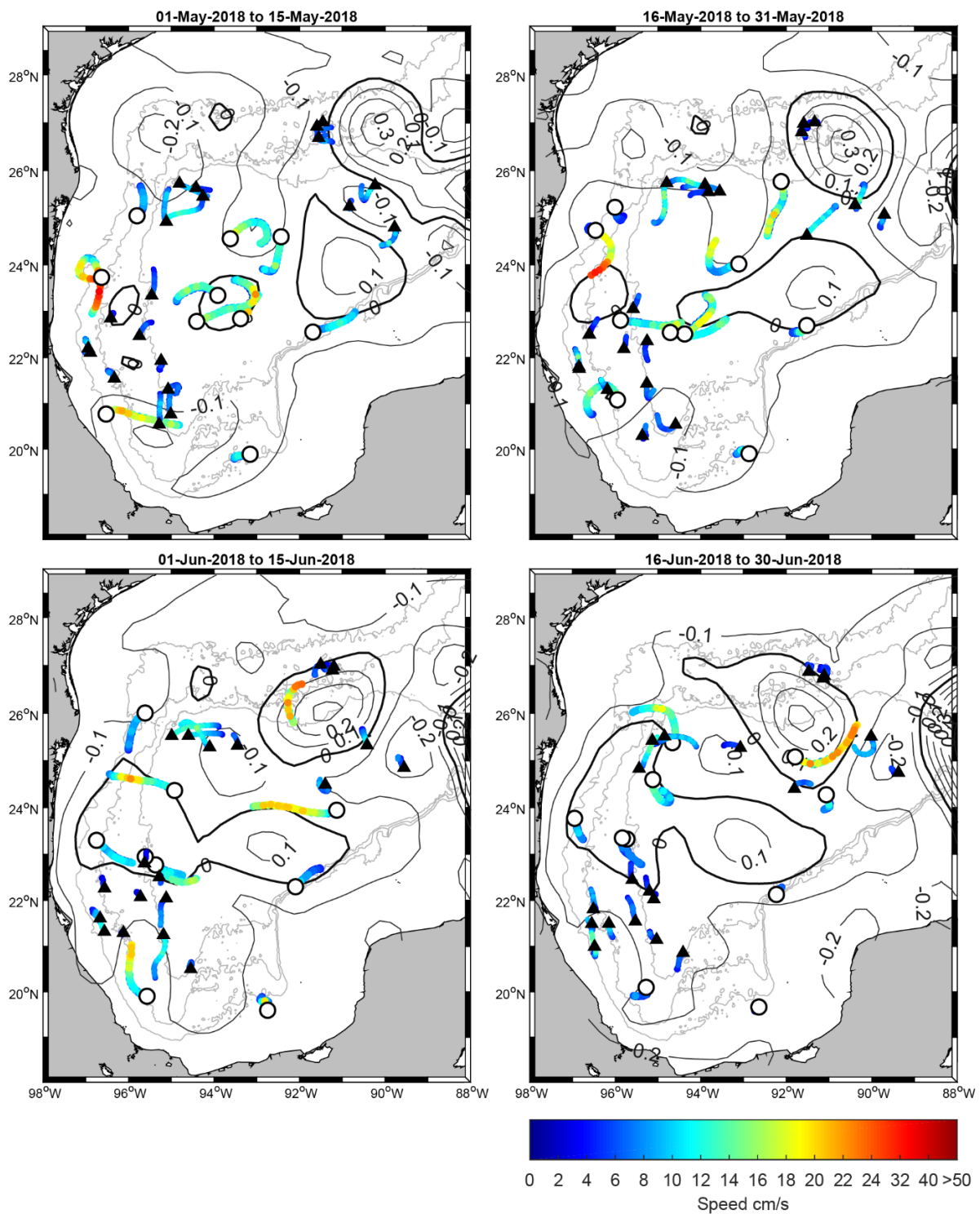


Figure 4-12. As in Figure 4-1, but for 01 May through 30 June 2018.

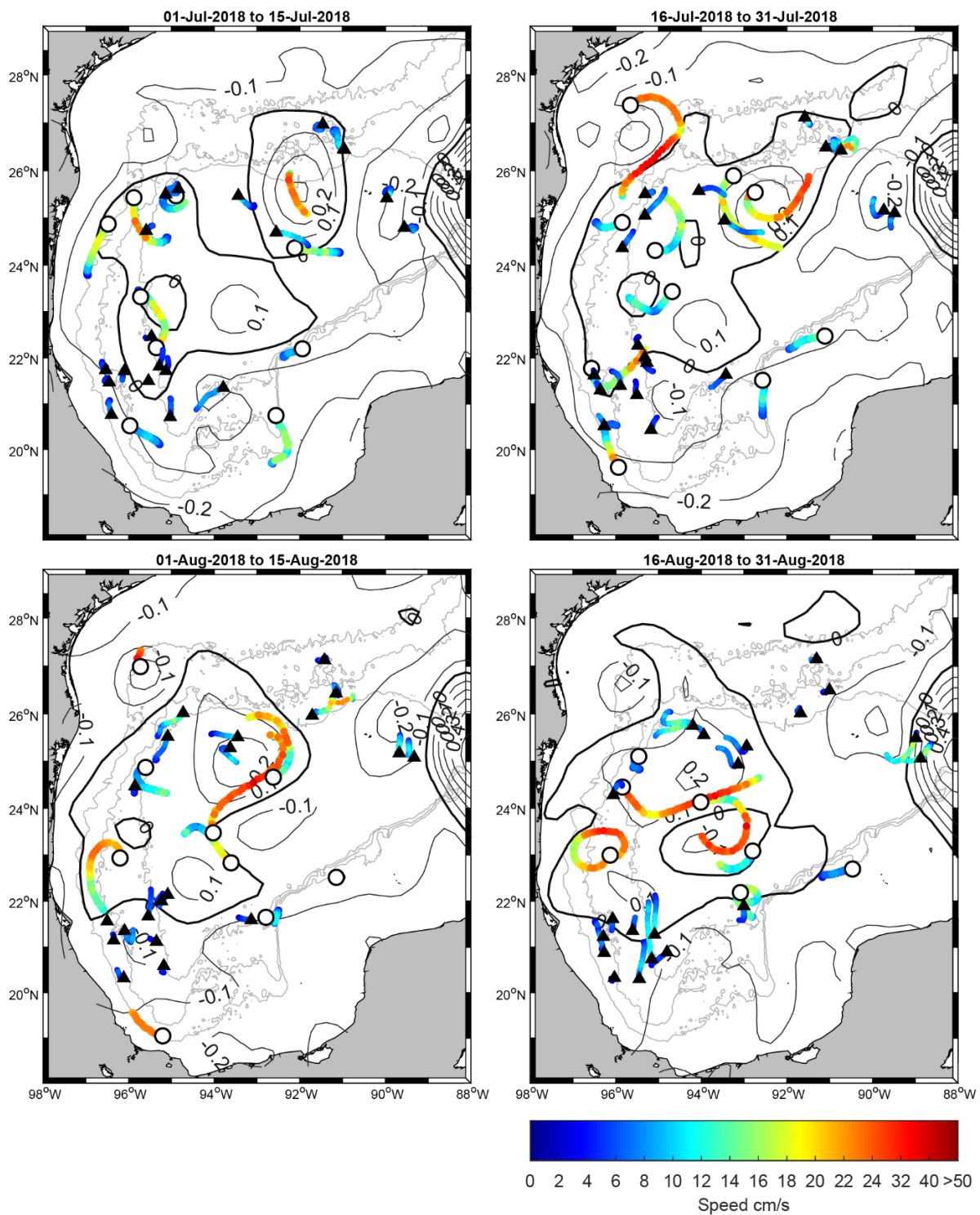


Figure 4-13. As in Figure 4-1, but for 01 July through 31 August 2018.

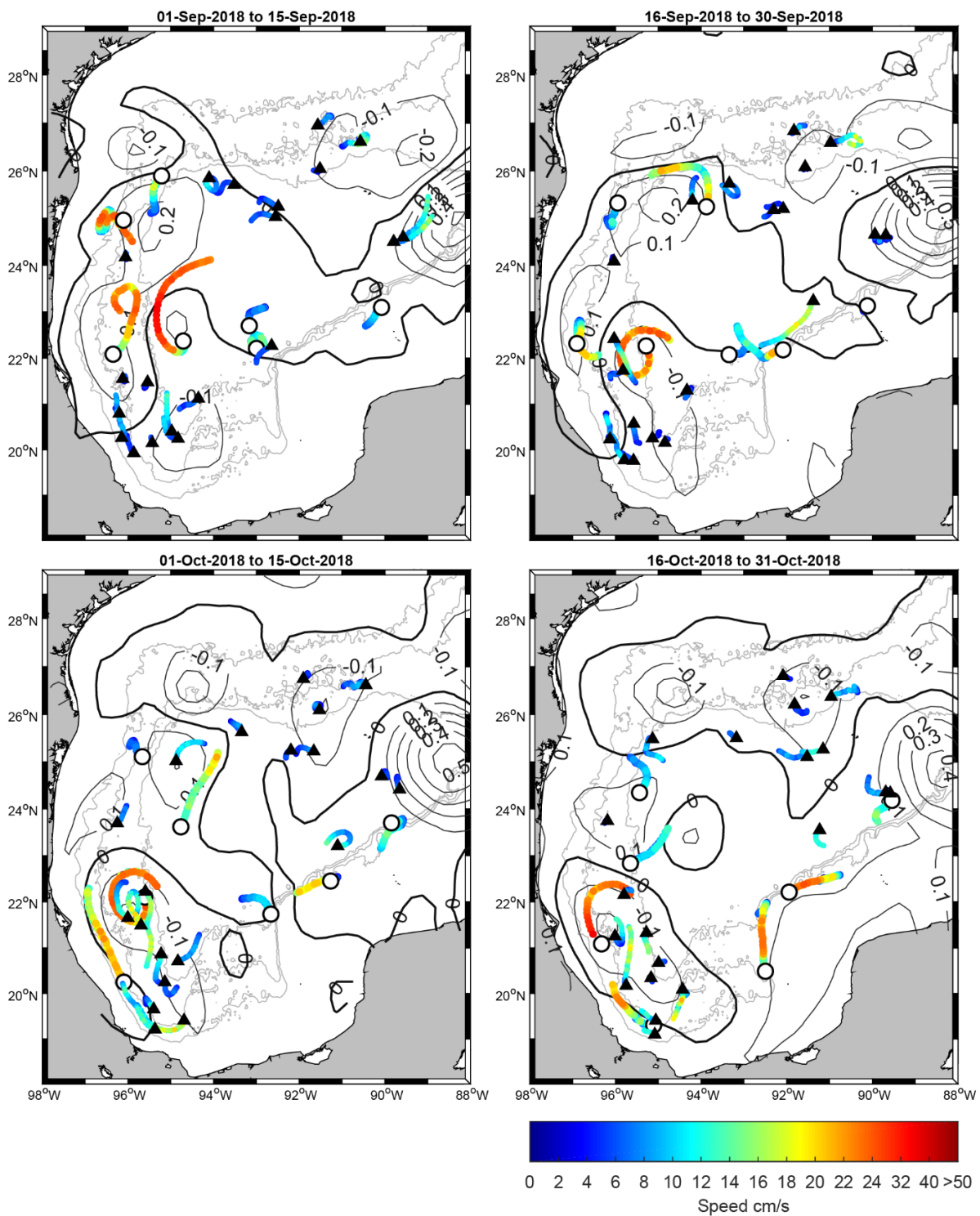


Figure 4-14. As in Figure 4-1, but for 01 September through 31 October 2018.

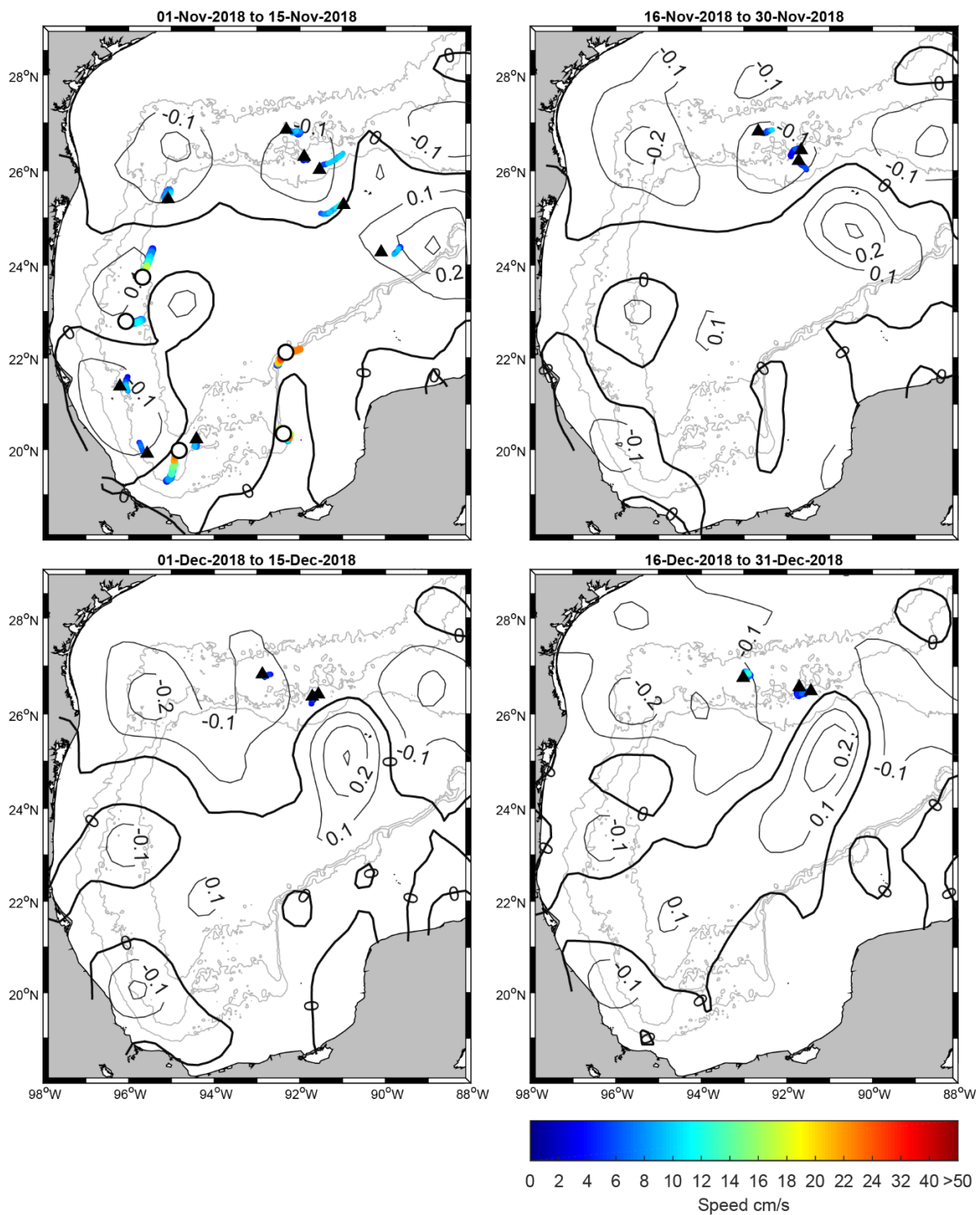


Figure 4-15. As in Figure 4-1, but for 01 November through 31 December 2018.

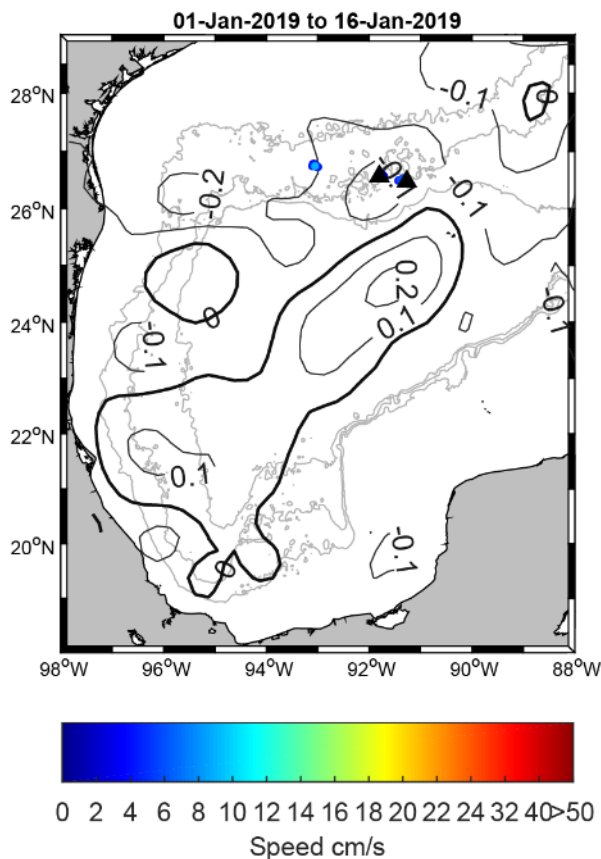


Figure 4-16. As in Figure 4-1, but for 01- January through 16 January 2019.

4.2 DISPERSION STATISTICS

CONTEXT OF THE STUDY

One of the objectives of the DWDE project was to study the rate at which tracers are diffused in the deep Northwest Gulf of Mexico. This region is influenced by large and energetic Loop Current Rings that collide with the western slope, resulting in complex topographic interaction, LCR erosion and vortex splitting, yielding a rich submesoscale environment. Because this dynamically rich and turbulent region is expected to be associated with rapid tracer dispersion, which can strongly impact oil spills, quantification of the dispersion properties in the Western GoM is of prime importance. The circulation of the GoM is essentially two-layered, with distinct processes dominating the surface and deep dynamics. Thus, the dispersion properties are also expected to be different. This study was designed to address these different circulation patterns by sampling different depths: surface, 300 m, and 1500 m.

METHODS

Dispersion of a tracer can be quantified by the mean of statistical analysis of the time evolution of particle separation as they are advected by a spatially variable current. Separation of two particles whose trajectories are described by the vectors $\vec{X}_1(t)$ and $\vec{X}_2(t)$ and initially separated by the vector \vec{R}_0 can be described as:

$$\vec{R}(t, \vec{R}_0) = \vec{R}_0 + \vec{X}_1(t) - \vec{X}_2(t)$$

Under the assumption that a patch of tracer is equivalent to a large set of particle pairs, initially separated by a distance \vec{R}_0 , dispersion can be defined as the ensemble mean of the squared pair separations:

$$R^2(t, R_0) = \langle \vec{R}(t, \vec{R}_0) \cdot \vec{R}(t, \vec{R}_0) \rangle$$

In the case of a large set of particles, relative diffusivity, which can be thought of as the rate at which the area of the tracer patch increases, is thus proportional to the time derivative of dispersion:

$$k(t) = \frac{1}{2} \frac{d}{dt} R^2(t, \vec{R}_0)$$

Given an initial pair separation \vec{R}_0 , dispersion and diffusivity are time-dependent functions. However, diffusivity can as well be expressed as a function of the particle separation scale $D(t)$ rather than time. The latter approach is useful since the growth rate of a tracer patch depends on its size, and diffusivity grows with growing pair dispersion. The scale dependence of diffusivity is a consequence of the scale dependence of the different turbulence regimes in the ocean.

At length scales of (1-100 km), ocean dynamics are mostly two-dimensional, so that the dispersion properties are well captured by fixed-depth drifting floats such as RAFOS floats, or using fixed-depth model velocity fields to advect numerical particles. At smaller scales, and particularly in the case of steeply sloping fronts (sharp horizontal density gradients), vertical velocity becomes non-negligible, and the fixed depth approach might induce errors in the dispersion and diffusivity. In that case, only chemical tracer injections (such as SF₆) can offer a truly complete description of the 3-dimensional diffusion.

PREVIOUS EXPERIMENTS IN THE DEEP GULF OF MEXICO

A previous project, funded by the U.S. Bureau of Ocean Energy Management, ‘Lagrangian Study of the Deep Circulation in the Gulf of Mexico (BOEM)’, studied the deep circulation of the GoM, collecting RAFOS float drift data at 1500 and 2500 m (<https://marinecadastre.gov/espis/#/search/study/100029>). Figure 4-17 shows the spatial distribution of the deployment locations. Since this experiment used a similar triplet and pair-launching strategy, with long-term monitoring of the floats (18 months) and a wide coverage of the GoM including the Northwest corner, it is of interest to use these data to compute and analyze supplementary relative dispersion statistics in the deep GoM.

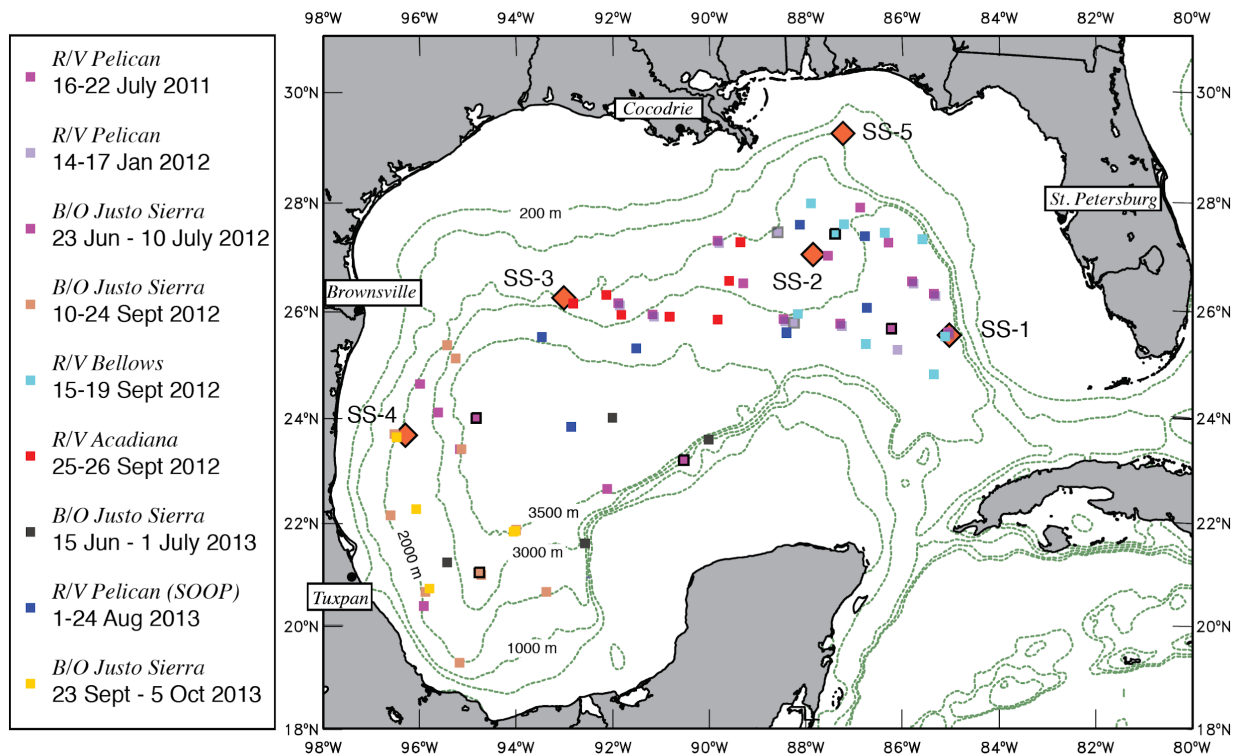


Figure 4-17. Launch locations of RAFOS and APEX floats from a previous program in the Gulf of Mexico. The survey names are color-coded. Sound source positions are shown as red diamonds. Figure from Hamilton et al. (2016).

NUMERICAL SIMULATIONS OF PARTICLE DISPERSION USING GOM'S REGIONAL CIRCULATION MODELS

The drift of particle triplets released at the same locations as the DWDE RAFOS floats and surface drifters was simulated using the velocity fields of three regional primitive equation models implemented in the frame of CIGoM (NEMO, ROMS and HYCOM).

Particles were released on the first day of each model month between 1993 and 2012. Particle advection was performed by integrating a fourth order Runge-Kutta scheme during 100 days with a temporal resolution of 1 hour. The models' spatial resolution ranged between 3 and 5 km, and the temporal resolution of the velocity fields was 1 day, corresponding to daily averages (hence filtering superinertial motion such as internal waves and inertia-gravity waves).

DEPTH DEPENDENCE OF DISPERSION PROPERTIES

Although coupling exists between the deep and near-surface GoM, the circulation patterns are completely different: The mean deep circulation, described by Pérez-Brunius et al. (2018), consists of a cyclonic

boundary current along the slope and a cyclonic abyssal gyre (the Sigsbee Abyssal Gyre), while the surface circulation is mostly driven by the Loop Current anticyclonic rings and cyclonic frontal eddies, as well as the Campeche cyclonic gyre in the southwestern GoM. Thus, significant differences in the dispersion properties are also expected.

Dispersion and diffusivity were computed from the DWDE and BOEM datasets using a total of 175 surface drifters, 47 300-dbar RAFOS floats, and 101 1500-dbar RAFOS floats (45 DWDE and 56 BOEM floats). Because of the smaller number of subsurface floats, we also searched for pairs of opportunity (floats that accidentally approached each other). To increase the significance of the statistics, BOEM floats from the western GoM were also included in the analysis.

Figure 4-18a shows dispersion against time for the three sampled depths. Surface drifter pairs and triplets separate immediately after launching, while the 300-dbar and 1500-dbar floats start to separate one and two days later, respectively. For the entire time series, relative dispersion is larger at the surface than at depth. It would take 10, 20, and 50 days for an initially 4 km wide tracer patch to reach a width of 100 km at the pressure of 1, 300, and 1500 dbar respectively.

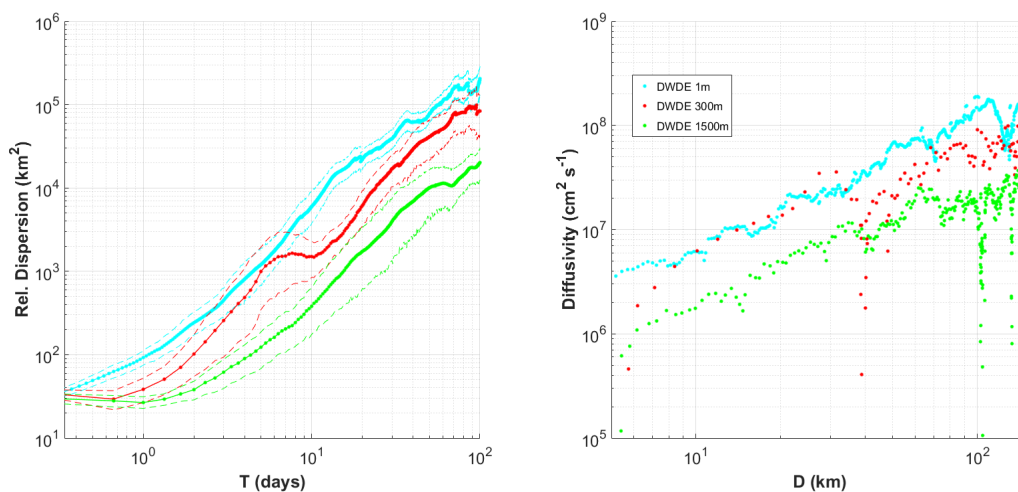


Figure 4-18. (a) Relative dispersion against time at 1 dbar (blue line), 300 dbar (red line), and 1500 dbar (green line). The thin lines represent the 95% confidence level. (b) Relative diffusivity against pair separation for the 1 dbar, 300 dbar, and 1500 dbar experiments. The color code is the same as panel (a).

Figure 4-18b shows that diffusivity is 2-3 times larger at the surface than at 1500 dbar, whatever the separation length scale. At 300 dbar, dispersion is of the same order of magnitude as at the surface for length scales of O(10-30 km), while for larger scales, the 300-dbar dispersion takes values in between those at the surface and at 1500 dbar. Note that a relatively small number of 300-dbar floats could be processed, in comparison with surface and 1500-dbar floats, so that the 300-dbar statistics might not be

as solid. Note also that 300-dbar floats were only released in two out of the four experiments. It is possible that having a larger dataset, acquired in a wider range of conditions, would result in the 300-dbar diffusivity ranging between that of the surface and of 1500 dbar for all length scales.

COMPARING FLOAT OBSERVATIONS AND MODEL SIMULATIONS

The relative dispersion and diffusivity obtained from the float data is compared with model simulations at the surface, 300 dbar, and 1500 dbar in Figures 4-19, 4-20, and 4-21, respectively.

The similarity between all three models is striking at the surface for both dispersion and relative diffusivity, regardless of the timescale (Figure 4-19). While dispersion initially grows exponentially in the DWDE data and in the model runs, the growth is significantly faster in the data than in the models: after the first 24 hours, DWDE dispersion estimates are three times greater than that derived from the models. From days 1 to 20, models and observations exhibit the same slope in relative dispersion. The magnitude of observed relative dispersion is, however, twice as large as the modeled dispersion. From days 30 to 100, the modeled dispersion converged towards the observations. Discrepancies between the model's surface diffusivity and the observations are evident in Figure 4-19b, with observed diffusivity being two to three times larger than modeled diffusivities.

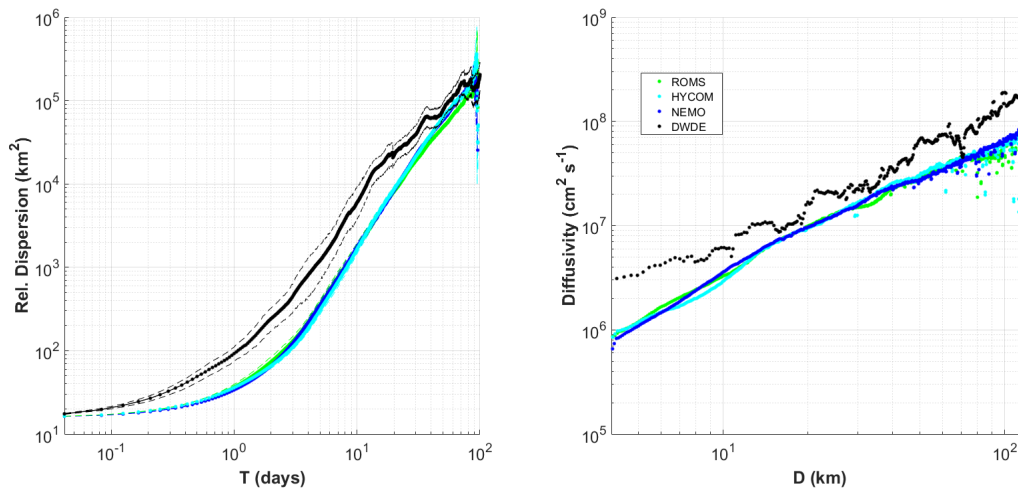


Figure 4-19. (a) Surface dispersion computed from the DWDE surface drifters (black line) and from the regional models (ROMS, green line; HYCOM, light blue; NEMO dark blue). The plain thin dashed lines represent the 95% confidence interval. (b) Same as (a) for diffusivity.

At 300 m, the Hycom and Nemo configurations are still in good agreement, while ROMS exhibits either significantly smaller dispersion, or a time lag of about 10 days in the onset of pair separation. The agreement between observations and model is reasonable after day 100 (there is only a factor two

between the observed and modeled dispersion), while at shorter times, they differ by one order of magnitude. Again, the lack of observations at 300 dbar could partially explain this discrepancy.

The agreement between models and observations in terms of diffusivity appears to be scale dependent: at separation scales larger than 40 km, results from all models closely match the observations, despite larger scattering than at the surface. At smaller scales, the observed diffusivity is about 5 times larger than in the models.

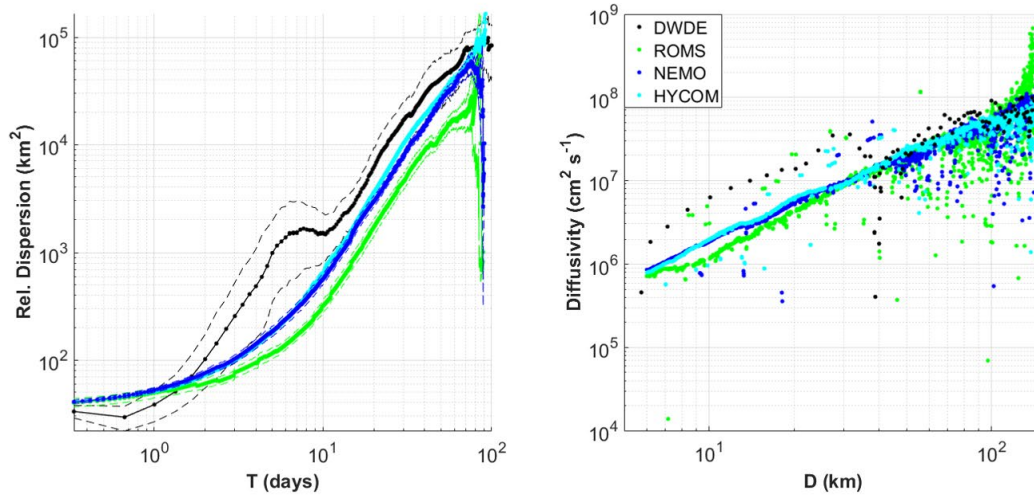


Figure 4-20. Same as for Figure 4.2.3, but at 300 m depth.

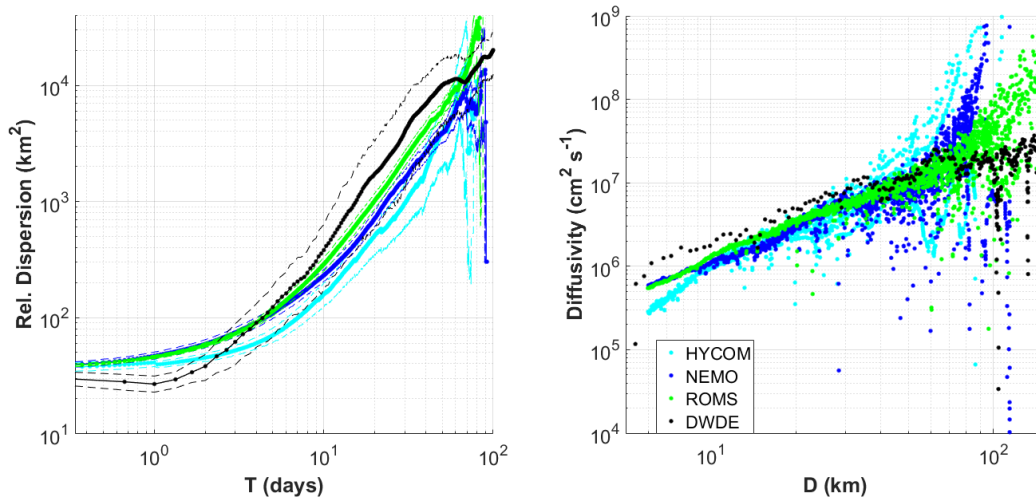


Figure 4-21. Same as for Figure 4.2.3, but at 1500 m depth.

At 1500 m, model estimates seem to diverge: after day 1, Hycom exhibits a significantly smaller dispersion than ROMS and NEMO (Figure 4-21a). The latter are in good agreement until day 10, when they start to diverge. The initial dispersion (<3 days) is faster in all models than in the observations. After three days, the observed dispersion growth is faster than in the models. Diffusivity at 1500 m (Figure 4-21b) shows more scattering in the models (ROMS in particular) at 1500 m than at the surface and at 300 m. Surprisingly, while the scattering in models is larger for scales larger than 40 km, the observed diffusivity in Hycom seems to converge towards the observed values at these scales. At smaller scales, where the models all show consistently similar values, they underestimate diffusivity by a factor two to five compared to observations.

CHAPTER 5. DISCUSSION AND RECOMMENDATIONS

While the initial goal of the DWDE experiment was to assess the dispersive and diffusive properties of the western Gulf of Mexico and their dependence on depth, it also contributed to strengthening our knowledge of the intermediate and deep Gulf's circulation patterns, as well as its mesoscale and submesoscale activity.

The mean deep circulation inferred from the 1500-dbar floats confirmed the permanent nature of the boundary current circling cyclonically around the basin, and of the Sigsbee Abyssal Gyre (SAG), previously reported by Pérez Brunius et al. (2018). In particular, the SAG appeared to be the dominating circulation feature of the deep GoM with a clear signal in mean kinetic energy density, evidently constrained by topography. Further examination of the anisotropy of deep floats trajectories, using the variance ellipses orientations and statistics of the ratio of along/across-bathymetry components of the flow, confirmed the general topographic control of the deep circulation.

At intermediate depth, the 300-dbar floats revealed two main circulation patterns in the form of seemingly persistent or recurrent cyclonic flows in the northwestern and southwestern corners of the GoM. While the southwestern circulation cell corresponds to the well-known Bay of Campeche Cyclone (BOC; Vázquez de la Cerda et al. 2005), we found no mention of the northwestern structure in the literature. The persistence and coherence of the BOC was demonstrated in a series of observational and numerical studies (Vázquez de la Cerda et al. 2005; DiMarco et al. 2005; Pérez-Brunius et al. 2013), and is confirmed here by a clear mean kinetic energy density signal, and a large mean kinetic energy density/eddy kinetic energy density ratio (the energy of the mean flow is significantly larger than that of the fluctuations). From our observations, it is difficult to conclude on the persistence of the northwestern cyclonic structure: while its signature is evident in the mean kinetic energy density maps, it is also associated with high eddy kinetic energy which indicates large fluctuations of the velocity field. This structure could thus be recurrent rather than persistent.

Either way, the presence of a cyclonic circulation at intermediate depth is an unexpected result since a recent modelling study suggested that the northwestern corner of the GoM was the locus of a coherent anticyclonic feature (The Hook; Gough et al. 2019). The apparent discrepancy between model results and our observations could be due to an excessive northward advection of anticyclonic relative vorticity in coarse resolution models, as Loop Current Rings interact with the western boundary. A recent study of the interaction between mesoscale eddies and western boundaries showed that the northward advection of anticyclones along a wall was blocked by the formation of stationary Kelvin waves, which are only resolved in very high vertical resolution models, so that coarser resolution models tend to exaggerate the northward advection of negative vorticity (de Marez et al. 2020). This artifact of the models, which might alter their ability to correctly describe the western GoM's circulation, deserve further investigations.

Because eddies are key to cross-slope exchanges and to turbulent diffusion, describing the mesoscale and submesoscale environment of the intermediate and deep GoM is crucial to put the study of dispersion and diffusivity in context. At intermediate depths (300 dbar), the RAFOS floats capture the complex current patterns of decaying Loop Current eddies as they interact with the western GoM's continental shelf and slope. An equal number of cyclonic eddies were tracked by the 300-dbar floats, including two cyclones drifting westward in the northern GoM, before reaching the northwestern corner, where they got trapped for several weeks. These eddies could possibly provide information on the nature of the mean cyclonic circulation discussed above: rather than being locally forced, this circulation could result from the accumulation of positive vorticity as cyclones drift northwestward towards the boundary and remain trapped in the large thalweg of the northwest corner.

While the number of observed eddies in the deep layer was moderate, the DWDE experiments confirmed the existence of a new class of deep eddies in the GoM, as three submesoscale (4 km average radius), high Rossby number (0.25) anticyclones were observed to drift southward in the boundary current along the western slope. While the RAFOS observations may not allow us to shed light on the formation mechanism of these submesoscale eddies, recent numerical experiments by Morvan et al. (2019) showed that frictional effects of a mean flow against a sloping boundary were able to generate a thin layer of intense negative vorticity, eventually evolving into a row of small anticyclonic eddies, confirming D'Asaro's (1988) theory. The use of a very high resolution regional numerical model could help to reveal the physics at work in the generation of these structures in the deep GoM, and to assess their possible effects on small spatial scale dispersion over the continental slope.

The DWDE experiments shed light on three major questions regarding relative dispersion and diffusivity:

- How dispersive and diffusive is the western GoM?
- What is the depth dependence of dispersion and diffusivity?
- How realistic are regional models?

Answering the first question, namely, quantifying relative dispersion and diffusivity, is obviously a requirement to answer the others. It also offers valuable information by itself. While it might sometimes be difficult to make sense of pointwise diffusivity values because of the scale dependence of the latter, the RAFOS float observations provide a scale-wise description of diffusivity and explicitly offer diffusivity estimates for each resolved scale of motion. This contrasts with the estimates of the Taylor diffusivity described in section 3.3, which exhibit the same orders of magnitude as the relative diffusivity for each sampled depth, but are unable to provide a scale-dependent description.

The depth dependence of diffusivity in the western GoM was clearly shown from the RAFOS float observation. At all separation scales, diffusivity is nearly one order of magnitude larger at the surface than at 1500 m, consistent with the observed decrease of EKE with increasing depth. The seemingly similar slope of the surface and 1500 m diffusivity distributions is, however, a counterintuitive result, as one would expect dramatically different turbulent regimes and thus different slopes.

Finally, our assessment of the performance of three different regional primitive equations models provide contrasting results. For a long time range (over 20 days), all models provide realistic dispersion estimates at the surface (within the 95% confidence interval of the drifters' observations). On the other hand, for short time ranges (1-20 days), the models' dispersion predictions are two to three times smaller than observed. Since the purpose of this model-observation comparison is to assess the ability of models to predict the dispersion of oil spills, or chemical contamination in general, the discrepancy at a short time scale might reveal an important issue. Contamination containment measures require rapid actions, at time scales of days or weeks, and to be useful, dispersion forecasts need to be valid at these short time scales. Underestimation of dispersion by a factor of two in models means that decontamination operations would be planned for an oil spill that is half the surface of the actual spill, resulting in the use of possibly inappropriate technical means

5.1 RECOMMENDATIONS

PAIR DISPERSION STATISTICS

While this preliminary analysis of the RAFOS float data allowed us to quantify dispersion and diffusivity in the western Gulf of Mexico and to highlight their sensitivity to depth for the first time, further analysis is required to understand the physical processes driving the dispersion properties. In particular, computation of the diffusivity slopes as well as the Finite Size Lyapunov Exponents, following LaCasce and Ohlmann (2003), is necessary to assess the dispersion regimes found at different depths, and should be performed on these data in the future.

INCREASED VERTICAL RESOLUTION AND GENERALIZATION OF THE RESULTS

Since the DWDE experiment clearly demonstrated the depth dependence of dispersion in the western Gulf of Mexico, similar experiments in other regions of the ocean, with different dynamics and a different vertical distribution of kinetic energy, would allow us to generalize our findings. Considering the success of the DWDE experiment, planning a similar experiment with an increased number of sampled depths would be of interest. In particular, while the depths sampled here well represent each of the two layers of the Gulf of Mexico, the dispersive properties in the vicinity of the interface between the layers remain unexplored. Repeating the experiment with an increased vertical resolution could thus provide a more detailed picture of the vertical distribution of diffusivity.

TRACER DIFFUSIVITY OF LOOP CURRENT EDDIES

The DWDE project was designed and executed in the western Gulf of Mexico to answer the concerns of oil spill dispersion in an intensive drilling region. However, quantifying dispersion and diffusivity is also key to understanding the heat and salt budgets in the world ocean and in the Gulf of Mexico in particular, where the long term heat content and sea level are largely controlled by the rate at which the heat content of Loop Current Eddies is diffused towards the Gulf's water (Meunier et al. 2020). Performing a similar experiment as DWDE, targeting Loop Current Rings drifting in the central GoM could provide crucial information on the GoM's heat budget, and on how eddies release their tracers in general.

NORTHWESTERN CYCLONIC CIRCULATION

The previously unnoticed cyclonic structure in the GoM's northwestern corner described in this report is one of the major findings of the DWDE experiments in terms of mean circulation features. Further assessment of its persistence over time is however needed to determine if this structure is quasi-permanent, is recurrent, or was simply a fortuitous measurement. The use of all available surface drifters in the GoM, combined with satellite altimetry, would allow a better understanding of the nature and physical forcing of this possibly important feature of the western GoM's upper layer circulation.

UNDERSTANDING THE DYNAMICS AND IMPACTS OF THE SUBMESOSCALE SLOPE EDDIES

Observations of deep submesoscale anticyclonic eddies embedded in the western boundary current also encourage further investigations. While recent studies highlighted the existence of intrathermocline or subthermocline eddies in the Gulf of Mexico at the tip of the Campeche Bank (Furey et al. 2018), under Loop Current Rings (Meunier et al. 2018b), or along the northern shelf-break (Bracco et al. 2016), this is the second time that such structures have been found along the western slope. Using a regional numerical model, Bracco et al. (2016) highlighted the possibly strong impact of such submesoscale eddies on tracer dispersion along the northern slope. Assessing the abundance of these eddies, their formation mechanism and their vertical structure thus seems necessary to understand the physical processes at work in the deep tracer dispersion at small time and space scales in the western GoM. This kind of submesoscale activity, whether in the form of turbulence or of coherent structures, is not represented by the currently used regional numerical simulations of the GoM, and might be one of the missing ingredients leading to the discrepancy between the modelled and observed dispersions and diffusivities at depth. Implementation of a very high resolution model configuration centered on the western slope seems necessary to understand the formation and evolution of these submesoscale eddies and their impact on local dispersion.

CHAPTER 6. ACKNOWLEDGMENTS

The authors wish to thank Melinda Hall (WHOI) for her help with scientific editing. The altimeter products were produced by Ssalto/Duacs and distributed by Aviso, with support from CNES (<http://www.aviso.altimetry.fr/duacs/>).

CHAPTER 7. REFERENCES

- Bracco, A., Choi, J., Joshi, K., Luo, H., & McWilliams, J. C. (2016). Submesoscale currents in the northern Gulf of Mexico: Deep phenomena and dispersion over the continental slope. *Ocean Modelling*, 101, 43-58.
- D'Asaro, E. A. (1988). Generation of submesoscale vortices: A new mechanism. *Journal of Geophysical Research: Oceans*, 93(C6), 6685-6693.
- de Marez, C., Meunier, T., Tedesco, P., L'Hégaret, P., & Carton, X. (2020). Vortex–wall interaction on the β -plane and the generation of deep submesoscale cyclones by internal Kelvin Waves–current interactions. *Geophysical & Astrophysical Fluid Dynamics*, 1-19.
- DiMarco, S. F., Nowlin, W. D., & Reid, R. O. (2005). A statistical description of the velocity fields from upper ocean drifters in the Gulf of Mexico. *Geophysical Monograph-American Geophysical Union*, 161, 101.
- Domínguez-Guadarrama A. and P. Pérez-Brunius (2017). “CIGoM altimetry derived products from AVISO Ssalto/DUACS” L4, V1.0, GridSeries, [dataset] CICESE.
- Furey, H., Bower, A., Pérez-Brunius, P., Hamilton, P., & Leben, R. (2018). Deep eddies in the Gulf of Mexico observed with floats. *Journal of Physical Oceanography*, 48(11), 2703-2719.
- Gough, M. K., Beron-Vera, F. J., Olascoaga, M. J., Sheinbaum, J., Jouanno, J., & Duran, R. (2019). Persistent Lagrangian transport patterns in the northwestern Gulf of Mexico. *Journal of Physical Oceanography*, 49(2), 353-367.
- Hamilton, P. A. Bower, H. Furey. R. Leben, and P. Pérez-Brunius, 2016. Deep Circulations in the Gulf of Mexico: A Lagrangian Study. U.S. Department of the Interior, Bureau of Ocean Energy Management, Gulf of Mexico OCS Region, New Orleans, LA. OCS Study BOEM 2016-081, 289 pp.
- Hamilton, P., Leben, R., Bower, A., Furey, H. and Pérez-Brunius, P., 2018. Hydrography of the Gulf of Mexico using autonomous floats. *Journal of Physical Oceanography*, 48(4), pp.773-794.
- Hamilton, P., A. Bower, H. Furey, R. Leben, and P. Pérez-Brunius, 2019. The Loop Current: Observations of deep eddies and topographic waves. *Journal of Physical Oceanography*, doi.10.1175/JPO-D-18-0213.1.
- LaCasce, J. H., & Ohlmann, C. (2003). Relative dispersion at the surface of the Gulf of Mexico. *Journal of Marine Research*, 61(3), 285-312.
- Meunier, T., Tenreiro, M., Pallàs-Sanz, E., Ochoa, J., Ruiz-Angulo, A., Portela, E., ... & Carton, X. (2018). Intrathermocline eddies embedded within an anticyclonic vortex ring. *Geophysical Research Letters*, 45(15), 7624-7633.

- Meunier, T., Sheinbaum, J., Pallàs-Sanz, E., Tenreiro, M., Ochoa, J., Ruiz-Angulo, A., ... & de Marez, C. (2020). Heat Content Anomaly and Decay of Warm-Core Rings: the Case of the Gulf of Mexico. *Geophysical Research Letters*, 47(3), e2019GL085600.
- Morey, S.L., Gopalakrishnan, G., Sanz, E.P., Azevedo Correia De Souza, J.M., Donohue, K., Pérez-Brunius, P., Dukhovskoy, D., Chassignet, E., Cornuelle, B., Bower, A. and Furey, H., 2020. Assessment of numerical simulations of deep circulation and variability in the Gulf of Mexico using recent observations. *Journal of Physical Oceanography*, 50(4), pp.1045-1064.
- Morvan, M., L'Hégaret, P., Carton, X., Gula, J., Vic, C., de Marez, C., ... & Koshel, K. (2019). The life cycle of submesoscale eddies generated by topographic interactions. *Ocean Science*, 15(6).
- Oey, L., Ezer, T., & Lee, H. (2005). Loop Current, rings and related circulation in the Gulf of Mexico: A review of numerical models and future challenges. *Geophysical Monograph-American Geophysical Union*, 161, 31.
- Pallàs-Sanz, E., Candela, J., Sheinbaum, J., Ochoa, J., & Jouanno, J. (2016). Trapping of the near-inertial wave wakes of two consecutive hurricanes in the Loop Current. *Journal of Geophysical Research: Oceans*, 121(10), 7431-7454.
- Pérez-Brunius, P., García-Carrillo, P., Dubranna, J., Sheinbaum, J., & Candela, J. (2013). Direct observations of the upper layer circulation in the southern Gulf of Mexico. *Deep Sea Research Part II: Topical Studies in Oceanography*, 85, 182-194.
- Pérez-Brunius, P., Furey, H., Bower, A., Hamilton, P., Candela, J., García-Carrillo, P. and Leben, R., 2018. Dominant circulation patterns of the deep Gulf of Mexico. *Journal of Physical Oceanography*, 48, 511–529, doi.org/10.1175/JPO-D-17-0140.1
- Ramsey, A., H. Furey, A. Bower, P. Pérez Brunius, and P. García Carrillo, 2019. The Deep Water Dispersion Experiment: RAFOS Float Data Report, June 2016 - January 2019. *Woods Hole Oceanographic Institution Technical Report*, WHOI-2020-01.
- Rossby, T., D. Dorson, and J. Fontaine, 1986. The RAFOS system. *J. Atmos. Oceanic Technol.*, 3, 672-679.
- Vázquez De La Cerda, A. M., Reid, R. O., DiMarco, S. F., & Jochens, A. E. (2005). Bay of Campeche circulation: An update. *GMS*, 161, 279-293.
- Wooding, C., H. Furey, and M. Pacheco, 2005. RAFOS Float Processing at the Woods Hole Oceanographic Institution. *Woods Hole Oceanographic Institution Technical Report*, WHOI-2005-02, 35 pp.